

AD-A111 903

WEIDLINGER ASSOCIATES MENLO PARK CA

F/G 8/11

RESEARCH INTO SURFACE WAVE PHENOMENA IN SEDIMENTARY BASINS.(U)

DEC 81 G L WOJCIK, J ISENBERG, F MA

F49620-80-C-0009

UNCLASSIFIED

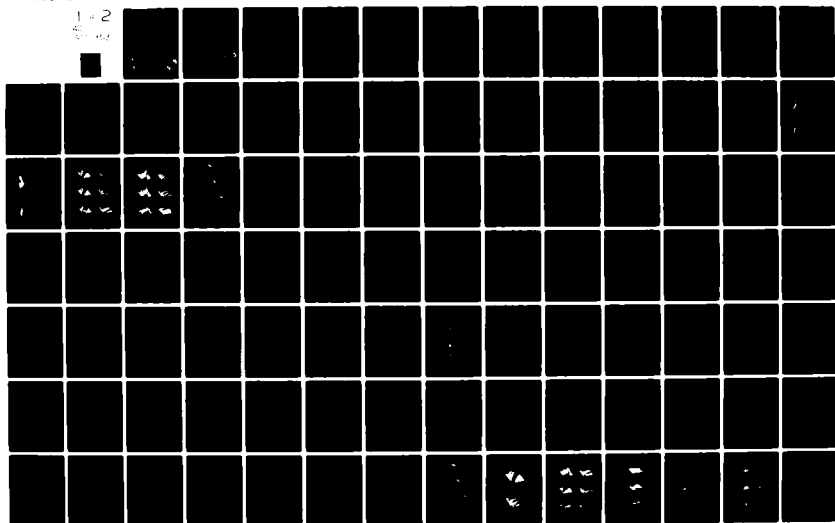
R-8144

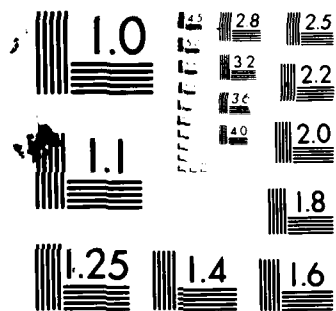
AFOSR-TR-82-0065

NL

1-2

1-2





MICROCOPY RESOLUTION TEST CHART  
NATIONAL BUREAU OF STANDARDS-1963-A

ADA111903

WEIDLINGER ASSOCIATES  
3000 SAND HILL ROAD  
BUILDING 4, SUITE 245  
MENLO PARK, CALIFORNIA 94025

**RESEARCH INTO SURFACE WAVE PHENOMENA  
IN SEDIMENTARY BASINS**

By

G.L. Wojcik  
J. Isenberg  
F. Ma  
E. Richardson

Prepared for

Air Force Office of Scientific Research  
Bolling AFB, Washington, D.C. 20332

and

Air Force Geophysics Laboratory  
Terrestrial Sciences Division  
Hanscom AFB, Massachusetts 01731

Final Report

AFOSR Contract F49620-80-C-0009

For the Period 1 October 1980 to 30 September 1981

Approved for public release;  
distribution unlimited.

DTIC FILE COPY

DTIC  
SELECTED  
MAR 11 1982  
H

82 03 11 114

WEIDLINGER ASSOCIATES  
3000 SAND HILL ROAD  
BUILDING 4, SUITE 245  
MENLO PARK, CALIFORNIA 94025

**RESEARCH INTO SURFACE WAVE PHENOMENA  
IN SEDIMENTARY BASINS**

By

G.L. Wojcik  
J. Isenberg  
F. Ma  
E. Richardson

Prepared for

Air Force Office of Scientific Research  
Bolling AFB, Washington, D.C. 20332

and

Air Force Geophysics Laboratory  
Terrestrial Sciences Division  
Hanscom AFB, Massachusetts 01731

Final Report

AFOSR Contract F49620-80-C-0009

For the Period 1 October 1980 to 30 September 1981

DTIC  
ELECTE  
MAR 11 1982  
H

DISTRIBUTION STATEMENT A

Approved for public release;  
Distribution Unlimited

UNCLASSIFIED

SECURITY CLASSIFICATION OF THIS PAGE (When Data Entered)

REPORT DOCUMENTATION PAGE		READ INSTRUCTIONS BEFORE COMPLETING FORM
1. REPORT NUMBER <b>AFOSR-TR- C2-0065</b>	2. GOVT ACCESSION NO. <b>AD-A111 903</b>	3. RECIPIENT'S CATALOG NUMBER
4. TITLE (and Subtitle)  RESEARCH INTO SURFACE WAVE PHENOMENA IN SEDIMENTARY BASINS		5. TYPE OF REPORT & PERIOD COVERED Final Report 1 Oct 1980 to 30 Sept 1981
7. AUTHOR(s) G. L. Wojcik                      E. Richardson J. Isenberg F. Ma		6. PERFORMING ORG. REPORT NUMBER R 8144
9. PERFORMING ORGANIZATION NAME AND ADDRESS Weidlinger Associates 3000 Sand Hill Road, Building 4, Suite 245 Menlo Park, California 94025		8. CONTRACT OR GRANT NUMBER(s)  F49620-80-C-0009
11. CONTROLLING OFFICE NAME AND ADDRESS Air Force Office of Scientific Research Bldg. 410, Bolling AFB, Washington, DC 20332		10. PROGRAM ELEMENT, PROJECT, TASK AREA & WORK UNIT NUMBERS  6110215 2309/A1
		12. REPORT DATE 31 December 1981
		13. NUMBER OF PAGES 108
		14. SECURITY CLASS. (of this report) UNCLASSIFIED
		15a. DECLASSIFICATION/DOWNGRADING SCHEDULE
16. DISTRIBUTION STATEMENT (of this Report)  Approved for public release; distribution unlimited.		
17. DISTRIBUTION STATEMENT (of the abstract entered in Block 20, if different from Report)		
18. SUPPLEMENTARY NOTES		
19. KEY WORDS (Continue on reverse side if necessary and identify by block number)  Minuteman Wing V                      Geology                      Sedimentary Prisms Seismic Alarms                      Denver Basin                      Surface Waves Seismology                      Green River Basin                      Ray Tracing		
20. ABSTRACT (Continue on reverse side if necessary and identify by block number)  This study is a continuation of an engineering seismology research effort prompted by the sensitivity of guidance sets in Minuteman Wing V to distant earthquakes. An earlier report considers the probable cause of anomalous patterns of seismic alarms triggered by two North American earthquakes. This report extends the previous study by examining the propagation of surface waves from the 1975 Pocatello Valley, Idaho earthquake sequence across Wyoming to Wing V. In addition, the more general question of		

UNCLASSIFIED

SECURITY CLASSIFICATION OF THIS PAGE (When Data Entered)

20. ABSTRACT (Continued)

surface wave phenomena in sedimentary basins is addressed, particularly the effect of laterally inhomogeneous (dipping) basin-bedrock interfaces. Findings indicate that fundamental and first overtone surface waves are significantly modified by the travel path. In contrast, higher modes are relatively unchanged by the travel path, and affect Wing V in much the same way as body waves considered in the previous study.

# ACKNOWLEDGMENTS

The work reported here benefited from information and comments by a number of individuals. Dr. Ker Thomson of the Air Force Geophysics Laboratory instigated the research effort and his support is gratefully acknowledged. Professors Amos Nur and George Thompson of Stanford University, and their graduate students, Carol Tosaya and Janice Hill, provided shale data and sediment velocity data, respectively. Their generosity is much appreciated. Conversations with Professors Donald Helmberger and Karen McNally of Caltech suggested useful sources of seismological data which materially benefited the work. Our colleague David Vaughan helped with some timely dispersion calculations, for which we are grateful.

In addition, the technical assistance and patience of Myrtle Carey, Penny Sevison and Edith Durfey in report preparation and data reduction is always a pleasure to acknowledge.

Approved for Release		<input checked="" type="checkbox"/>
Distribution/Availability Codes		
Dist		Special
A		

DTIC  
COPY  
INSPECTED  
2

# TABLE OF CONTENTS

<u>Section</u>		<u>Page</u>
1	INTRODUCTION. . . . .	7
	1.1 Travel Path Reconnaissance and Crustal Velocity. .	7
	1.2 Seismograms and Theoretical Interpretation . . . .	8
	1.3 Seismic Rays and Surface Waves . . . . .	9
	1.4 Prototype Problems and the Seismic Prism Analysis Method . . . . .	11
	1.5 Summary. . . . .	12
2	GEOLOGICAL AND SEISMOLOGICAL RECONNAISSANCE . . . . .	29
	2.1 The Regional and Seismic Setting . . . . .	29
	2.2 Travel Path Geology and Tectonics. . . . .	30
	2.3 Seismic Surveys and Velocity Models. . . . .	31
	2.4 Golden Seismograms . . . . .	33
	2.5 Observed and Theoretical Dispersion Data . . . . .	35
	2.6 Response of Denver Basin Sediments to Love and Rayleigh Waves . . . . .	37
3	SURFACE WAVES: A SEISMIC RAY THEORY PERSPECTIVE. . . .	47
	3.1 Mixed (Hyperbolic-Elliptic) Wave Fields Composing Surface Waves. . . . .	48
	3.2 Hyperbolic Wave Fields and Rays. . . . .	50
	3.3 Ray Tracing in Smooth Crustal Models . . . . .	53
	3.4 Equivalent Ray Beams and the Hyperbolic Solutions. .	56
4	SURFACE WAVES IN SEDIMENTARY PRISMS . . . . .	65
	4.1 Two-Point Ray Tracing in Sedimentary Prisms. . . .	66
	4.1.1 The self-similar system of rays . . . . .	67
	4.1.2 Rays to an interior point . . . . .	68
	4.1.3 The two-point solution. . . . .	69
	4.1.4 Amplitude and phase at the receiver . . . .	70
	4.1.5 Updip versus downdip ray tracing. . . . .	71
	4.2 Results of Love Wave Propagation in Sedimentary Prisms . . . . .	72
	4.2.1 Ideal free surface response . . . . .	73
	4.2.2 A comparison of response for both models. .	74
	4.2.3 Higher modes and response through depth . .	75
	4.2.4 Effects of material damping on surface response. . . . .	76
	4.3 Extension of Ray Tracing to P-SV-Waves in a Sedimentary Prism. . . . .	77
	4.3.1 Binary tree representation of rays. . . . .	77
	4.3.2 Leakage of surface wave energy at basin edges . . . . .	79



TABLE OF CONTENTS (CONCLUDED)

<u>Section</u>		<u>Page</u>
5	SUMMARY AND CONCLUSIONS . . . . .	99
	5.1 Summary. . . . .	99
	5.2 Conclusions. . . . .	101
6	REFERENCES. . . . .	104

# LIST OF FIGURES

<u>Figure</u>		<u>Page</u>
1-1	Tectonic map of Wyoming and adjacent states showing principal uplifts and basins. The Pocatello Valley epicenter is marked by a star on the border above the Great Salt Lake. . . . .	14
1-2	Travel paths and crustal velocity surveys in the area of interest . . . . .	15
1-3a	Sediment depth on 500 km of the travel path from Pocatello Valley to Wing V . . . . .	16
1-3b	Sediment depth on 250 km of the travel path from Pocatello Valley to the Golden, Colorado seismographic station . . . . .	17
1-4	P-wave velocity functions near the travel paths. . . . .	18
1-5	Long period WWSSN seismograms of a $M_L = 4.7$ , March 29, 1975 Pocatello Valley aftershock recorded at Golden, Colorado . . .	19
1-6a	Observed and theoretical Rayleigh wave dispersion data . . . .	20
1-6b	A comparison of first modes for 0, 2 and 5 km of sediment over the Flaming Gorge crustal model. . . . .	21
1-7a	Mantle and crustal P-rays in the Flaming Gorge crust with 5 km of overlying sediment. . . . .	22
1-7b	Shallow penetrating sediment P-rays in the Flaming Gorge crust with 3-5 km of sediments . . . . .	23
1-8a	Fundamental mode surface response for the 2 km layer and various dip angles . . . . .	24
1-8b	Fundamental mode surface response for the 5 km layer and various dip angles . . . . .	25
1-9	Leaked beams in a $3^\circ$ updipping transition with Love wave input	26
1-10	Schematic of a sedimentary basin . . . . .	27
1-11	Prototype waveguide models to be examined. . . . .	28
2-1	Sonic log data from nearby Wind River and Powder River Basin sediments compared to Faust's fit for shale/sandstone sections	39
2-2	Short period E-W WWSSN seismogram of a $M_L = 3.8$ March 28, 1975 Pocatello Valley aftershock recorded at Golden, Colorado. First minute mark on event trace is 16h17m . . . . .	40

# LIST OF FIGURES (CONTINUED)

<u>Figure</u>		<u>Page</u>
2-3	Observed fundamental mode Rayleigh wave group velocity and ellipticity at Golden, Colorado. . . . .	41
2-4	A comparison of Rayleigh wave dispersion for Sinclair and Flaming Gorge models with 3 km of sediment . . . . .	42
2-5	Dispersion curves for Wolcott model. . . . .	43
2-6a	Radial displacement ratios for fundamental mode Rayleigh waves	44
2-6b	Vertical displacement ratios for fundamental mode Rayleigh waves (see text for explanation) . . . . .	45
2-7	Displacement ratios for fundamental mode Love waves (see text for explanation) . . . . .	46
3-1	Components of surface wave motion. . . . .	58
3-2	Wavefronts in the hyperbolic channel . . . . .	59
3-3	Ray geometry . . . . .	60
3-4	Rays in the hyperbolic channel . . . . .	61
3-5	Phase velocities for first Rayleigh overtone (second mode) in the Flaming Gorge crust with 0, 3 and 5 km of sediment. . .	62
3-6	Surface wave ray system showing equivalent ray beams in a homogeneous prism joined to the halfspace. . . . .	63
3-7	The equivalent surface wave beam input and a schematic of ray interaction with a basin flank . . . . .	64
4-1	Prototype waveguide (a) and waveguide transition (b-d) models.	80
4-2	The equivalent Love wave transition model based on a ray beam projected into a prism . . . . .	81
4-3	The system of multiply-reflected rays in the prism (case of downdip) . . . . .	82
4-4	The graphical result of self-similarity, all rays tangent to a single circle. . . . .	82
4-5	The geometry of rays incident on an interior point at $R_n$ , $\Theta$ .	83
4-6	The totality of entering rays illuminating the receiver. . . .	83
4-7	The complete ray system for a ray shot in the updip direction.	84

# LIST OF FIGURES (CONCLUDED)

<u>Figure</u>		<u>Page</u>
4-8	The equivalent Love ray beam in a 7° downdip . . . . .	85
4-9	The equivalent Love ray beam in a 3° updip showing leaked beams. . . . .	86
4-10	An example of the 2 km waveguide fundamental Love mode surface response as a function of wave period and distance over the transition . . . . .	87
4-11	5 km waveguide fundamental and higher mode surface response over 5° updipping and downdipping transitions. . . . .	88
4-12	5 km layer mode shapes for the fundamental and first two overtones; given analytically by $ \cos \omega_1 z $ . . . . .	89
4-13	Examples of 2 km amplitude through depth in 5° updipping and downdipping transitions (see Fig. 4-10). . . . .	90
4-14	Effects of material damping on 2 km, 3° updip and downdip surface response . . . . .	91
4-15	A typical P-SV-ray cascade in a layer. . . . .	92
4-16	The ray fan in a prism, and the convention for drawing the binary tree for each ray of the fan. . . . .	93
4-17	P-ray binary trees for the 10° prism in Fig. 16a. Ratio of P to SV velocity is 1.5 in the prism. . . . .	94
4-18	S-ray binary trees for the 10° prism . . . . .	95
4-19a	Leaked rays from a 10° prism for an incident P-ray. Upper number is amplitude and lower is angle from vertical in degrees (negative sign for updip). Rays in prism are pruned to an amplitude of 10% of incident ray . . . . .	96
4-19b	Leaked rays for an incident S-ray. . . . .	97
4-20	A ray fan in the Sinclair crustal model with no sediment. The fan is from 34° to 55° in increments of 1° and illustrates the paths of leaked rays into bedrock. . . . .	98

## SECTION 1

### INTRODUCTION

This work is a continuation of an engineering seismology research effort prompted by the observed sensitivity of Minuteman Wing V to distant earthquakes. An earlier report, "Site Dependent Ground Motions from Distant Earthquakes," Wojcik et al. [1980], considered the probable cause of anomalous patterns of seismic alarms triggered by two North American earthquakes--1975 Pocatello Valley, Idaho ( $M_L = 6$ ) and 1979 St. Elias, Alaska ( $M_S = 7.1$ ). It concluded that body waves amplified by the 2-3 km sedimentary layer under Wing V, near longer period, lightly damped resonances of the missile suspension system were probably responsible for the patterns. Layered halfspace calculations indicated that peak ground shaking in the period window of interest could vary by a factor of two at adjacent missile flights.

The present research report extends the previous study by examining the propagation of Love and Rayleigh surface waves from the Pocatello Valley, Idaho event across Wyoming to Wing V. In addition, the more general question of surface wave phenomena in sedimentary basins is addressed, particularly the effect of laterally inhomogeneous (dipping) basin-bedrock interfaces. The report includes a reconnaissance of geology, tectonics and velocity functions on the surface wave travel paths; an examination of relevant seismograms and associated dispersion calculations to pick the "best" crustal model; and ray theory analyses to show the effects of travel path inhomogeneities on natural surface waves.

#### 1.1 Travel Path Reconnaissance and Crustal Velocity

The 700 km travel path from the Pocatello Valley epicenter to Wing V (70 km east of Cheyenne, Wyoming) includes 180 km of the Idaho-Wyoming overthrust

belt, 350 km of the Green River Basin of Wyoming and about 170 km of the Laramie Range and Denver Basin (see Fig. 1-1). It is structurally complex, including inhomogeneities in the upper crust (deep sediments over irregular bedrock, faults and mountainous uplifts), as well as variable depth to Moho (across the Laramie Range) and variable upper mantle velocities (based on  $P_n$  earthquake phases).

Figure 1-2 shows travel paths from the Pocatello Valley epicenter to Wing V, and from the epicenter to the Golden, Colorado seismographic station. Sediment depth over these two paths are shown in Fig. 1-3. A number of seismic surveys have been conducted near these paths. Most relevant are refraction surveys made by the USGS which cross one or both paths as shown. The western line runs southeast from the Snake River Downwarp (Fig. 1-1) across the Overthrust Belt to Flaming Gorge, near the Utah-Wyoming border. The eastern survey runs south from Sinclair, Wyoming through Wolcott, Colorado, paralleling the Central and Southern Rocky Mountains.

Velocity functions are shown in Fig. 1-4 for the Flaming Gorge model in western Wyoming and the Sinclair and Wolcott models to the east. These indicate a nominal crustal thickness of 40 km which thickens to about 48 km across a northeast trending shear zone indicated in Fig. 1-1.

## 1.2 Seismograms and Theoretical Interpretation

Seismograms of the 1975 Pocatello Valley earthquake sequence were recorded on bedrock at Golden, Colorado (see Fig. 1-5). These are the closest available records to Wing V and are expected to suggest its ground motion history. The main shock drove the instruments off scale for over five minutes providing no useful data, but numerous fore and aftershocks were well recorded. The short period seismograms showed the usual sequence of arrivals for a local event, e.g.  $P_n$ ,  $P_g$ ,  $S_g/L_g$  but detailed period data could not be inferred. However,

a long period seismogram of a  $M_L = 4.7$  aftershock, shown in Fig. 1-5, provided useful dispersion data. The wave arrival time and particle motion polarization indicated that these were fundamental mode Rayleigh waves.

From the dispersed train of surface waves shown in Fig. 1-5, dispersion (arrival time vs. period) and particle motion (ellipticity) data were deduced. These are shown in Fig. 1-6a. The retrograde elliptical path identifies the phase as a Rayleigh wave. The measured group velocity data were used to find the "best" average travel path model. The theoretical first and second mode dispersion curves shown were for the Flaming Gorge crust with 2 km of sediment. For comparison, the first mode for zero, two and five kilometers of sediment is drawn in Fig. 1-6b. Figure 1-6a indicates a group velocity minimum corresponding to Airy phases may be present in the 2 to 4 second period range, to which Wing V has proven sensitive.

### 1.3 Seismic Rays and Surface Waves

Surface waves are usually analyzed from a modal viewpoint. In laterally inhomogeneous structure a ray theory perspective is more useful because rays are easily continued through inhomogeneities, while modal solutions are not. A suite of ray fans in the Flaming Gorge crust, Fig. 1-4, are drawn in Figs. 1-7a,b for various penetration scales. Accompanying these are reduced travel-time curves. Figure 1-7a shows mantle and crustal P-rays while Fig. 1-7b shows sedimentary P-rays. A correspondence between such rays (including S-rays which are not shown) and surface wave phases exists and can be used to deduce the depth of component ray penetration as a function of surface wave period. The finding is that fundamental mode Love and Rayleigh waves and the first Rayleigh overtone in the 3-4 second period range of importance to Wing V are composed of rays which penetrate to relatively shallow depths, e.g. on the order of

7 km or less. Therefore, these surface waves would be expected to interact with near surface lateral inhomogeneities shown in Fig. 1-3.

To determine what effect near surface, lateral inhomogeneities, such as the 3°-5° updip in Fig. 1-3b, have on shallow surface waves, two-point ray tracing calculations have been performed in prismatic structure. An example is shown in Fig. 1-8a for a layer over halfspace, modeling the updipping geology in Fig. 1-3b as well as a corresponding downdip. The input is a fundamental mode Love wave for a range of periods. For updip the surface response amplitude as a function of distance over the transition shows amplification followed by a rapid cutoff. Amplification is due to the converging geometry and the cutoff occurs because the component rays leak into the lower halfspace, to emerge elsewhere depending on their takeoff angle. A similar suite of plots is drawn in Fig. 1-8b for different dip angles and waveguide thicknesses, for comparison. The qualitative features are similar.

The most pronounced effect of Love waves into an updipping transition is the distinct cutoff at some distance, depending on surface wave period. The cutoff is due to energy leakage into the lower halfspace and the question is where does this energy go. This is useful to know because it involves the idea of detection--particularly the question of deducing activity within a basin from seismic signals recorded outside. Figure 1-9 shows the mechanism of leakage. For Love waves into an updip, the energy is transmitted as distinct ray beams into the halfspace. By ray tracing, it is simple to determine where these beams will re-emerge on the surface.

The results shown above for Love waves propagating into prisms in Fig. 1-8a,b are an intermediate result of a more general study addressing the question of Rayleigh and Love type ducted surface waves within a basin interacting with dipping bedrock interfaces. Such interfaces are common near basin edges,



as well as under smooth depth transitions in the basin interior, Fig. 1-10. The fill is idealized as a dissipative homogeneous, isotropic elastic medium. Underlying bedrock is similarly elastic, but with higher seismic wavespeeds. Scale of the basins may be on the order of tens to hundreds of kilometers.

This idealization provides a prototype model from which fundamental surface wave reflection and transmission phenomena can be recognized and quantified. Relevant effects include: patterns of amplification and attenuation over the free surface; energy leakage and its dependence on interface geometry and surface wave type; influence of material damping, fill depth, impedance contrast, etc. The purpose of the analysis is to provide both qualitative and quantitative data for the analyst who must assess anomalous wave effects and seismic hazard due to surface waves in real geologies.

#### 1.4 Prototype Problems and the Seismic Prism Analysis Method

Three prototype problems are examined. They are illustrated in Fig. 1-11, each consisting of an upstream waveguide supporting a single mode Love wave, connected to a converging or diverging layer. Figure 1-11a shows an updipping layer which terminates at the vertex; Fig. 1-11b shows a downdipping layer which does not terminate; and Fig. 1-11c illustrates the more general case of a dipping layer connecting waveguides of different depth, which includes the other two as special cases (and is not analyzed). These models exhibit most relevant physics of the natural features at some level of idealization.

In general, prototype models are very useful in seismic analysis of complex structure. For example, Love's prototype waveguide, so important in early seismology, was the homogeneous layer over a halfspace, Love [1911]. The examples examined here are the simplest generalization of this basic model to laterally inhomogeneous waveguides.

The mathematical analysis of surface waves in the prototype models is based on a ray decomposition of the incident surface wave, yielding a two-point ray tracing problem in a so-called seismic prism. The prism models the dipping layer and is analyzed on the basis of self-similarity. An exact solution is found for all Love-wave-derived rays using a canonical solution for rays in the prism. The Rayleigh wave ray solution, which may involve thousands of P- and SV-waves, is conveniently displayed by a binary tree data structure. The complete ray theory has yet to be implemented.

Secondary rays, associated with diffraction, are free surface Rayleigh waves, head waves and cylindrical waves. These are not included in asymptotic ray theory. To include them requires a canonical solution for edge diffraction in elastic media. The continuation of such diffracted solutions away from the diffractor proceeds by ray tracing, as in the geometrical theory of diffraction, Keller [1958].

### 1.5 Summary

There are three basic questions motivating the research:

1. What was the causative wave type for Wing V alarms?
2. What are the response anomalies due to surface waves through inhomogeneous waveguides?
3. How does surface wave energy leak out of basins and where does it go?

Question 1 relates directly to the Wing V alarm problems from the Pocatello Valley quake. Travel path from Pocatello Valley to Wing V was through a number of geologies across Wyoming, all characterized by thinning of sedimentary cover in the direction of propagation. Gross features described in a previous report indicate convergence in both azimuth and depth (funneling). Previous work does not explain what effects this has on surface waves on the

period range of interest (1-5 sec). The present work indicates that the updip across Wyoming may filter out certain 1-5 second waves.

Question 2 addresses the problem of anomalous response in a nonuniform basin due to surface waves. For example, the effects on surface waves at Wing V of the highland/lowland depth change and of interface steps or transitions are examined below as well as the effects of the Western Rocky Mountain flank on surface waves. The results bear on the general question of basing sensitive structures near basin edges or near other waveguide inhomogeneities.

Question 3 concerns the seismic detection problem. For a source within a basin (moving or stationary) most energy is trapped except for direct body waves which escape. We find that the trapped surface wave energy is projected out of the basin as diffraction limited ray beams at the updipping edges or transitions. In the sequel these effects are quantified on the basis of geometry, wave type, impedance contrasts, etc. Typical take-off angles and crustal ray paths will be described for these leaky beams.

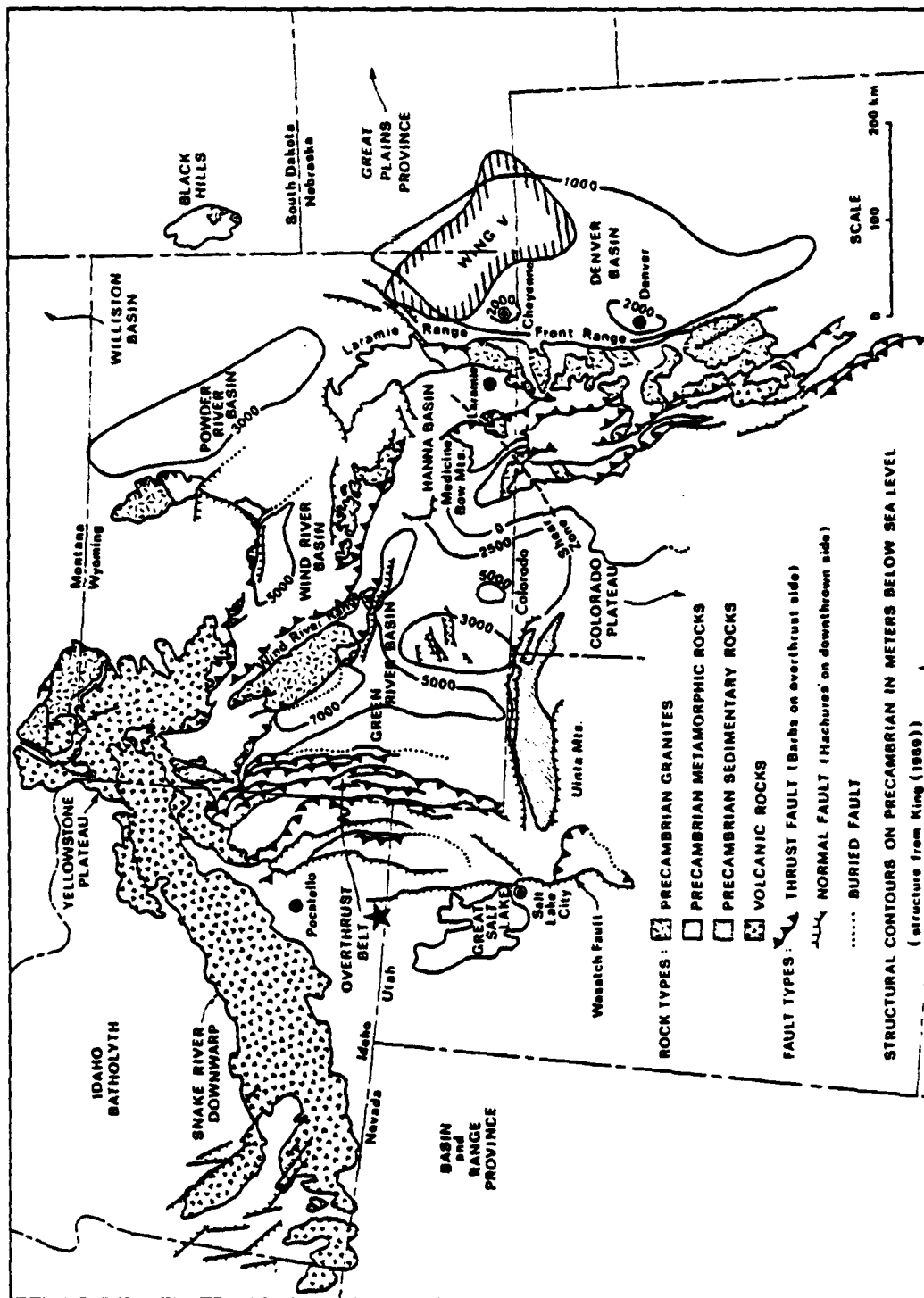


Figure 1-1. Tectonic map of Wyoming and adjacent states showing principal uplifts and basins. The Pocatello Valley epicenter is marked by a star on the border above the Great Salt Lake.

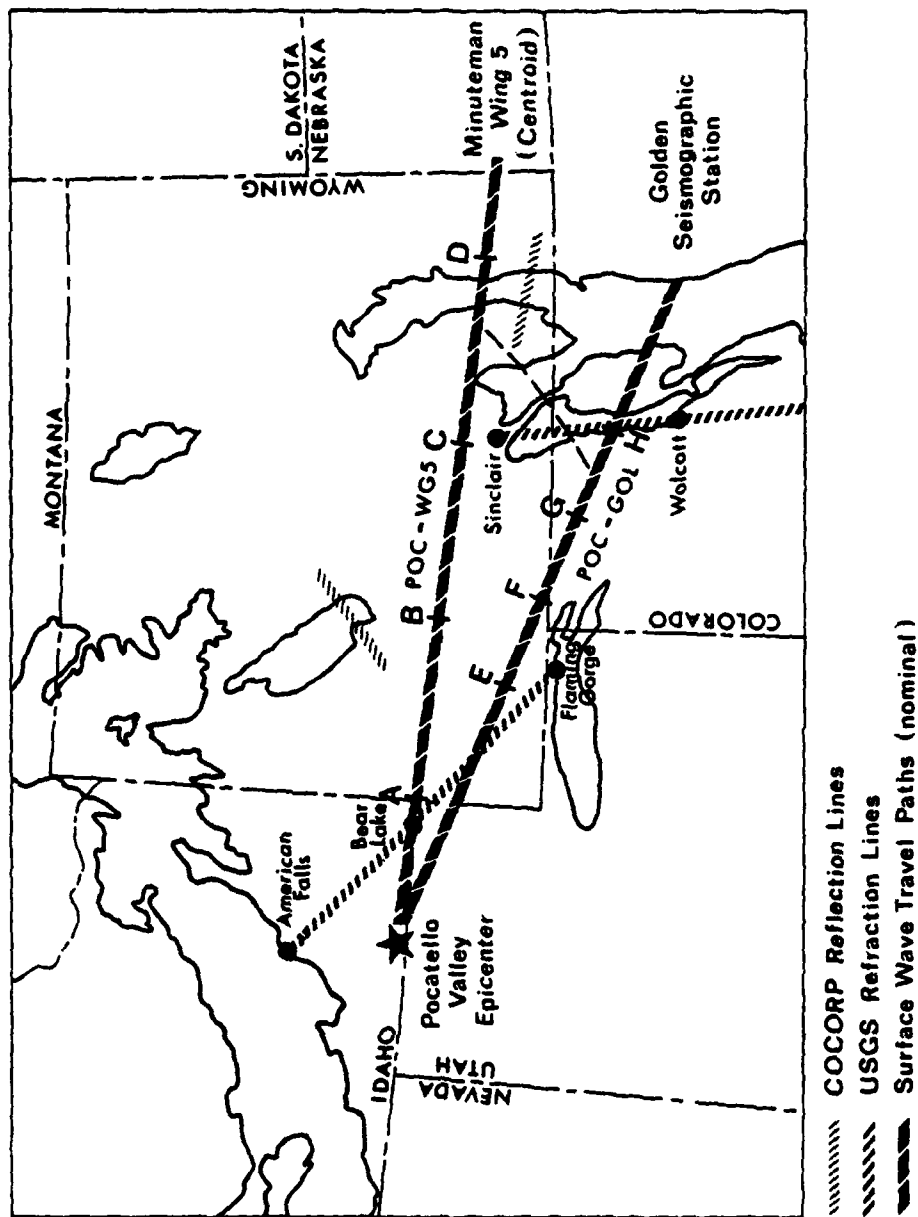


Figure 1-2. Travel paths and crustal velocity surveys in the area of interest.

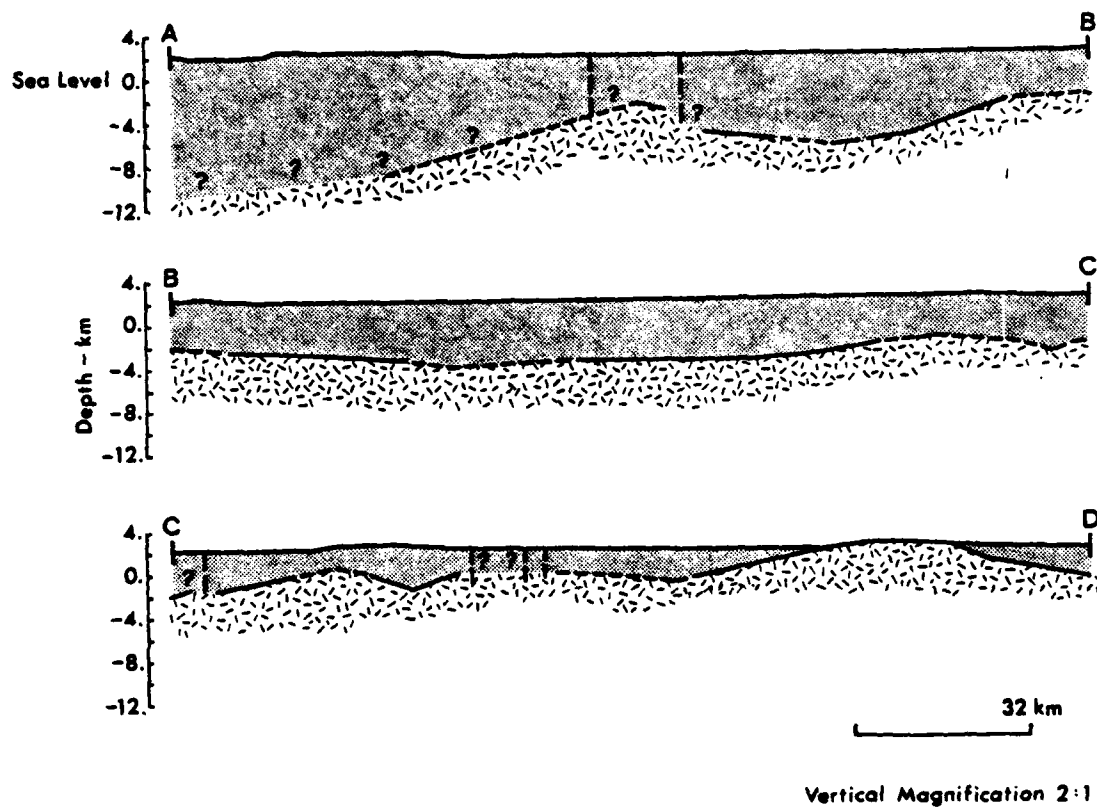


Figure 1-3a. Sediment depth on 500 km of the travel path from Pocatello Valley to Wing V.

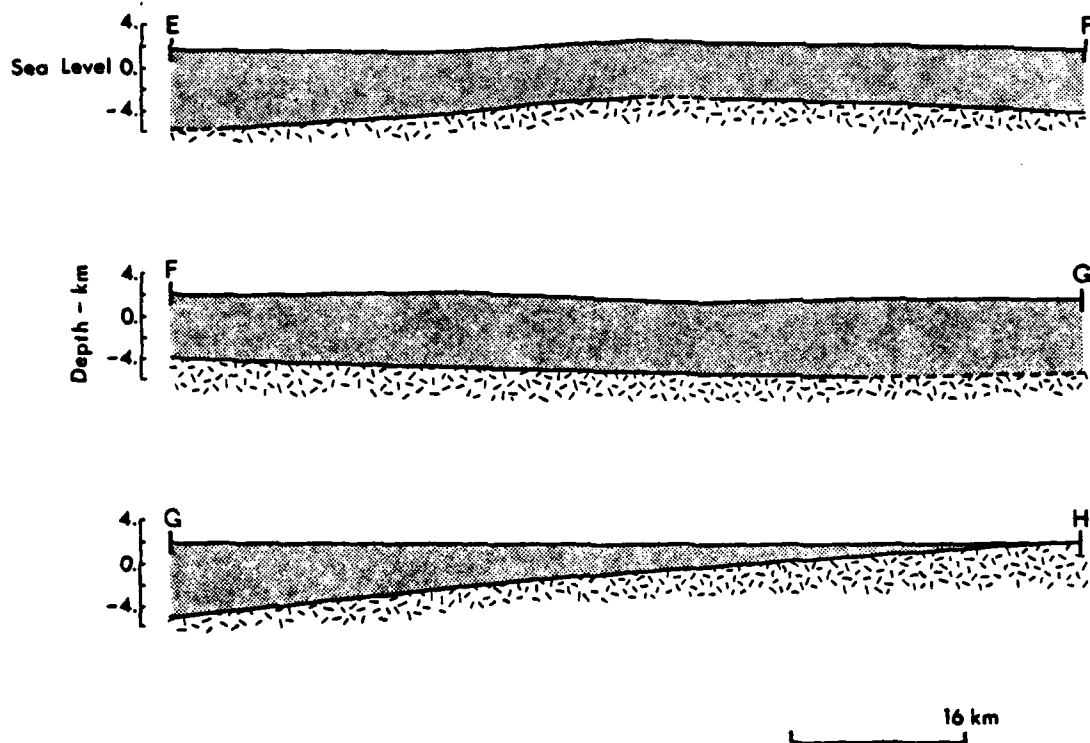


Figure 1-3b. Sediment depth on 250 km of the travel path from Pocatello Valley to the Golden, Colorado seismic station.

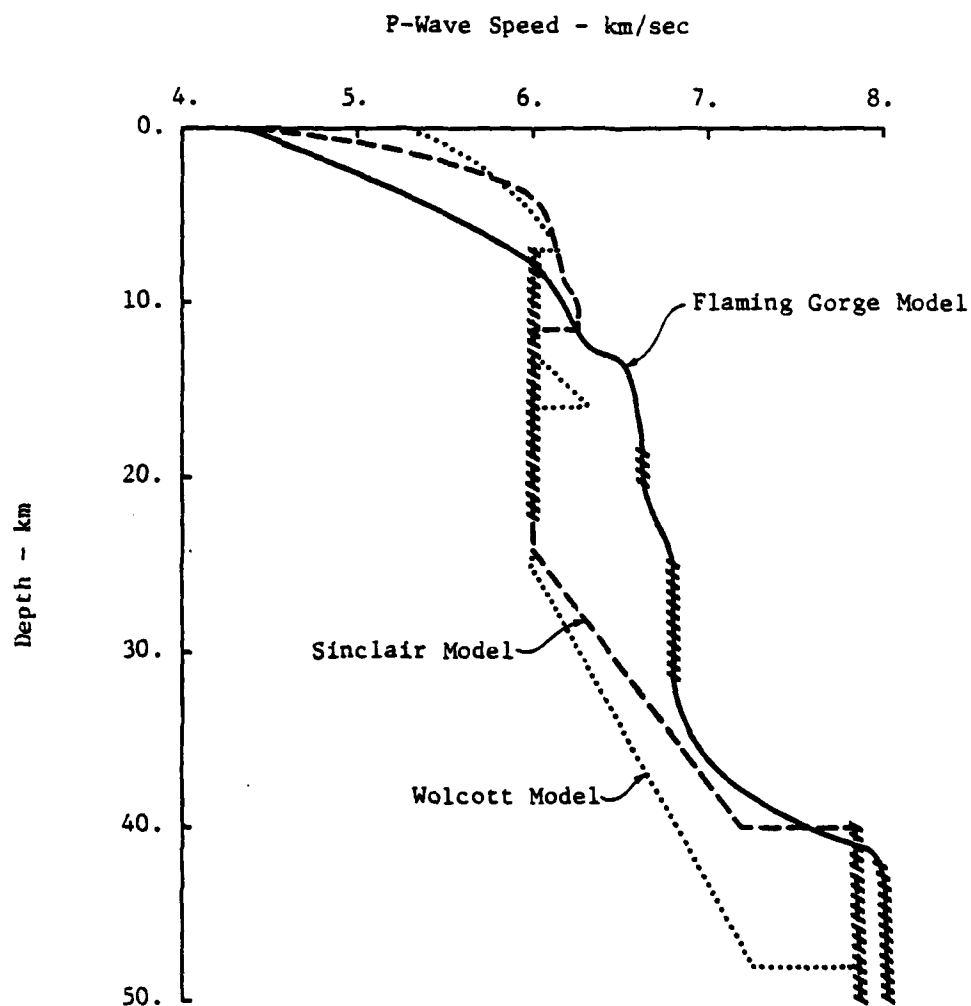
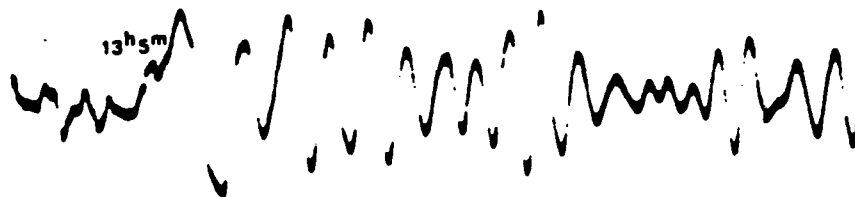


Figure 1-4. P-wave velocity functions near the travel paths.





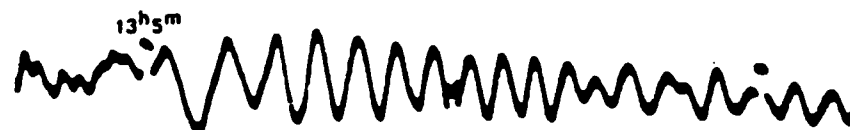
Vertical Component



North-South Component



East-West Component



Pocatello Valley aftershock: origin time  $13^h 1^m 20^s$



Figure 1-5. Long period WWSSN seismograms of a  $M_L = 4.7$ , March 29, 1975 Pocatello Valley aftershock recorded at Golden, Colorado.

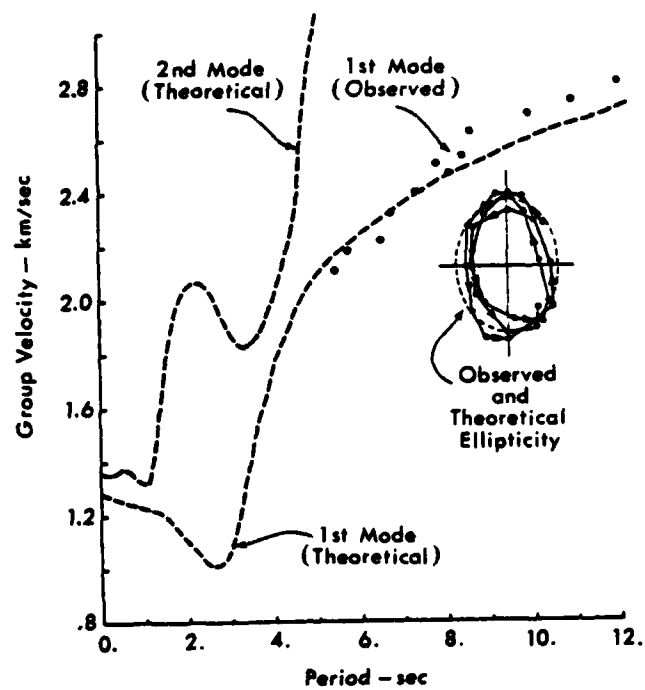


Figure 1-6a. Observed and theoretical Rayleigh wave dispersion data.

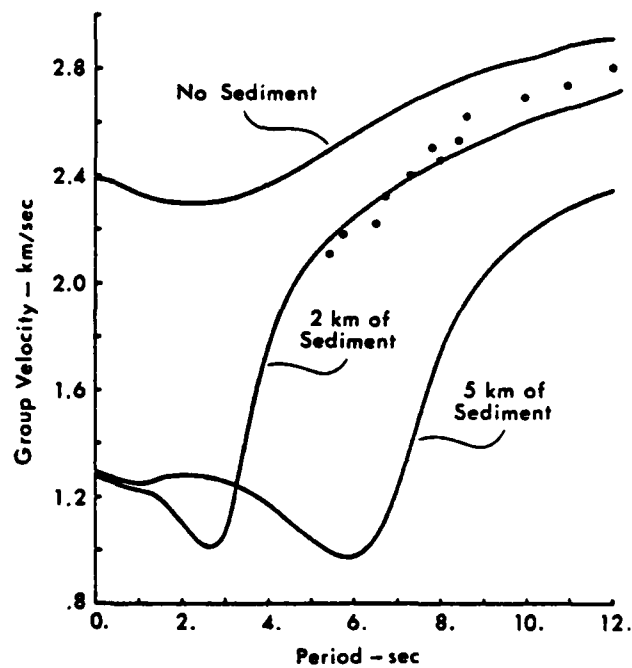
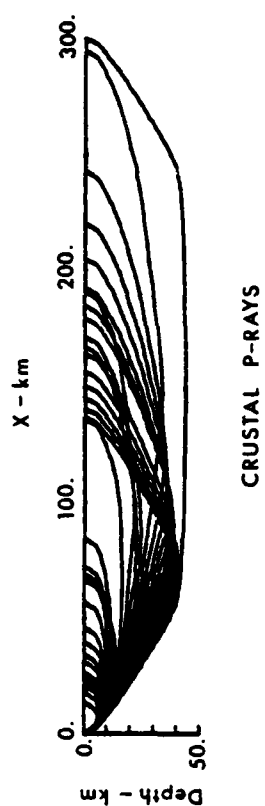
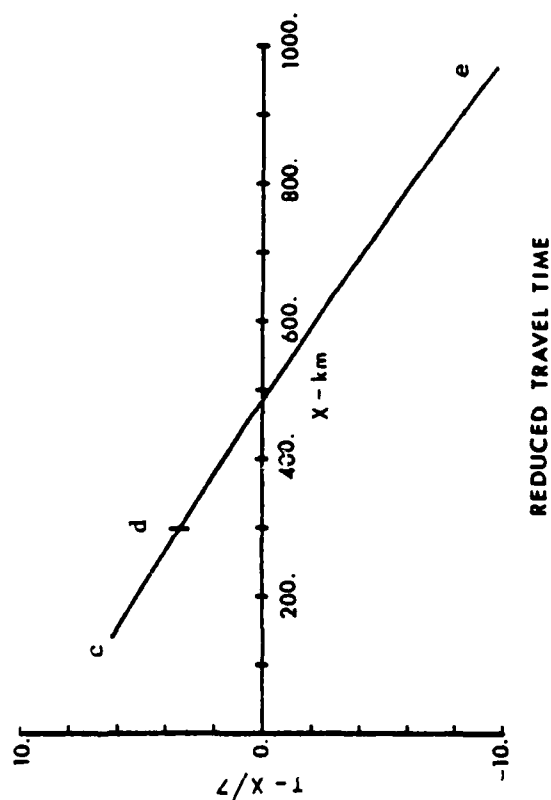


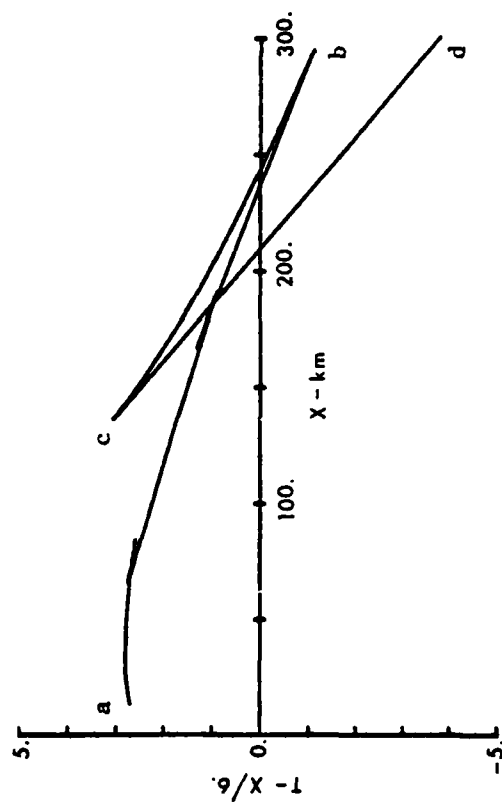
Figure 1-6b. A comparison of first modes for 0, 2 and 5 km of sediment over the Flaming Gorge crustal model..



MANTLE P-RAYS

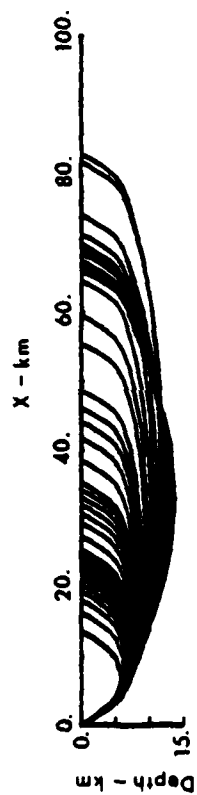


REDUCED TRAVEL TIME

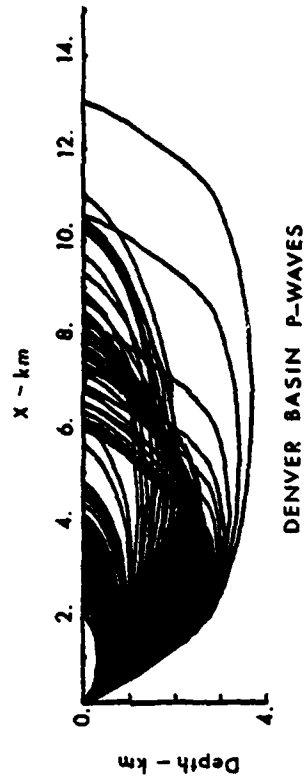


REDUCED TRAVEL TIME

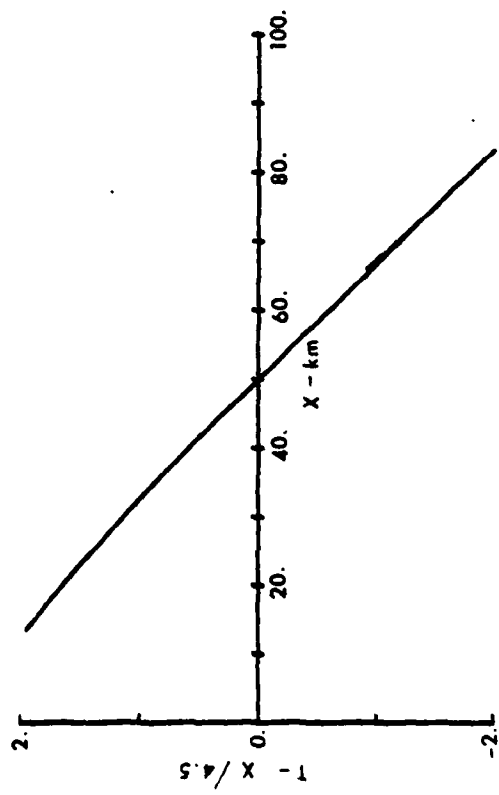
Figure 1-7a. Mantle and crustal P-rays in the Flaming Gorge crust with 5 km of overlying sediment.



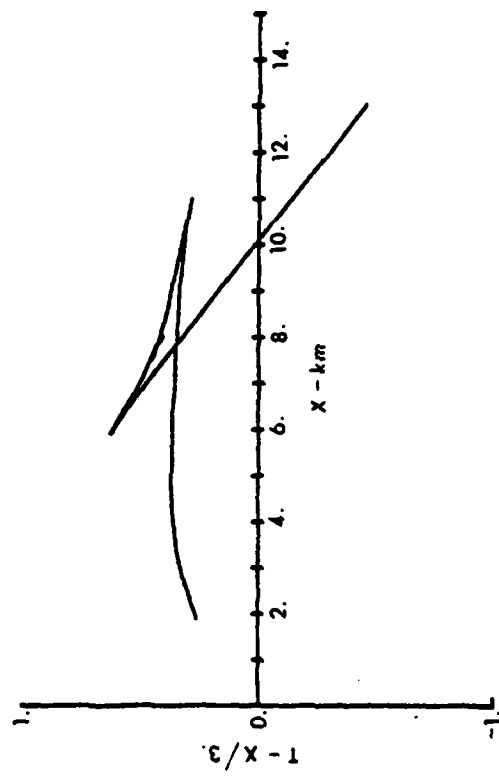
DEEP SEDIMENT P-WAVES



DENVER BASIN P-WAVES



REDUCED TRAVEL TIME



REDUCED TRAVEL TIME

Figure 1-7b. Shallow penetrating sediment P-rays in the Flaming Gorge crust with 3-5 km of sediments.

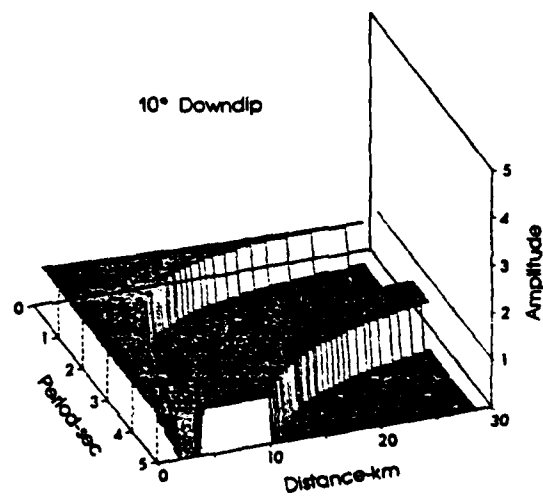
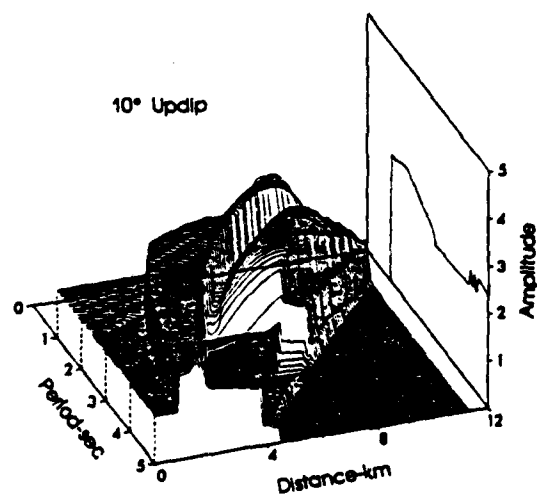
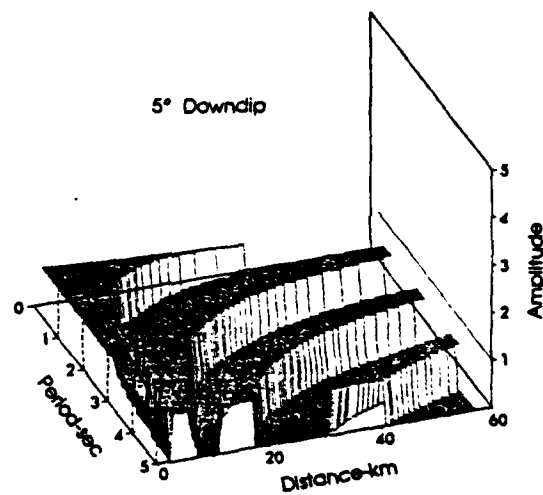
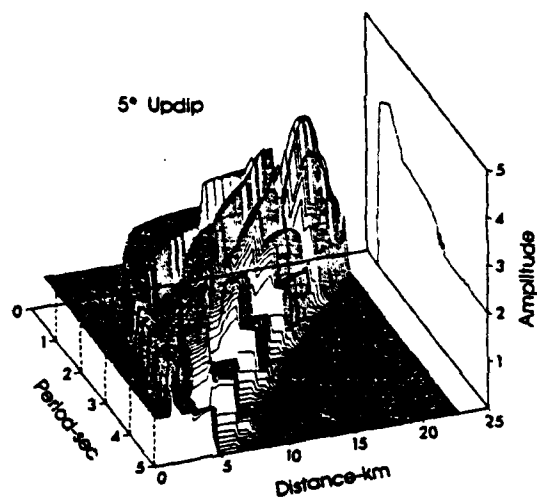
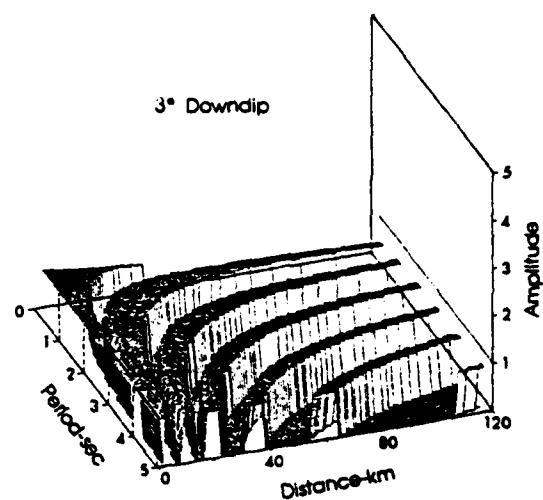
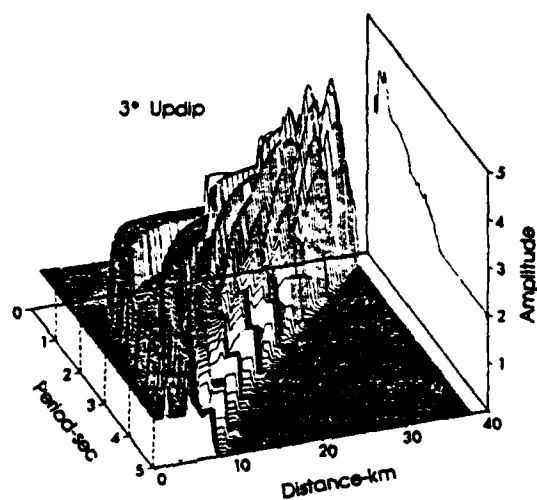


Figure 1-8a. Fundamental mode surface response for the 2 km layer and various dip angles.

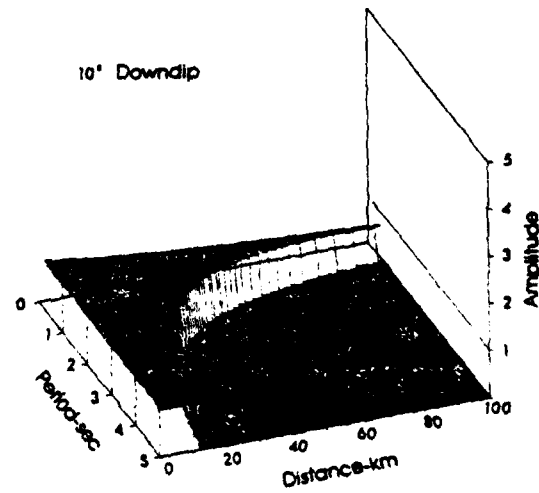
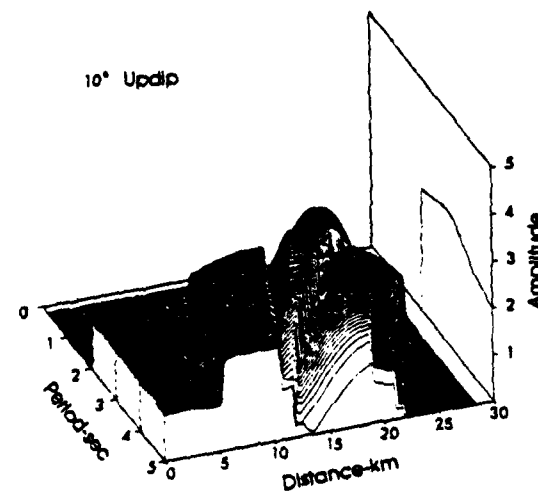
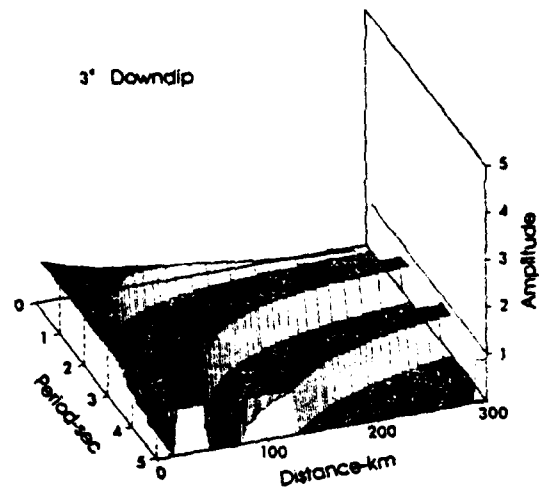
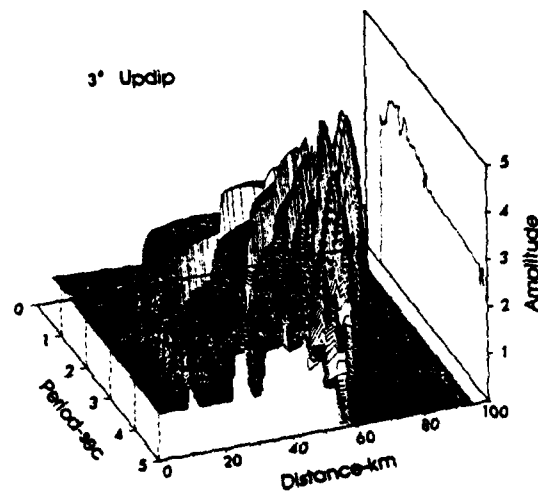
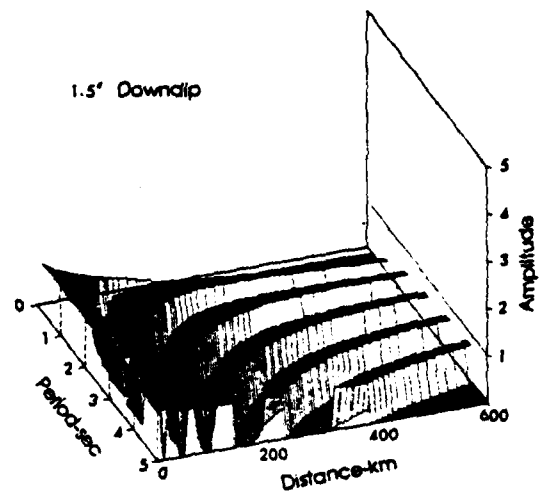
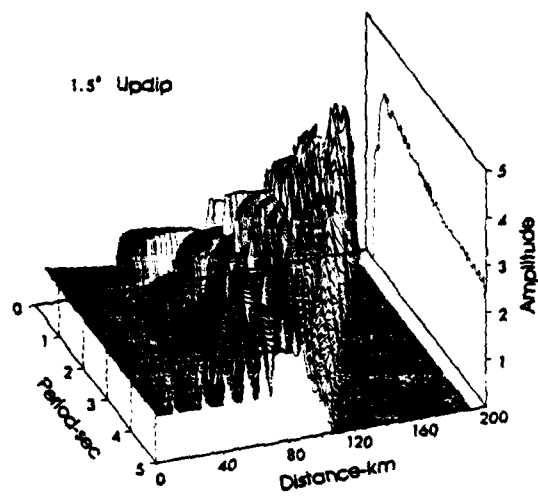


Figure 1-8b. Fundamental mode surface response for the 5 km layer and various dip angles.

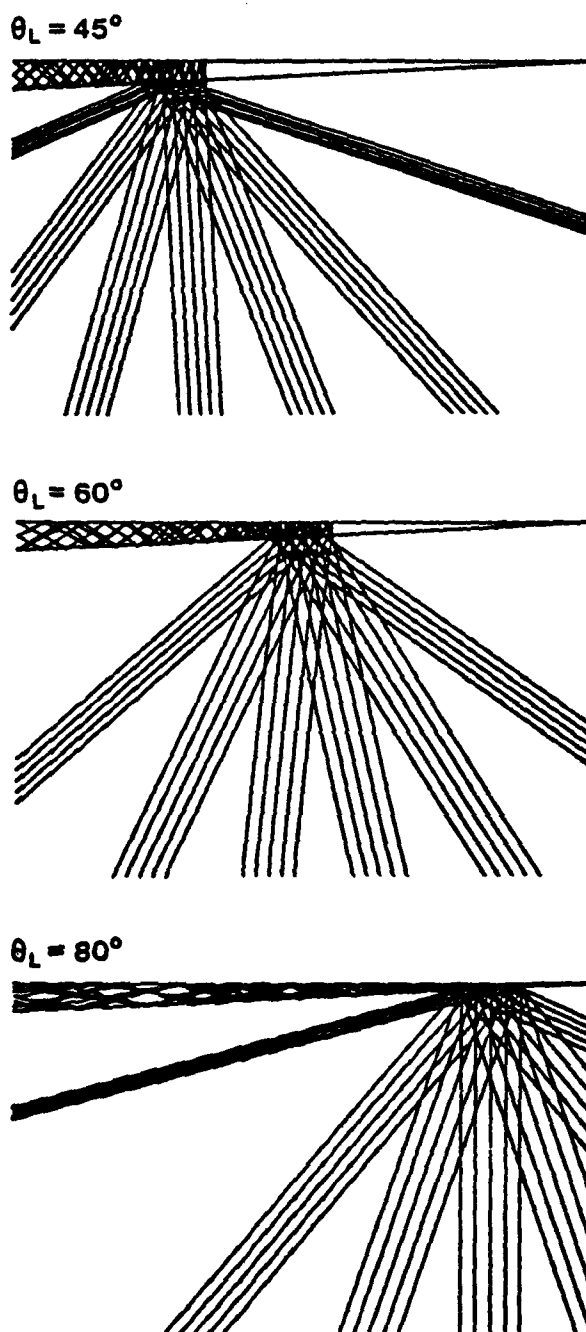


Figure 1-9. Leaked beams in a 3° updipping transition with Love wave input.



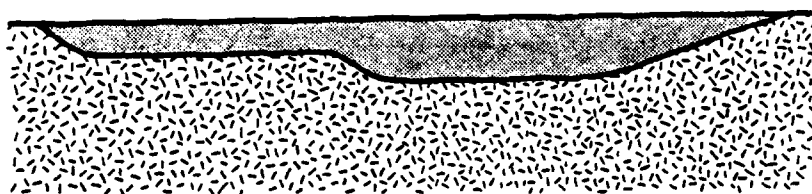
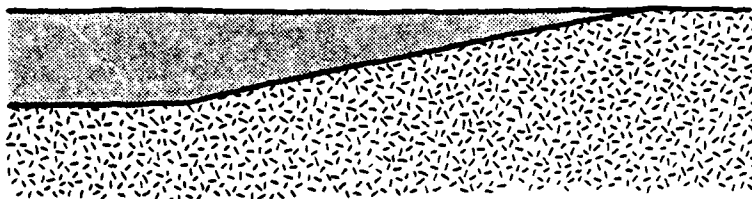
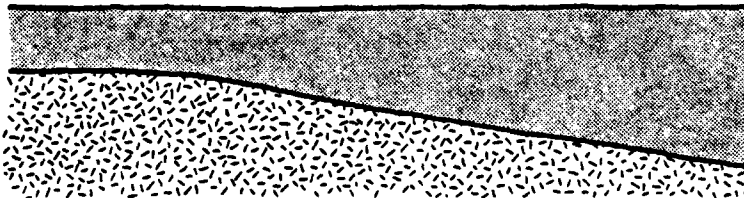


Figure 1-10. Schematic of a sedimentary basin.

a. Converging, terminating waveguide



b. Diverging, non-terminating waveguide



c. Transitional waveguide

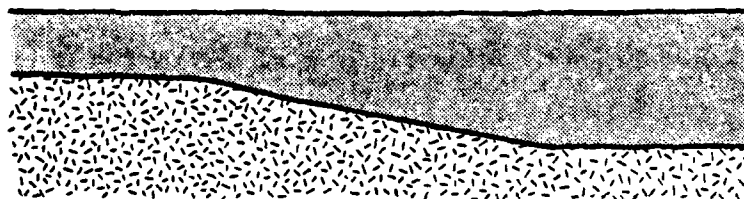


Figure 1-11. Prototype waveguide models to be examined.

## SECTION 2

### GEOLOGICAL AND SEISMOLOGICAL RECONNAISSANCE

This section presents a reconnaissance of geologic, tectonic and seismic data in the neighborhood of surface wave travel paths from the Pocatello Valley epicenter to both Wing V and a seismographic station near Golden, Colorado. It includes a description of near-surface structure, lateral inhomogeneities in the deep sediment-bedrock interface, and velocity models for sedimentary and crustal sections. Seismograms of the Pocatello Valley event, recorded on Rocky Mountain bedrock 150 km south of Wing V, are described and reduced to crustal dispersion data for fundamental mode Rayleigh waves with periods greater than 5 seconds. In conjunction with theoretical dispersion calculations, the seismographic data are used to deduce dispersion curves in the period window of interest--1 to 5 seconds.

#### 2.1 The Regional and Seismic Setting

Wing V is distributed over the tri-state area of Wyoming, Nebraska and Colorado in the northern Denver Basin (Julesburg Basin) between the North and South Platte Rivers. It is bounded to the west by the Laramie and Front Ranges of the Central and Southern Rocky Mountains, and to the east by the Great Plains of Central North America. The areal extent and neighboring tectonic features are illustrated in Fig. 1-1, King [1969], showing principal uplifts and sedimentary basins. Structure to the west is dominated by the Cordilleran system of mountains, basins and plateaus extending 800-1600 kilometers inland from the Pacific Coast along the length of North America. Of principal interest here is the eastern part of the system which was deformed most recently during the Laramide orogeny towards the end of the Mesozoic era, King [1977].

The Pocatello Valley earthquake sequence of late March and April, 1975 was centered around the main shock ( $M_L = 6.0$ ) in an area just north of the Idaho-

Utah border at 42.1°N, 112.5°W. The locus of epicenters, Arabasz et al. [1981] is indicated by a star above the Great Salt Lake in Fig. 1-1. Historically, this is a region of high seismicity within the southern Intermountain Seismic Belt, Smith and Sbar [1974]. The most significant recent events in the area were the 1934 Hansel Valley ( $M = 6.6$ ) and the 1962 Cache Valley ( $M = 5.7$ ) earthquakes, both within 75 km of the Pocatello Valley epicenter. Structurally, the Pocatello Valley area is a 10 x 15 km northern trending sediment filled graben on the eastern margin of the Basin and Range province. Arabasz et al. [1981] conclude that the 1975 earthquake sequence accompanied irregular graben subsidence within the valley.

## 2.2 Travel Path Geology and Tectonics

Travel paths from the Pocatello Valley epicenter (POC) to Wing V (WG5), and to the Golden seismographic station (GOL) are drawn in Fig. 1-2. The 700 km path from POC to WG5, across the lower third of Wyoming, includes about 180 km of the Idaho-Wyoming Overthrust Belt, 350 km of the Green River Basin (across the Continental Divide) and 170 km of the Laramie Range and Denver Basin (see Fig. 1-1). The 650 km path from POC to GOL includes perhaps 150 km of the southerly extension of the Overthrust Belt, 350 km of the Green River Basin paralleling the Uinta Mountains and 150 km across the Front Range.

The mountains and uplifts near the travel paths in Wyoming and Colorado were affected most recently by the Laramide orogeny, beginning in late Cretaceous time. The orogeny created great vertical uplifts and the present structures developed from rocks of the ancient continental platform. Heavily metamorphosed, steeply tilted precambrian rocks form most of the mountain cores. A discontinuity in rock type occurs across the northeast trending shear zone (Mullen Creek-Nash Fork Shear Zone) shown in Fig. 1-2. The overall surface

structure has since been modified by processes during Tertiary time. These include basin formation and regional uplift responsible for the present height of the Rockies. Streams invigorated by the uplift have etched out the ranges and filled the basins.

The depth of basin sediments (late Paleozoic to early Tertiary) covering Precambrian basement rock is shown in Fig. 1-3a,b for segments on both travel paths indicated in Fig. 1-2. These are drawn from state topographic maps and the tectonic map of North America. The cross sections show non-uniform cover, generally thinning towards the east with the interface dipping intermittently on the order of  $2^{\circ}$  to  $10^{\circ}$ . The POC-WG5 path is the more variable of the two, exhibiting both updips and downdips as well as significant azimuthal variations. The variability with azimuth forms a crude three-dimensional channel bounded abruptly by the Wind River Range and associated faults and uplifts to the north, converging into the Hanna Basin. The POC-GOL path is more uniform but with an 80 km  $5^{\circ}$  updip terminating on the western flank of the Rocky Mountains. The most significant azimuthal variations occur on the flank of the Uinta uplift to the south.

### 2.3 Seismic Surveys and Velocity Models

Seismic velocity data near the POC-WG5 and POC-GOL travel paths are available from a variety of sources including oil well sonic logs (near surface) and seismic reflection and refraction surveys (deeper structure). Refraction and reflection surveys conducted by USGS and COCORP, respectively, are indicated in Fig. 1-2. Of principal use here are reinterpretations of the USGS data by Prodehl [1979] and Prodehl and Pakiser [1980] using smooth velocity functions rather than the conventional but approximate piecewise constant functions. The western refraction line in Fig. 1-2 runs southeast from the Snake River Downwarp, across the Overthrust Belt to Flaming Gorge near the Utah-Wyoming border.

The eastern refraction line runs south from Sinclair, Wyoming through Wolcott, Colorado, paralleling the Central and Southern Rocky Mountains. Of more qualitative use are the COCORP deep reflection profiles across the Wind River and Laramie Ranges in Wyoming. These provide a striking picture of tilted prismatic structure in the Ranges and surrounding deep sediment, e.g. Smithson et al. [1979], as well as mapping a rapid increase in Moho depth across the Nash Fork-Mullen Creek Shear Zone, Allmendinger [1980].

Velocity functions are shown in Fig. 1-4 near Flaming Gorge on the western line, and Sinclair and Wolcott on the eastern. The cross hatching indicates questionable values associated with possible low velocity zones in the crust, and the mantle velocity gradient below the Moho. The Flaming Gorge and Sinclair models show a depth to Moho of about 40 km while the Wolcott Moho is near 48 km. The eastern models indicate a low velocity zone in the upper crust common to the region immediately west of the Front Range in Colorado, Prodehl and Pakiser [1980], but absent in the more westerly Flaming Gorge model, Prodehl [1979]. Upper crust velocities are significantly higher on the eastern line in contrast to the western because the latter survey sampled deep sediments between Bear Lake and Flaming Gorge, while the former sampled Rocky Mountain bedrock between Sinclair and Wolcott. Note in Fig. 1-2 that the eastern line crosses the northeast trending shear zone which marks a discontinuity in surface rock type.

Although the Wolcott velocity function south of the shear zone exhibits a more complicated low velocity zone compared to Sinclair, as well as higher near-surface velocity, the principal difference is depth to Moho. Based on the Laramie Range COCORP reflection line data, Allmendinger [1980] found that the depth transition correlates with the Mullen Creek-Nash Fork Shear Zone indicated. This implies that the Shear Zone is a crustal rather than surficial feature, possibly extending into the mantle. Therefore, the Wolcott model is presumed

to be representative of crustal structure east of the Shear Zone, particularly under the Denver Basin. It is consistent with a layered interpretation of USGS refraction data in eastern Colorado by Jackson et al. [1963].

The above crustal models do not include velocities in near-surface sedimentary rock. They can be augmented, however, employing sonic oil well logs in the shales and sandstones ubiquitous to the basins on and around the travel paths in Fig. 1-2. The most significant recent basin fills are of Eocene age, deposited after the climax of the Laramide orogeny. For example, the Green River Basin contains thick Eocene beds of oil shale. These lay unconformably on older sedimentary rocks, chiefly Mesozoic and late Paleozoic, King [1977]. Examples of sonic log data reduced by Thompson et al. [1981] from the Wind River and Powder River Basins are plotted in Fig. 2-1. Velocity depends on depth and rock type; for shales and sandstones the dependence has been extensively studied, e.g. Haskell [1941], Faust [1951]. Faust's velocity fits of well-controlled shale and sandstone sections at various depths are plotted in the figure for comparison. The velocity function is represented by  $Az^{1/6}$ , where  $z$  is depth and  $A$  depends on geologic age. Faust's constants, modified to yield velocities in km/sec for depth in meters, are  $A$  (Pennsylvanian)  $\approx 1.1$ ,  $A$  (Mesozoic)  $\approx 1.0$ ,  $A$  (Eocene)  $\approx .9$  and  $A$  (Post-Eocene)  $\approx .8$ .

#### 2.4 Golden Seismograms

The Pocatello Valley earthquake sequence included a  $M_L = 4.2$  foreshock, a 6.0 mainshock, one 4.7 and two 3.8 aftershocks and over 50 lesser events greater than 3.0, Arabasz et al. [1981]. Long and short period WSSN seismograms of the events were obtained from the Golden seismographic station, operated by the Colorado School of Mines, Majors [1980], Glover [1980]. These are the closest available records within the Denver Basin, and were recorded on bedrock at the

base of the Rocky Mountains. Because WG5 and GOL are only 150 km apart, with no significant difference in tectonic province, the GOL seismograms were judged adequate to infer bedrock motion near WG5.

Epicentral distance to GOL is about 650 km and the azimuth is  $67^\circ$  east of south. The main shock at  $2^{\text{h}}31^{\text{m}}6^{\text{s}}$  UTC, March 28 drove the long and short period instruments off-scale for 4 to 5 minutes; however, the lesser events provided good records. The short period east-west seismogram of the first 3.8 magnitude aftershock is shown in Fig. 2-2. The sequence, relative amplitude and timing of arrivals is common to the 4.2 foreshock and the 4.7 aftershock as well.

The first arrival, at  $1^{\text{m}}30^{\text{s}}$  after the origin time of  $16^{\text{h}}15^{\text{m}}6^{\text{s}}$  March 28, is the  $P_n$  phase. This is a low amplitude refracted wave associated with the crust-mantle transition or Moho. Following  $P_n$  is a higher amplitude  $P_g$  phase, a direct wave propagated through the granite crust. Another arrival,  $P^*$ , associated with deeper layers in the crust is present between  $P_n$  and  $P_g$ . The next obvious arrival is  $S_g$ , the direct shear wave. Faster refracted phases (e.g.  $S_n$ ) precede this arrival but are not obvious on the record. Love waves including  $L_g$  follow  $S_g$  but no distinctions can be made and similarly for Rayleigh waves. The corresponding long period seismogram shows no evidence of this event.

The only significant long period record at GOL besides the mainshock is the magnitude 4.7 aftershock shown in Fig. 1-5. Origin time is  $13^{\text{h}}1^{\text{m}}20^{\text{s}}$ , March 29. The long period arrival at  $13^{\text{h}}5^{\text{m}}$  begins with a period near 12 seconds and is down to 5 seconds after  $1^{\text{m}}30^{\text{s}}$ . The vertical and east-west components have the higher amplitude. This behavior, the normal dispersion and particle motion, identifies the phase as a Rayleigh wave. Group velocity of the 12 second period is about 2.85 km/sec, which is within the expected scatter for fundamental mode continental Rayleigh waves, Oliver [1962]. As expected, the smaller shocks do not excite surface waves very effectively; however, the 4.7 aftershock is seen to be a marginally effective source and the mainshock is a very rich source.



## 2.5 Observed and Theoretical Dispersion Data

The dispersed train of Rayleigh waves observed from the magnitude 4.7 after-shock is used here to deduce dispersion (group velocity vs. period) and particle motion (ellipticity) data. These data are compared to theoretical calculations for each of the crustal models described above, assuming a range of sediment thicknesses.

Direct measurements of predominant period and time of arrival off Fig. 1-5 yield group velocity versus period, plotted in Fig. 2-3. To compare this travel path dispersion with continental and sedimentary dispersion curves observed elsewhere in the world, the scatter band given by Oliver [1962] is indicated. Clearly, despite structural complexity on the travel path, no gross aberrations are observed for dispersed periods greater than 5 seconds.

Particle motion orbits, i.e. east-west versus vertical motion, were also measured. These are shown in Fig. 2-3 after correcting for azimuth to give radial versus vertical motion. Approximate ellipticities are .41 near 6 seconds and .69 near 9 seconds. Note that in comparison to the vertical seismogram in Fig. 1-5, the east-west amplitude is seen to smoothly decrease with time and predominant period. Actually, the smooth decrease is due to long period WWSSN instrument response, for which gain drops linearly from 3000 to 2000 as period decreases from 9 to 5 seconds. Therefore, observed east-west (or radial) motion is nearly uniform over the period range while vertical motion fluctuates principally as a function of ellipticity.

The period window of interest here is 1 to 5 seconds. Using the observed dispersion data available for periods greater than 5 seconds as a control, dispersion calculations in the crustal models topped by sedimentary sections were extended into the shorter period range. For example, assuming sedimentary layers of Paleozoic shales and sandstones, Fig. 2-1, over the Flaming Gorge crustal

model yields the fundamental mode Rayleigh wave dispersion curves in Fig. 1-6b. A 2 km layer gives the best fit to data, but of course optimum depth depends on sediment velocity which was chosen here only to provide an upper bound. Velocities could be as much as 25% lower in post-Eocene sediments, as indicated in Fig. 2-1. Nonetheless, these calculated dispersion curves show that sedimentary cover shifts the dispersion curve to the right and introduces a pronounced group velocity minimum in the period range of interest.

The dispersion calculations were made assuming a ratio of P to S seismic velocities of 2 in the sediment and 1.73 in the crust, corresponding to commonly assumed Poisson ratios of  $1/3$  and  $1/4$ , respectively. The sedimentary ratio is suggested by laboratory measurements in shales from the Williston Basin, Tosaya [1981] and the crustal ratio is consistent with rock data, Press [1966] and surface wave velocity inversion results of Keller, et al. [1976]. Densities are found from data in Gardner, et al. [1974] for sedimentary rock and the Nafe and Drake empirical curves in Press [1966]; although gravity modeling data in the Green River Basin, Smithson, et al. [1979] indicates 5-10% lower densities in basement rock. The computer code used for the dispersion calculations assumed a piecewise constant layered halfspace, Herrmann [1978] with 20-30 layers to adequately resolve the velocity models.

A comparison of fundamental and first higher mode Rayleigh wave dispersion is shown in Fig. 2-4 for the Flaming Gorge and Sinclair models covered by a 3 km Paleozoic layer. Group velocity minima for the fundamental are near 3.5 seconds in both models, and near 4.3 seconds for the first overtone. The presence of these minima in the period range corresponding to Wing V suspension system resonances is very suggestive. Group velocity minima yield the Airy phase--associated with long duration ringing due to late arrivals propagating near the minimum group velocity. Such long duration ringing near critical periods of a

surface structure may excite significant response even if the amplitude of ground shaking is relatively low.

The above results are for an average Moho depth of 40 km. Because depth increases to 48 km across the Shear Zone, about 25-30% of the travel path is through this thicker crust. Dispersion curves for the Wolcott model are therefore shown in Fig. 2-5 for no sediment, corresponding to the Golden seismograph location, and about 2.5 km of sediment suggestive of Denver Basin fill west of Golden and similar to that under Wing V. These show similar group velocity minima, implying that the change in crustal thickness does not radically alter the dispersion. A favorable comparison of observed and theoretical ellipticity is also shown in the figure for 9 second waves. The calculated ellipticity is nearly constant ( $\approx 0.73$ ) for periods from 2 to 12 seconds so the observed ellipticity at 6 seconds shown in Fig. 2-3 does not compare as well.

#### 2.6 Response of Denver Basin Sediments to Love and Rayleigh Waves

In order to convert estimates of bedrock motion to response at the surface of deeper sediments, surface wave response ratios were calculated for two sites in the Denver Basin. The responses at Flights H and P (1800 m, 3400 m depth of sediment, respectively, over the Wolcott model) of Wing V were normalized by surface wave response in the Wolcott model. This allows us to investigate the periods which are most strongly amplified by the sediments in the Denver Basin. Flights H and P are chosen because they bound the sediment depths for all of Wing V.

We assume that the surface wave energy flux is the same on a path from the Rocky Mountains to the Denver Basin and we scale the mode shapes obtained from dispersion calculations on the basis of normalized total energy. If  $I_0$  is the normalized energy in the surface wave mode and  $U_g$  is its group velocity, then

the ratio of surface displacements at two different locations ( $U_2/U_1$ ) is given by

$$U_2/U_1 = \left( \frac{(I_o U_g)_1}{(I_o U_g)_2} \right)^{1/2}$$

The assumption of uniform energy flux neglects scattering into body waves and other surface wave modes, which can be included only by resorting to numerical methods. Nonetheless, the present results are qualitatively correct for the cases considered.

Figures 2-6a and b show results for radial and vertical components of Rayleigh waves, respectively. Nominal amplification is on the order of 3 relative to bedrock response. Peak amplification is about 4 and it occurs at a period of about 2.7 sec for Flight H (shallow sediment) and at about 4.4 sec for Flight P (deeper sediment). In Fig. 2-7, a nominal amplification of 4 is shown for the Love wave case. Peak amplification is about 5.3 and occurs at a period of about 4.4 sec. The significant findings are: For Rayleigh waves the amplification peaks occur within the period window of interest (1-5 sec) and, in fact, bracket the critical period of 3.5 sec, Wojcik et al. [1980], with a relative ratio of peak to nominal amplitude of about 1.33; and for Love waves the peaks occur near the upper end of the period window with a peak to nominal ratio near 1.25. In both cases, the peak relative amplification decreases, and its period increases as the sediment depth is increased from the 2 km to 3 km sites. The fact that peak amplification in the Rayleigh wave case brackets the critical period (3.5 sec) and in the Love wave case occurs at longer period suggests that Rayleigh waves are more likely to produce patterns of response anomalies than are Love waves.

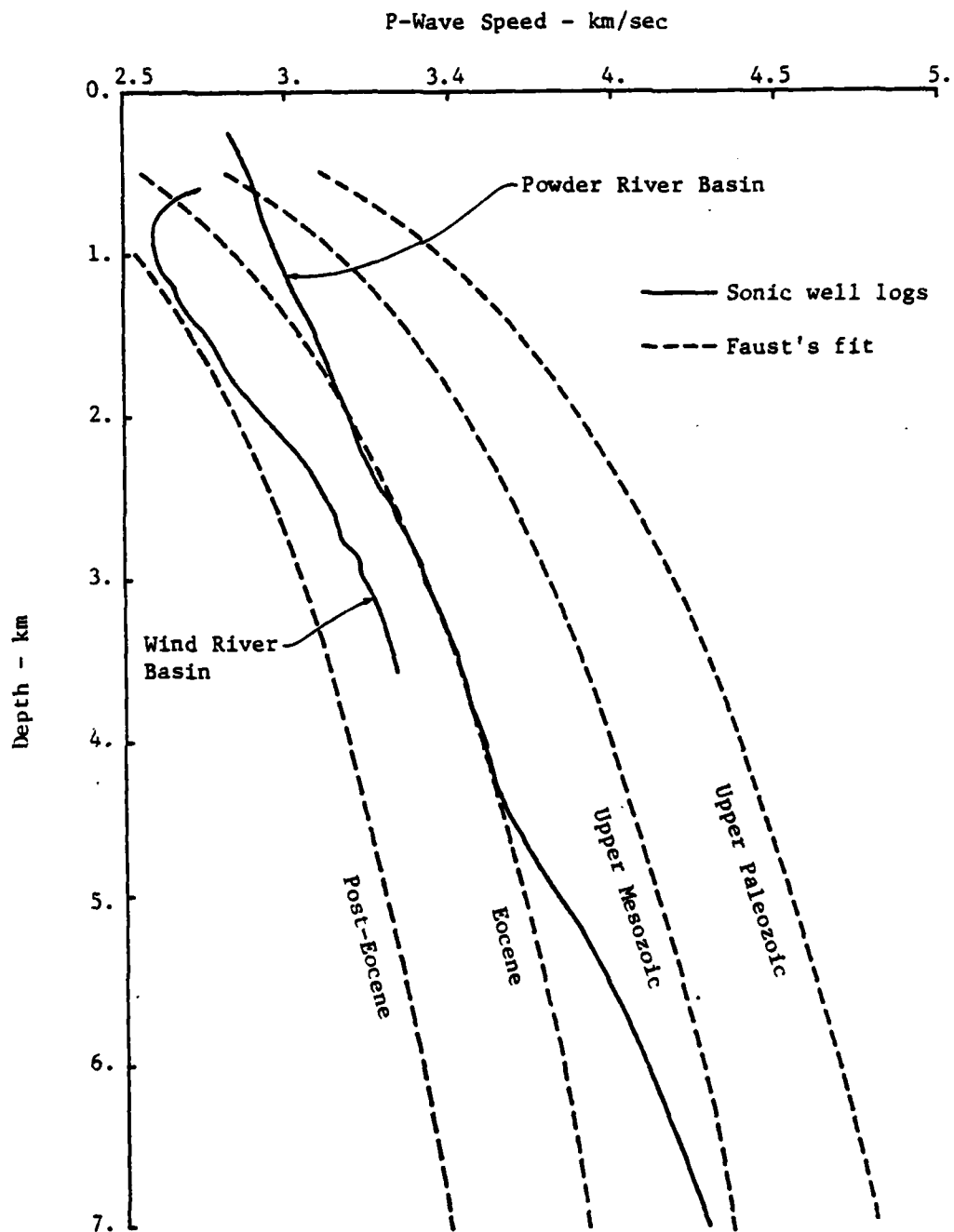


Figure 2-1. Sonic log data from nearby Wind River and Powder River Basin sediments compared to Faust's fit for shale/sandstone sections.

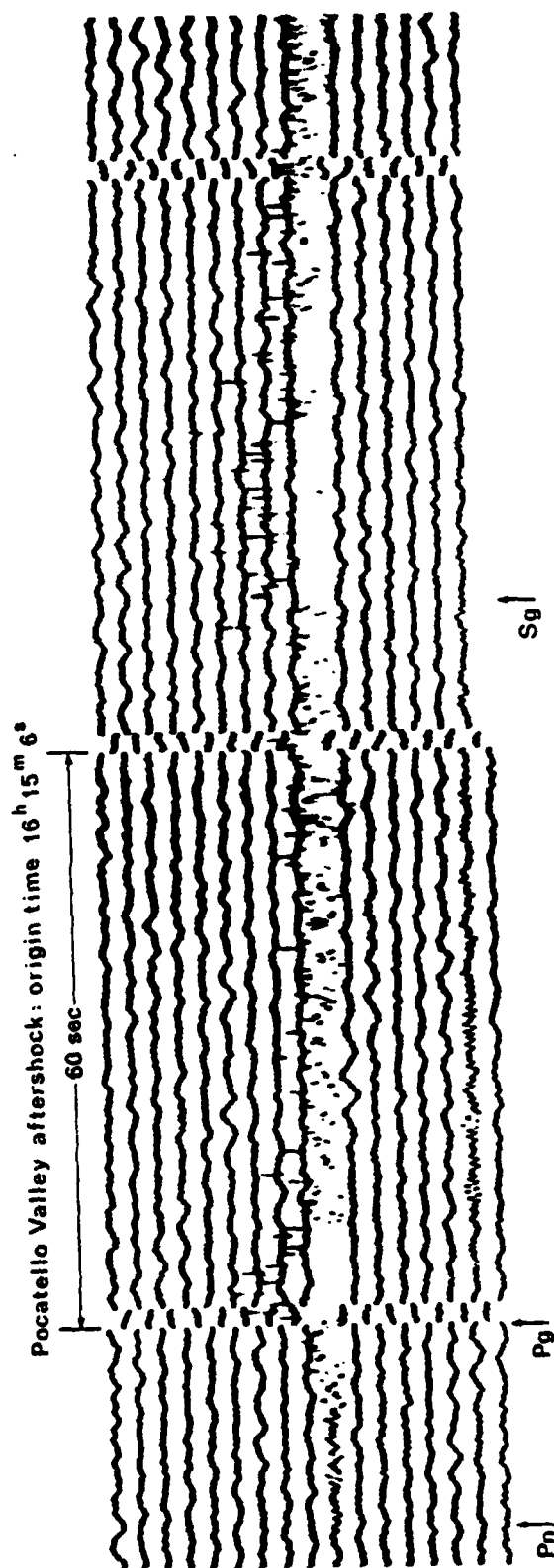


Figure 2-2. Short period E-W WSSN seismogram of a  $M_L = 3.8$  March 28, 1975 Pocatello Valley aftershock recorded at Golden, Colorado. First minute mark on event trace is 16<sup>h</sup> 17<sup>m</sup>.

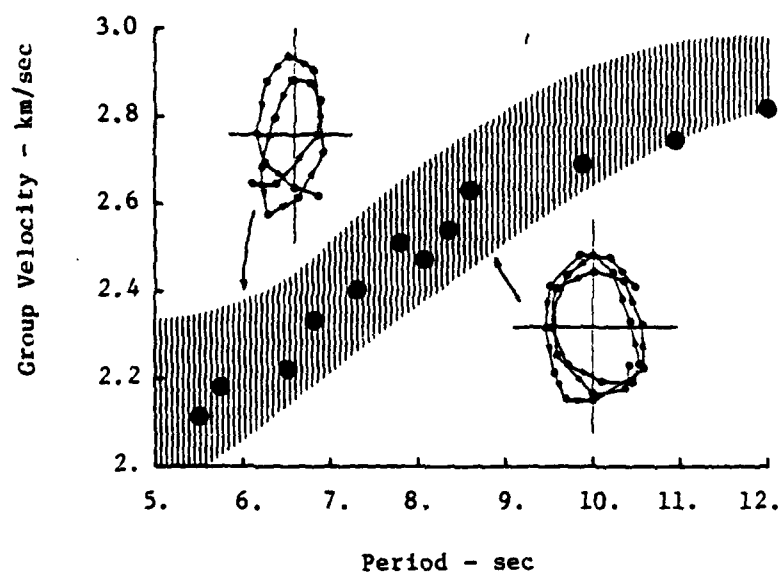


Figure 2-3. Observed fundamental mode Rayleigh wave group velocity and ellipticity at Golden, Colorado.

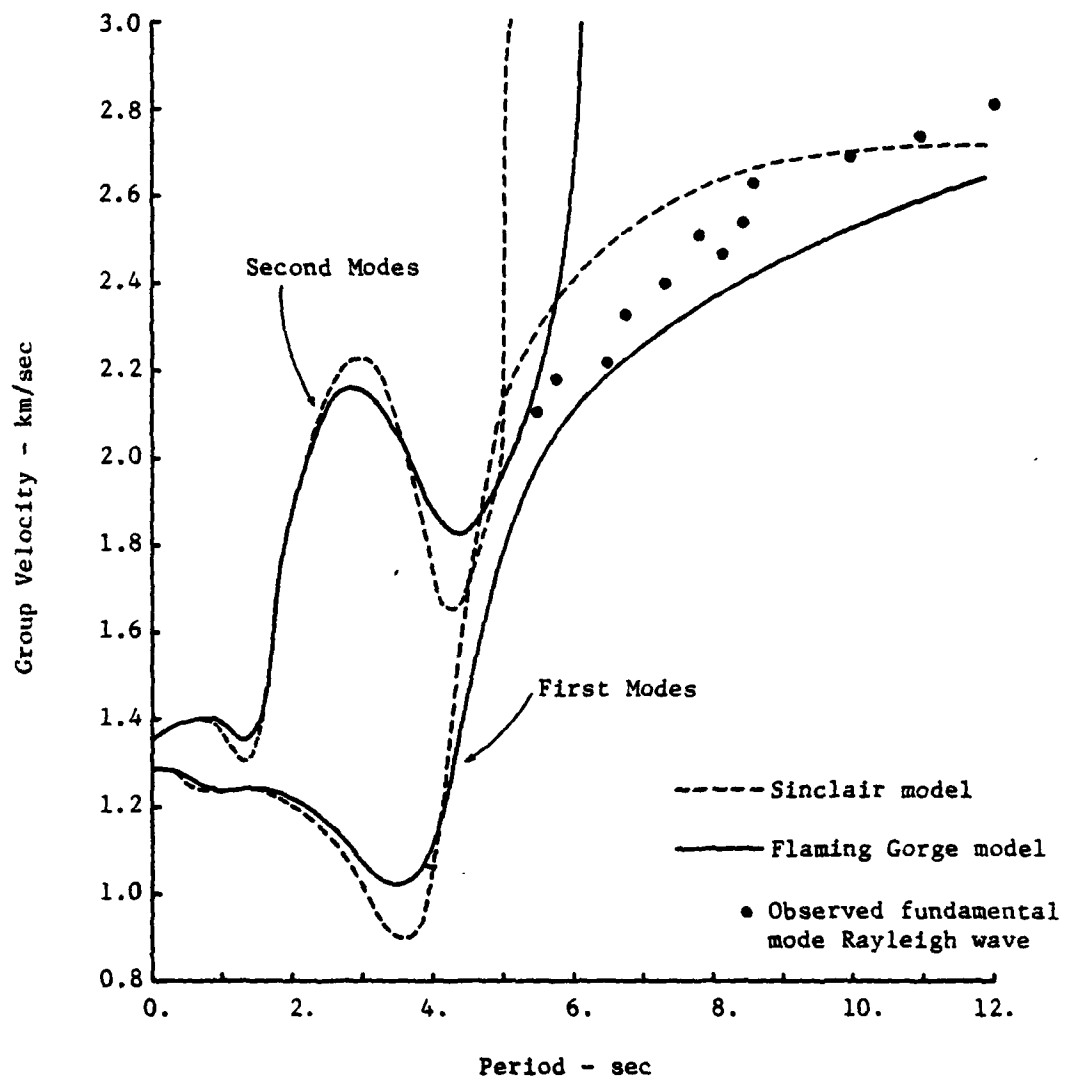


Figure 2-4. A comparison of Rayleigh wave dispersion for Sinclair and Flaming Gorge models with 3 km of sediment.



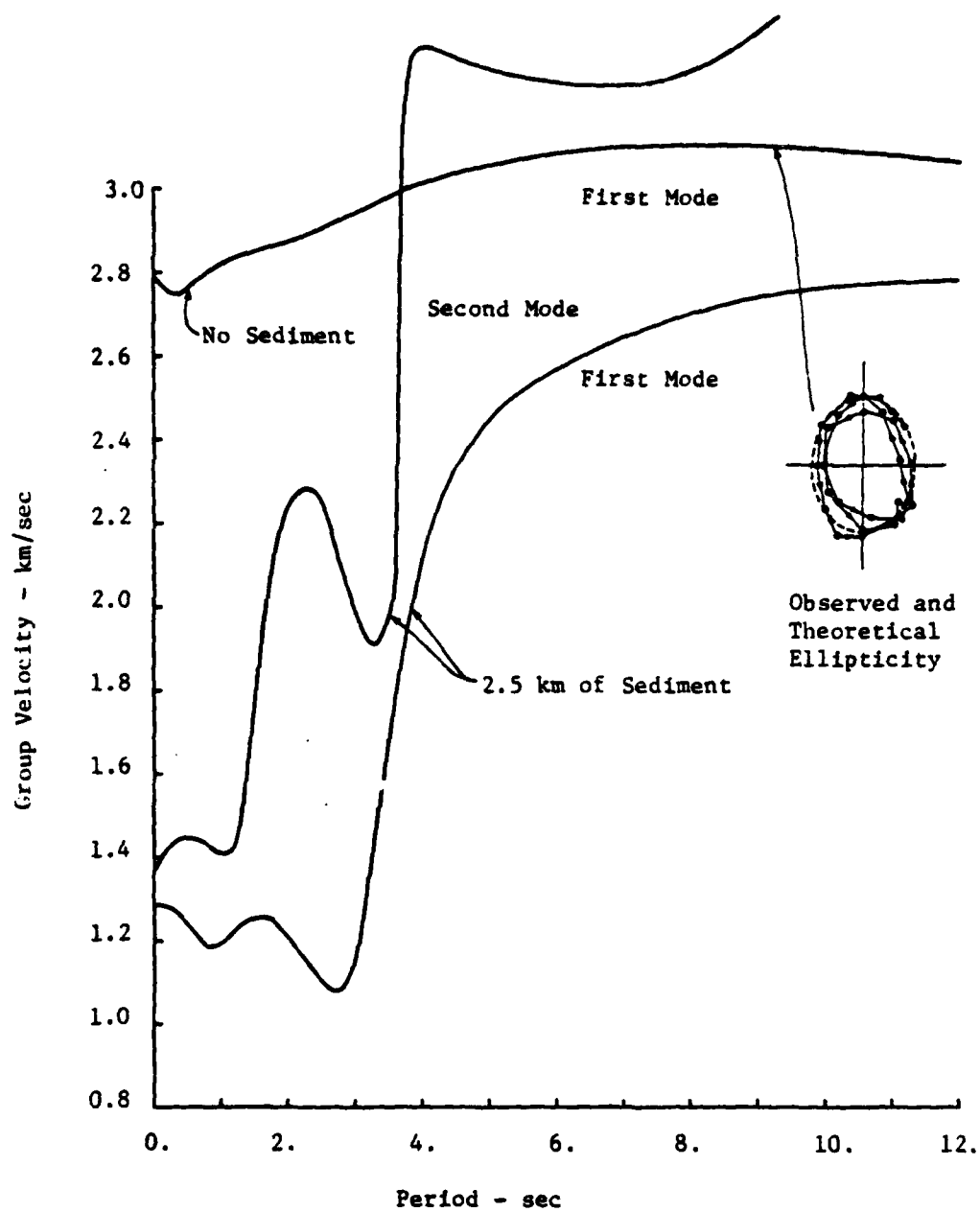


Figure 2-5. Dispersion curves for Wolcott model.

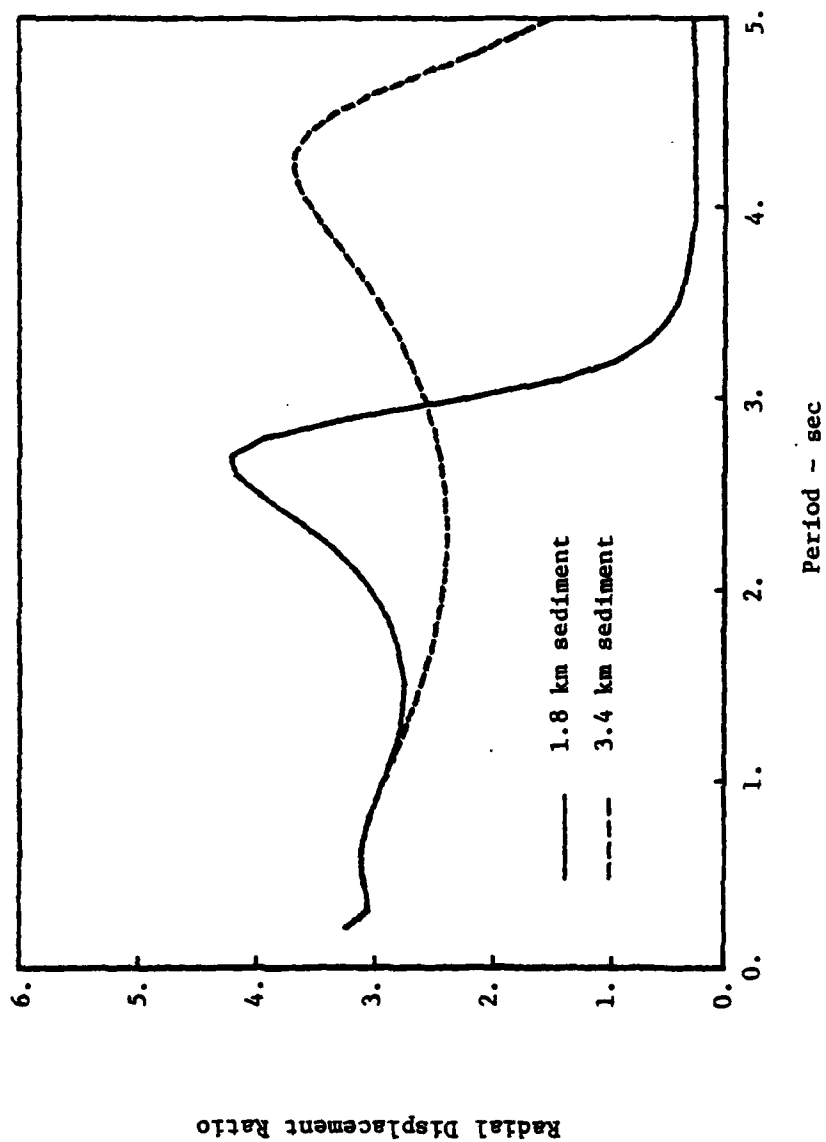


Figure 2-6a. Radial displacement ratios for fundamental mode Rayleigh waves.

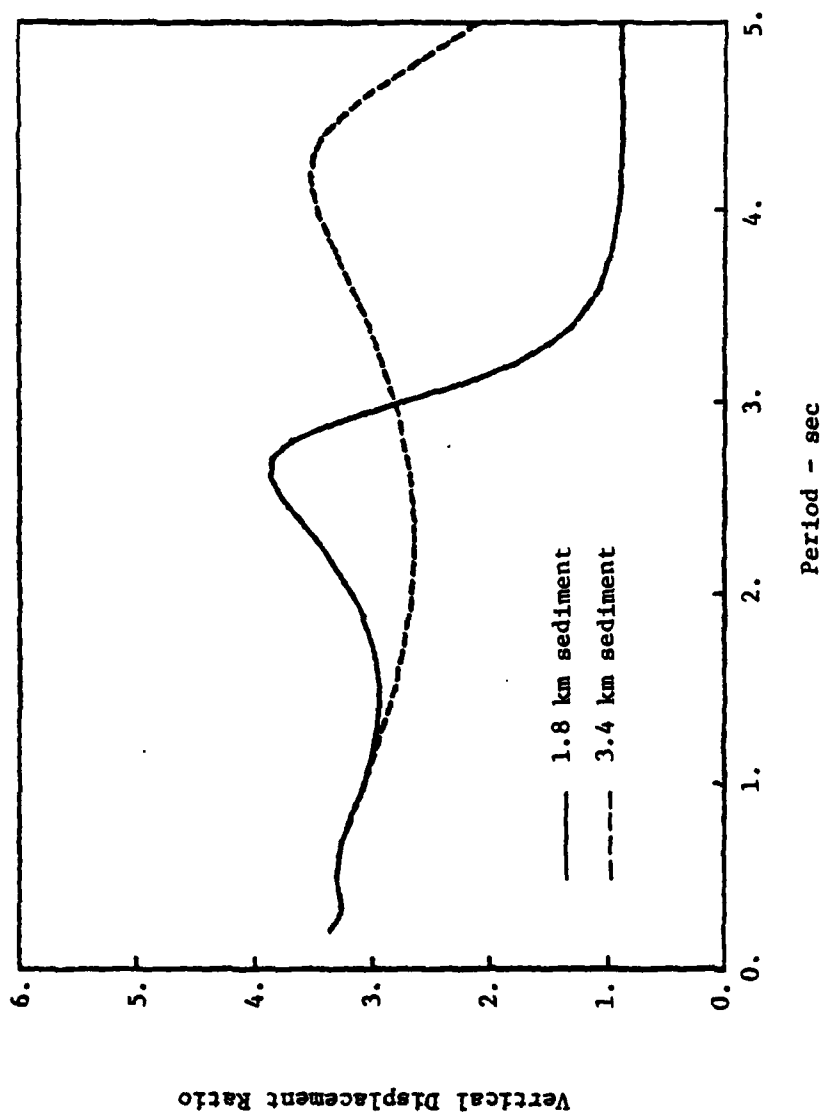


Figure 2-6b. Vertical displacement ratios for fundamental mode Rayleigh waves (see text for explanation).

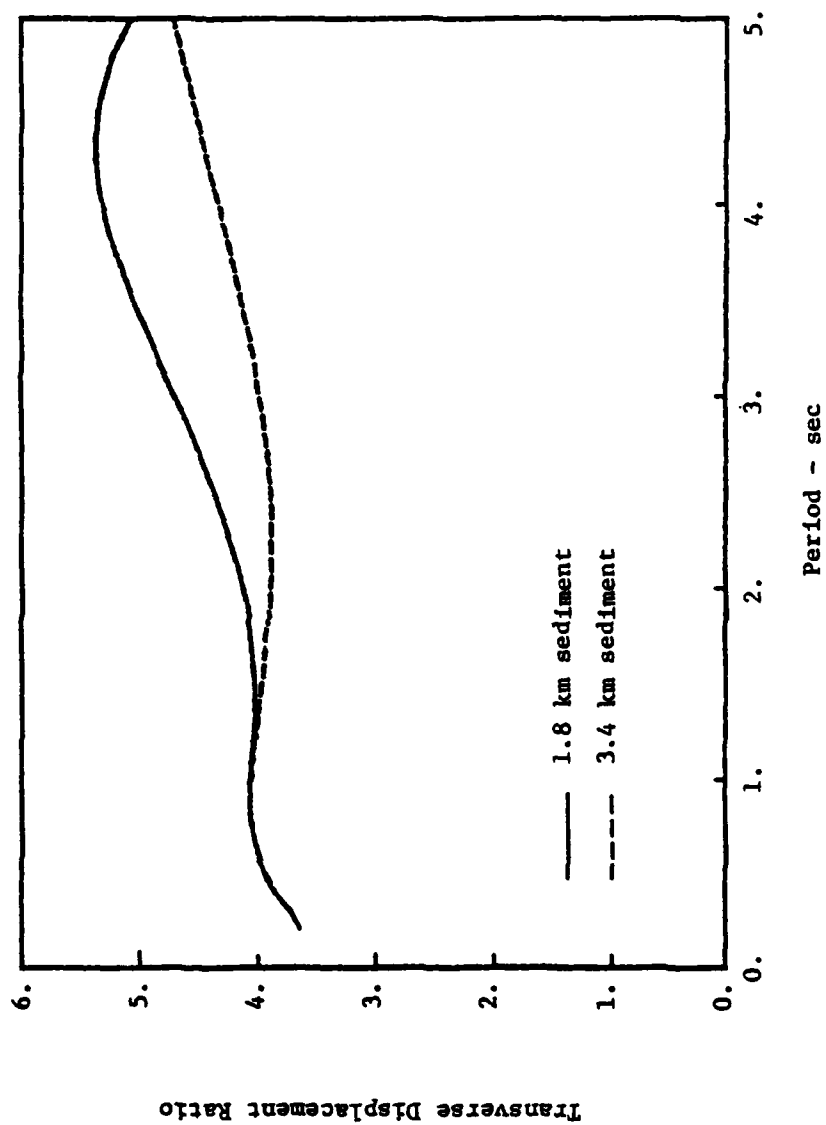


Figure 2-7. Displacement ratios for fundamental mode Love waves (see text for explanation).

### SECTION 3

#### SURFACE WAVES: A SEISMIC RAY THEORY PERSPECTIVE

Shorter period surface waves with periods of 1 to 5 seconds are expected to interact significantly with the laterally inhomogeneous near-surface structure on travel paths crossing the Green River Basin and the Central Rockies described above. The question is: How, and to what degree, are these surface waves filtered or otherwise modified by the travel path before reaching the Denver Basin? To investigate this question, it is necessary to first recognize that there are two distinct types of surface waves to be considered. First is the fundamental mode Rayleigh wave which depends only on the presence of a free surface for its existence, decays exponentially with depth and is composed of constructively interfering evanescent P- and SV- waves. Second are the Rayleigh overtones as well as the fundamental Love mode and its overtones, which are all channeled waves composed in part or fully of trapped plane waves, typically in a layer from the free surface to some depth of maximum wave penetration.

In an effort to explore the question of surface wave interaction with basin and mountain structure, this section examines their effects on channeled surface waves in the context of seismic ray theory. This is a useful perspective because rays are easily continued through inhomogeneities, while evanescent modal solutions are not. It is helpful to consider first the fundamental mathematical analysis of the governing wave equations in a halfspace with seismic velocities varying smoothly in the vertical direction only. This analysis is based on the theory of partial differential equations of mixed type (hyperbolic-elliptic) and relies on the method of characteristics for the hyperbolic solution.

### 3.1 Mixed (Hyperbolic-Elliptic) Wave Fields Composing Surface Waves

Consider time harmonic trains of Love and Rayleigh surface waves propagating over an elastic halfspace in the positive  $x$  direction with phase velocity,  $V$ , Fig. 3-1. The halfspace is a one-dimensional medium in that wave speeds are a function of depth only,  $\alpha(z)$  for P-waves and  $\beta(z)$  for SV and SH waves. Particle motion for Love waves is antiplane--in the  $y$  direction, while for Rayleigh waves motion is inplane--in the  $x$  and  $z$  directions. Normalized displacements on the free surface may be written as

$$\text{Love waves: } v_0(x,t) = \cos \omega(t-x/V) \quad (3-1)$$

$$\text{Rayleigh waves: } \begin{cases} u_0(x,t) = e_0 \cos \omega(t-x/V) \\ w_0(x,t) = \sin \omega(t-x/V) \end{cases} \quad (3-2)$$

where  $u_0$ ,  $v_0$  and  $w_0$  are  $x$ ,  $y$  and  $z$  surface displacements, respectively,  $\omega$  is circular frequency and  $e_0$  is surface ellipticity (ratio of horizontal to vertical amplitude).

The governing wave equations describing any two-dimensional motion of the halfspace are

$$\text{Antiplane: } \nabla^2 v = \frac{\partial^2 v}{\partial z^2} + \frac{\partial^2 v}{\partial x^2} = \frac{1}{\beta^2(z)} \frac{\partial^2 v}{\partial t^2} \quad (3-3)$$

$$\text{Inplane: } \nabla^2 \phi = \frac{1}{\alpha^2(z)} \frac{\partial^2 \phi}{\partial t^2} \quad (3-4)$$

$$\nabla^2 \psi = \frac{1}{\beta^2(z)} \frac{\partial^2 \psi}{\partial t^2}$$

where  $\phi$  and  $\psi$  are the Lamé displacement potentials for which  $u = \frac{\partial \phi}{\partial x} - \frac{\partial \psi}{\partial z}$  and  $w = \frac{\partial \phi}{\partial z} + \frac{\partial \psi}{\partial x}$ . In order to solve for the surface wave field in the halfspace, it is necessary to reduce the number of independent variables in these partial differential equations (PDE's). The usual approach is to express them as a number of ordinary differential equations, via separation of variables or

integral transforms. A useful alternative, however, is to attack the wave equations directly by means of wavefront and ray analysis, described next.

Surface waves in Fig. 3-1 are clearly stationary in a coordinate system convected with phase velocity,  $V$ , along the  $x$  axis. Accordingly, if  $t$  and  $x$  are replaced through the transformation,  $\tau = t - px$  where  $p \equiv 1/V$ , then for the Love wave case, the governing equation, (3-3) becomes

$$\frac{\partial^2 v}{\partial z^2} = q_\beta^2(z) \frac{\partial^2 v}{\partial \tau^2} \quad ; \quad q_\beta^2 = 1/\beta^2(z) - p^2 \quad (3-5)$$

which is a PDE in only two independent variables. From the general theory of second-order partial differential equations, Sommerfeld [1964], this may be characterized by type as hyperbolic, parabolic or elliptic, depending on the sign of the coefficient  $q_\beta^2(z)$ . The coefficient changes sign at depth, hence the PDE is of mixed type--hyperbolic when  $q_\beta^2 > 0$ , elliptic when  $q_\beta^2 < 0$  and parabolically degenerate when  $q_\beta^2 = 0$ . Therefore, for a monotonically increasing velocity function the displacement field in the halfspace is divided into two domains: hyperbolic in a layer above the so-called elliptic horizon at depth  $z_m$ , where  $\beta(z_m) = V$  and  $q_\beta^2(z_m) = 0$ ; and elliptic below this depth. When low velocity zones exist, there may be more than one elliptic horizon defining hyperbolic channels, for example.

In the convected wave equation (3-5) the constant,  $p = 1/V$  is the horizontal slowness and is commonly referred to as the ray parameter. The coefficient,  $q_\beta(z)$  is the vertical slowness and is imaginary below the elliptic horizon. This follows because, in the definition of  $q_\beta^2$  (see (3-5)), the  $1/\beta^2(z)$  term represents the relative contribution of inertial forces (recall it was the coefficient of acceleration in the wave equation (3-3)), while the  $p^2 = 1/V^2$  term is the relative contribution of elastic restoring forces. Inertial forces dominate elastic forces when  $q_\beta^2 > 0$  (hyperbolic), and conversely for elastic

forces when  $q_\beta^2 < 0$  (elliptic). Therefore, only inertial wave fields (homogeneous waves) exist in the hyperbolic domain but not in the elliptic, where steadily moving elastic equilibrium fields (inhomogeneous or evanescent waves) result, decaying exponentially with depth.

For the case of Rayleigh waves, the wave equations (3-4) in convected coordinates are

$$\begin{aligned} \frac{\partial^2 \phi}{\partial z^2} &= q_\alpha^2(z) \frac{\partial^2 \phi}{\partial \tau^2} \quad ; \quad q_\alpha^2 = 1/\alpha^2(z) - p^2 \\ \frac{\partial^2 \psi}{\partial z^2} &= q_\beta^2(z) \frac{\partial^2 \psi}{\partial \tau^2} \end{aligned} \quad (3-6)$$

Assuming that both  $\alpha(z)$  and  $\beta(z)$  increase with depth, the wave fields can be divided into hyperbolic and elliptic domains as before. Clearly, both potentials have their elliptic horizons on the free surface when  $V < \beta(0)$ , corresponding to fundamental mode (or free surface) Rayleigh waves (coupled inhomogeneous or evanescent wavefields). When  $\beta(0) < V < \alpha(0)$  the  $\psi$  potential has its elliptic horizon at depth, while the  $\phi$  horizon is on the surface; and when  $V > \alpha(0)$  both  $\phi$  and  $\psi$  have their horizons at depth. These latter cases correspond to higher mode (or channeled) Rayleigh waves because at least one hyperbolic layer or channel exists, admitting inertial or homogeneous surface waves.

### 3.2 Hyperbolic Wave Fields and Rays

The hyperbolic wave fields follow from the convected wave equations (3-5,6) using the method of characteristics. Recognizing that in the hyperbolic domains (3-5,6) are one-dimensional wave equations in the  $z$  direction with variable slowness or velocity, the characteristic equation is simply  $\frac{d\tau}{dz} = \pm q(z)$  (where  $q$  means  $q_\alpha$  or  $q_\beta$ ). Integrating from the free surface gives

$$\tau(z) = \pm \int_0^z q(\zeta) d\zeta + \tau_{0\pm} \quad (3-7)$$



where  $\tau_{0\pm}$  is the free surface intercept of the characteristic. These characteristic curves yield the wavefronts in the hyperbolic channel as shown in Fig. 3-2. Through each point of the channel, there are two characteristics corresponding to the  $\pm$  signs in (3-7). At the point of reflection on the elliptic horizon the wavefronts are either cusped (zero included angle) in the case of a smooth wave speed function (Fig. 3-2a), or bent (finite angle) if the wave speed is discontinuous at the horizon (Fig. 3-2b).

In applications, the wavefront trajectories or rays are a more convenient means of describing hyperbolic wave fields than are characteristics because rays are invariant with time. They follow from the fact that a wavefront in an isotropic medium is a surface of constant phase moving normal to itself at the local wave speed. Representing this surface by the phase function,  $\Phi(x, z, t) = 0$ , then from the equation of characteristics,

$$\Phi(x, z, t) = \pm \int_0^z q(\zeta) d\zeta + \tau_0 - t = \Psi(x, z) - t \quad (3-8)$$

where

$$\Psi(x, z) = px \pm \int_0^z q(\zeta) d\zeta + \tau_0 \quad (3-9)$$

is the wave function or eiconal. The normal to a wavefront at some fixed time is just  $\nabla\Psi$ , or

$$\underline{n} \equiv \nabla\Psi = p\underline{i} \pm q(z)\underline{k} \quad (3-10)$$

where  $\nabla = \frac{\partial}{\partial x} \underline{i} + \frac{\partial}{\partial z} \underline{k}$  is the gradient operator. This double valued vector is the slowness (or refractive index) and makes an angle  $\pm\theta$  with the positive  $z$  axis given by  $\tan\theta = p/q(z)$  which is Snell's law for a one-dimensional medium. Substituting the definition of  $q(z)$  yields the more familiar

form of Snell's law,

$$\frac{\sin\theta}{c(z)} = p \quad (3-11)$$

where  $c$  is equal to  $\alpha$  or  $\beta$  for  $P$  and  $SV$  or  $SH$  rays, respectively.

Snell's law provides the relation between ray angle and depth, hence the basis for ray tracing in a one-dimensional medium. Referring to Fig. 3-3, along the ray  $\frac{dx}{dz} = \tan\theta$ , hence substituting  $\tan\theta = p/q(z)$  and integrating,

$$x = p \int_0^z \frac{d\zeta}{q(\zeta)} + x_0 \quad (3-12)$$

where  $x_0$  is the starting point on the free surface. Travel time is found from  $\frac{dt}{ds} = 1/c(z)$  with  $ds = dz/\cos\theta$ , whence

$$t = \int_0^z \frac{d\zeta}{c^2(\zeta)q(\zeta)} + t_0 \quad (3-13)$$

and  $t_0$  is starting time. In a hyperbolic channel, the rays corresponding to the wavefronts in Fig. 3-2 are trapped between the free surface and elliptic horizon as shown in Fig. 3-4. The skip distance,  $X$  and travel time,  $T$ , on a ray segment from the free surface to the elliptic horizon and back to the free surface are

$$X = 2p \int_0^{z_m} \frac{d\zeta}{q(\zeta)}, \quad T = 2 \int_0^{z_m} \frac{d\zeta}{c^2(\zeta)q(\zeta)}. \quad (3-14)$$

For a smooth velocity function (Fig. 3-5a), the elliptic horizon is a caustic, which is tantamount to saying it is a boundary between hyperbolic and elliptic wave fields. When a ray is reflected at the horizon (touches the caustic), the amplitude reflection coefficient is unity but there is a phase change of  $\pi/2$ . For a discontinuous velocity function the reflection coefficient and phase change are found from the usual formulas for reflection at interfaces.

### 3.3 Ray Tracing in Smooth Crustal Models

To examine channeled surface waves on travel paths between Pocatello Valley and the Denver Basin, it is necessary to first trace ray paths in the crustal models. This amounts to evaluating the integral in (3-12). The easiest approach is to approximate the crustal models, Fig. 1-4, by piecewise linear velocity segments and use the fact that rays in a linear gradient are simply arcs of circles (Officer [1974], Exercise 6.5). More powerful algorithms for smoother velocity functions are available but not warranted for the purposes of this section. Mantle and crustal P-rays in the Flaming Gorge model with 5 km of Paleozoic sediment are shown in Fig. 1-7a, including reduced travel time curves. For reference, shallow penetrating sedimentary P-rays in the upper crust are shown in Fig. 1-7b for smoothly increasing sediment velocity and for a more realistic sedimentary column corresponding to Wing V in the Denver Basin.

The mantle ray fan in Fig. 1-7a starts at  $19.4^\circ$  from the vertical, with a  $.05^\circ$  ray angle increment, to the final ray at  $20.4^\circ$ . A velocity gradient of  $.005 \text{ km/sec/km}$  is assumed in the upper mantle below the Moho (approximated from Jeffreys [1929]) as indicated in Fig. 1-4. This value is supported approximately by deeper refraction studies near the Rocky Mountains, Julian [1970]. The crustal ray fan in Fig. 1-7a is a continuation of the mantle fan from about  $20^\circ$ , at increments of  $.25^\circ$  to  $24^\circ$ . Whereas the mantle rays yield refraction like arrivals (pseudo head waves) and a nearly linear reduced travel time curve (by virtue of the assumed linear mantle gradient), the crustal rays show much more variety in terms of penetration depth and travel times. The crustal reduced travel time curve shows a triplication from about 150 km to 300 km, consistent with the reduced USGS refraction data, Prodehl [1979], from which the crustal velocity model was originally derived. Minor triplication, for example at 75 km, is due to the rapid velocity increase in the upper crust.

With travel time curves available, two-point ray tracing allows an identification of arriving phases in the Denver Basin and a correlation with depth of ray penetration. Consider rays connecting the Pocatello Valley source and Golden, Colorado, an epicentral distance of  $\Delta = 650$  km. Referring to travel time curve edc in Fig. 1-7a, there is one direct or single skip mantle ray and a series of multiple skip mantle rays. Skip distances are  $X_m = \Delta/m$  where  $m$  is the integral number of skips,  $m = 1, 2, \dots, M$  with an upper bound of  $M = 4$  corresponding to  $X_4 = 162.5$  km. From the mantle travel time curve, the direct ray arrives at 90 sec and the last multiple at 116 sec. Respective depths of penetration are 60 to 40+ km. Next, from the crustal travel time curve cb, there is no direct crustal arrival but three multiple-skip crustal rays are present with skip distance,  $X_m = \Delta/m$ ,  $m = 2, 3, 4$ . Note that the  $m = 2$  case corresponding to  $X_2 = 325$  km does exist although not indicated in the fan of Fig. 1-7a. The range of calculated arrival times are 105 to 116 seconds and the depths are 40 to 32 km. Finally, from the travel time curve ba, there are an unlimited number of crustal skips for  $m = 2, 3, \dots$  starting from 116 seconds and penetrating to depths from 32 km up to the free surface. For example, the 13th skip ( $X_{13} = 50$  km) arrives at 145 seconds and penetrates to 10 km.

Referring to the Pocatello Valley aftershock recorded at Golden, Fig. 2-2 shows the correlation of early arriving body wave phases and segments of the travel time curves in Fig. 1-7. In particular,  $P_n$  corresponds to direct and multiple mantle P-rays on curve edc;  $P^*$  to multiple deeper crust P-rays on curve bc; and  $P_g$  to multiple shallower crust P-rays on curve ba. In fact, the phase identifiers on the seismogram were placed according to the above calculated arrival time ( $P_n: 90^s$ ,  $P^*: 105^s$ ,  $P_g: 116^s$ ). In contrast to the usual description of  $P^*$  and  $P_g$  as direct waves, according to this interpretation

they are actually skipping rays--with at least one intermediate reflection off the free surface for an epicentral distance of 650 km. Clearly, the same arguments can be applied to travel time curves for S-rays. This is somewhat more to the point because S-rays are the principal constituent of higher-mode surface waves. Unfortunately, this is beyond the scope of the present investigation.

Instead of examining S-rays, attention is directed to dispersion curves in Fig. 3-5 showing phase velocity versus period for higher-mode Rayleigh waves in the Flaming Gorge crust with 0, 3 and 5 km of overlying sediment. For 5 km of sediment in the period range 1 to 5 seconds,  $1.63 \text{ km/sec} \leq V \leq 2.71 \text{ km/sec}$ . Therefore, the elliptic horizon for S-waves is  $3 \text{ km} \leq 3 \text{ m} \leq 6 \text{ km}$ . Therefore, SV-rays composing this surface wave do not penetrate deeper than 6 km. If, instead, we assume 3 km of overlying sediments we find the elliptic horizon for S-waves is  $2.5 \text{ km} \leq 3 \text{ m} \leq 9 \text{ km}$ . If we assume no sedimentary cover, the elliptic horizon for S-waves is  $3.5 \text{ km} \leq 3 \text{ m} \leq 21.5 \text{ km}$ . For 3 km of sediment, the elliptic horizon for the second Rayleigh wave overtone in the period range 1 to 5 seconds is  $3 \text{ km} \leq 3 \text{ m} \leq 27 \text{ km}$ .

Specializing these results to periods of 3.5 seconds, which are of particular interest to Wing V, we find that the elliptic horizon is within the sedimentary layer for both 3 km and 5 km sedimentary depths. However, with no sedimentary cover, rays penetrate to 13 km.

From this we conclude that higher model Rayleigh waves at periods of interest to Wing V will interact with the dipping bedrock interface along the travel path from Pocatello Valley. In the next section, we will apply ray theory to study this interaction in order to identify the modes and periods which can be propagated along the travel path to Wing V.

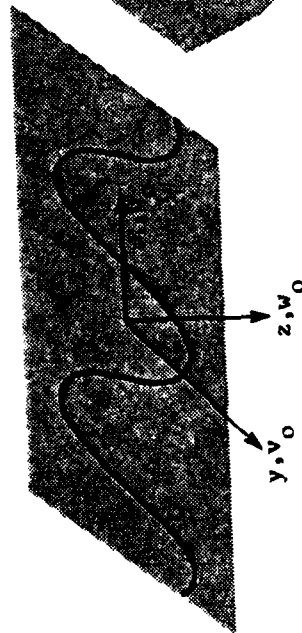
### 3.4 Equivalent Ray Beams and the Hyperbolic Solutions

The above results show that surface waves are composed of hyperbolic and elliptic wave fields. The former can be described by simple rays while the latter require diffracted rays, Keller and Karal [1964], and are beyond the scope of the present work. Hyperbolic wave fields include SH-rays for all Love waves; SV-rays for Rayleigh waves when  $V < \alpha(0)$ ; and both P- and SV-rays for Rayleigh waves when  $V > \alpha(0)$ . Elliptic wave fields, which include the free surface Rayleigh wave case and evanescent P-wave case when  $V < \alpha(0)$ , cannot be described by conventional rays. They can be treated by numerical methods, which is the subject of a current study by the present authors. It follows that the present study by conventional ray methods consider only a portion of the surface wave field which can occur, namely, that portion governed by hyperbolic equations.

A convenient view of the surface wave ray system in a waveguide is illustrated in Fig. 3-6. Here a source of monomode surface waves approaches from the left and is refracted from depths appropriate to the variation of wave speed with depth. At intervals,  $X$ , called the skip distance, the rays encounter the free surface and are reflected downward where the process is repeated. However, when the rays encounter, instead of the free surface, a block of material with the same wave speeds as the surface layer, they are refracted along straight rays as Fig. 3-6 shows. By reciprocity, we can inject ray beams from the block into the halfspace where they will propagate as surface waves, provided the frequency and ray inclination satisfy the dispersion relation. Figure 3-7 shows an example of how this view of surface waves can be used to determine the effect of a lateral inhomogeneity--in this case a dipping layer corresponding to an idealization of the western flank of the Rocky Mountains on the path between Pocatello Valley to Golden, Colorado, shown in Fig. 1-3b. This case will be treated quantitatively in Section 4.

This view of surface waves can be used to understand qualitatively their interaction with typical graben structures of Basin and Range valleys as well.

a. Love wave



b. Rayleigh wave

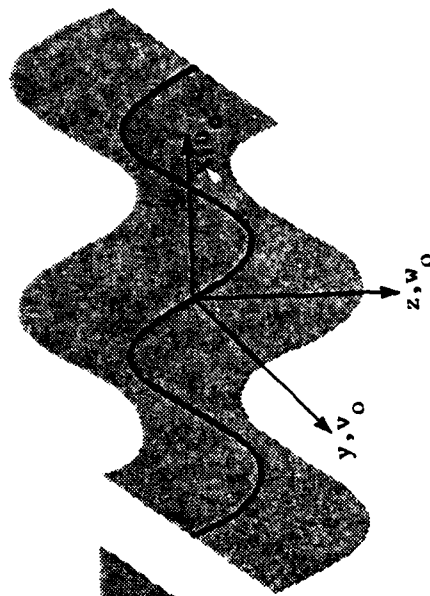
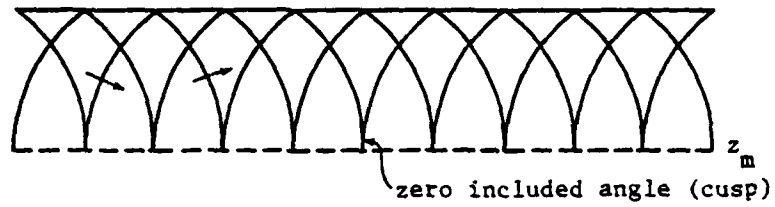


Figure 3-1. Components of surface wave motion.



a. Smooth velocity change at  $z_m$



b. Discontinuous velocity change at  $z_m$

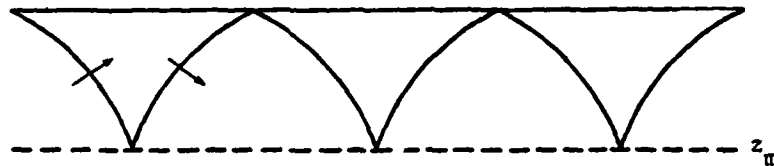


Figure 3-2. Wavefronts in the hyperbolic channel.

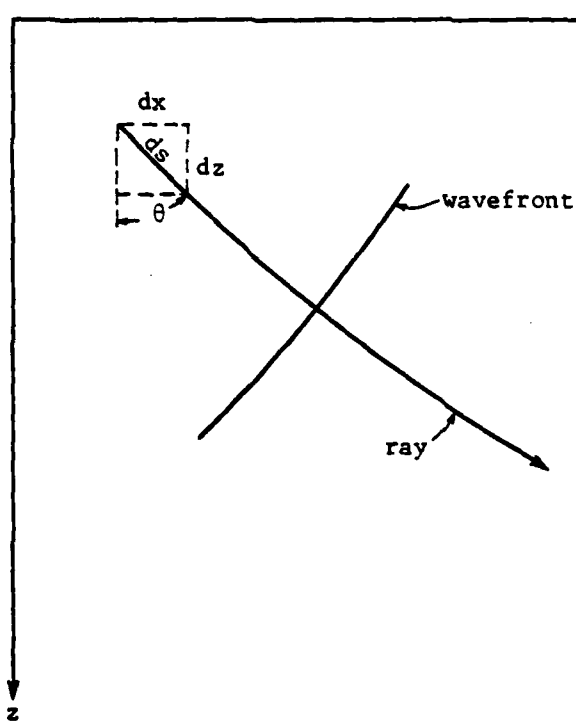
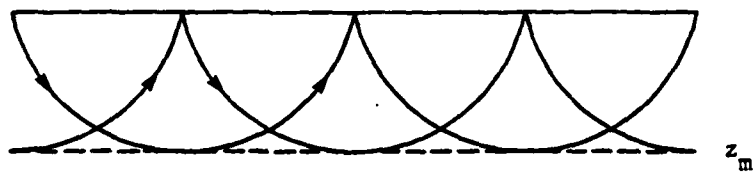


Figure 3-3. Ray geometry.

a. Smooth velocity change at  $z_m$



b. Discontinuous velocity change at  $z_m$

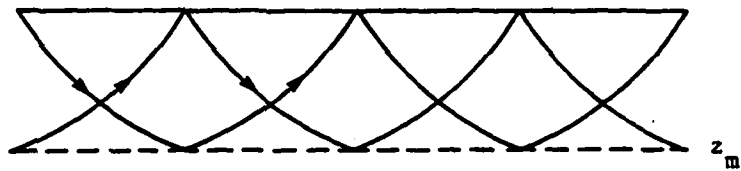


Figure 3-4. Rays in the hyperbolic channel.

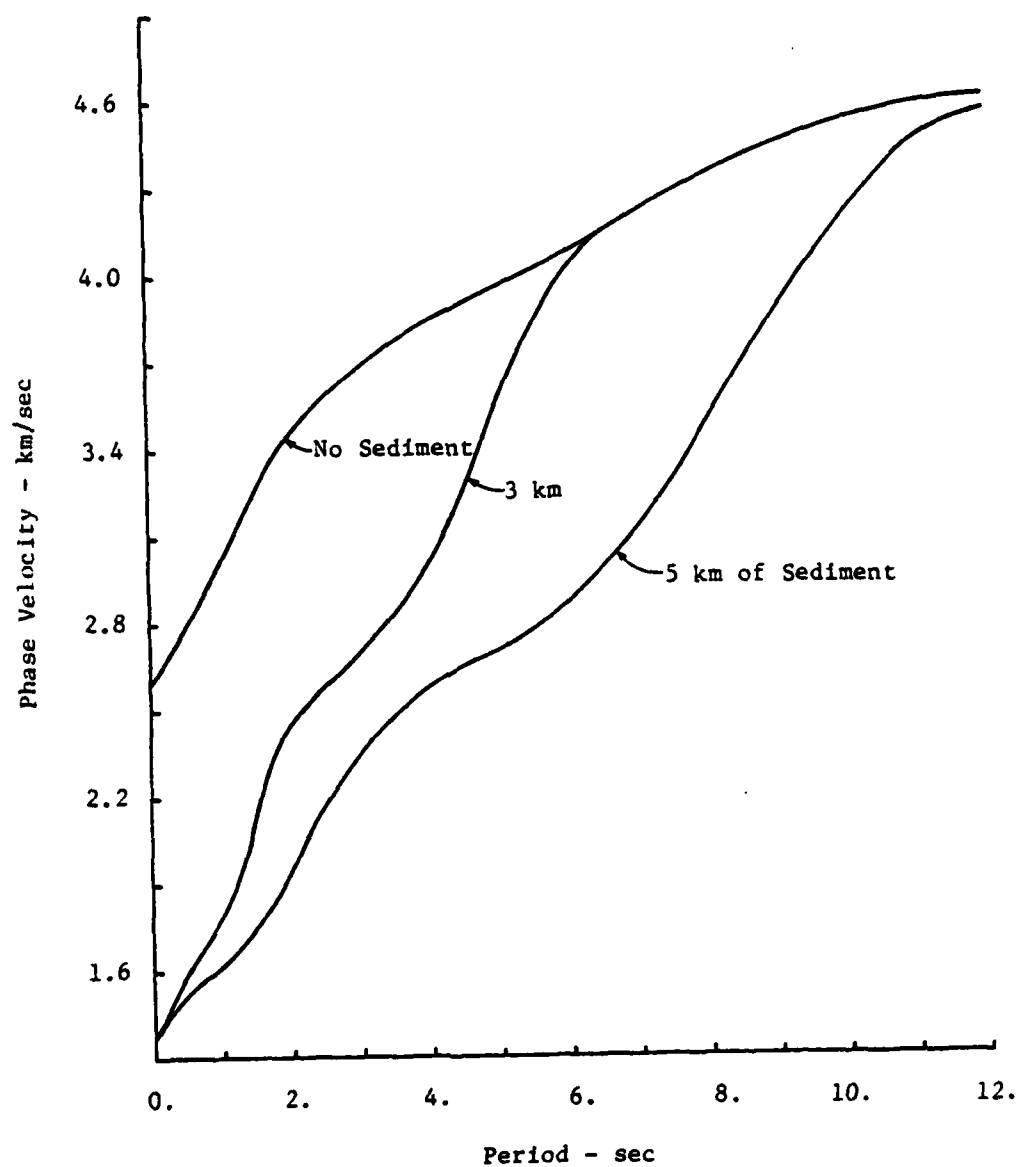


Figure 3-5. Phase velocities for first Rayleigh overtone (second mode) in the Flaming Gorge crust with 0, 3 and 5 km of sediment.

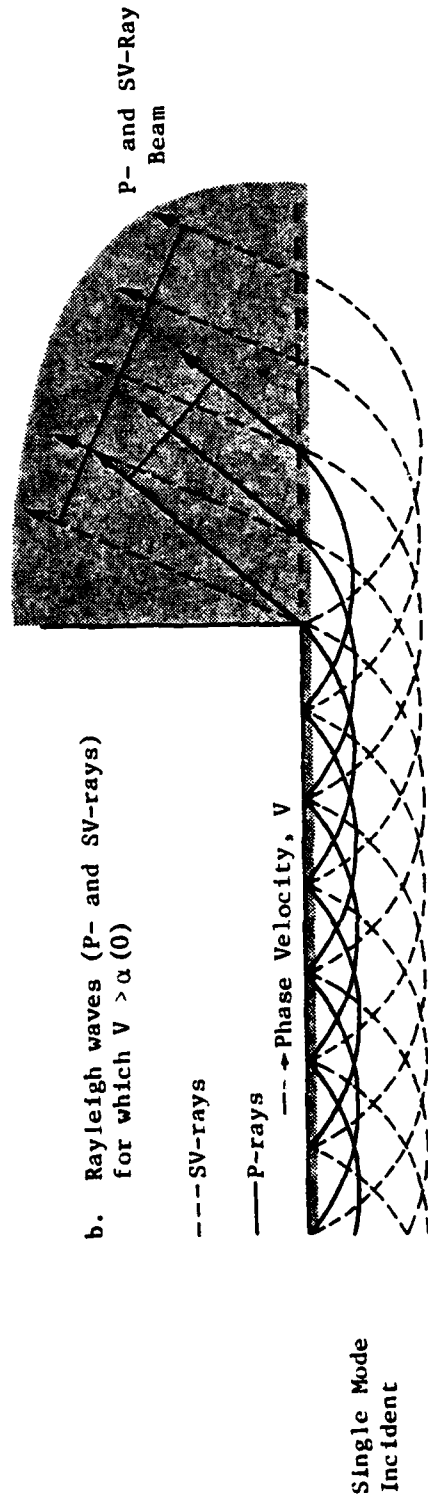
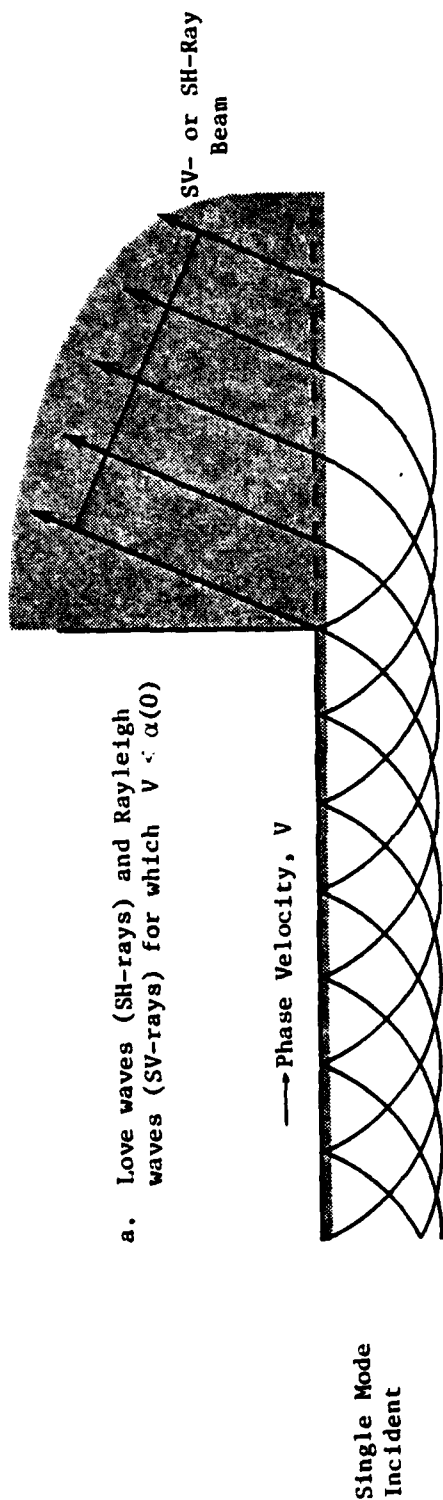


Figure 3-6. Surface wave ray system showing equivalent ray beams in a homogeneous prism joined to the halfspace.

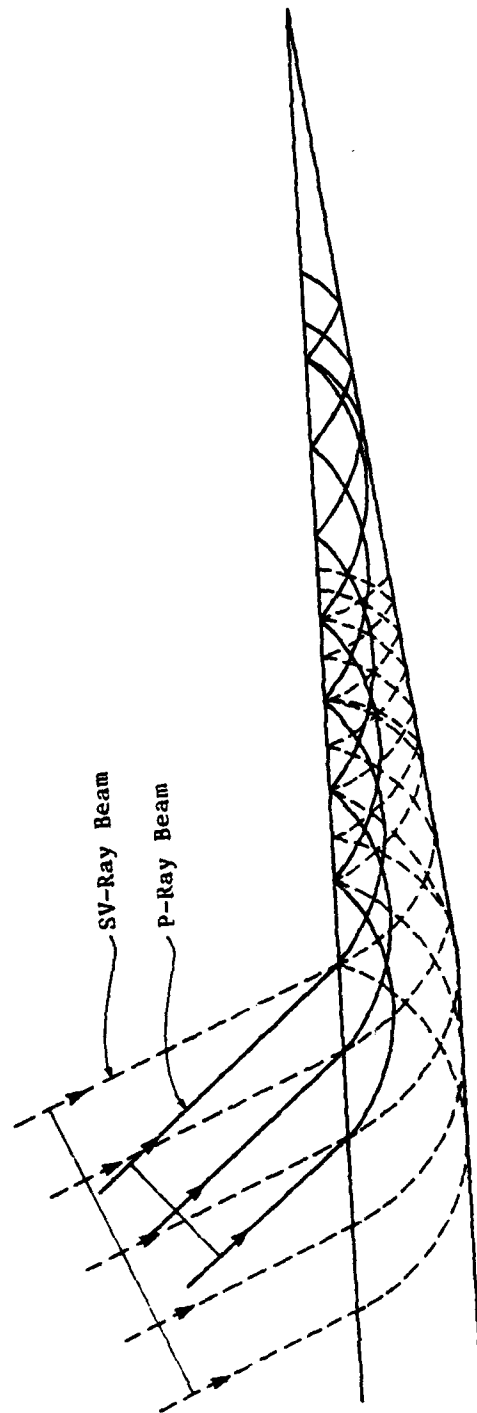


Figure 3-7. The equivalent surface wave beam input and a schematic of ray interaction with a basin flank.

## SECTION 4

### SURFACE WAVES IN SEDIMENTARY PRISMS

In this section we address questions 2 and 3 raised in Section 1.5, as follows:

- How does the non-uniform travel path between Pocatello Valley and the Denver Basin affect short period surface waves reaching Wing V?
- How does surface wave energy leak out of basins and where does it go?

The sedimentary layer along the travel path may be idealized as a sequence of sedimentary prisms (dipping layers over a half space). Here we analyze the basic geologic units or prototype waveguides as illustrated in Fig. 4-1. A further idealization is that the velocity in the sedimentary prisms is constant and that it overlies a homogeneous halfspace representing a granite basement rock.

Although we have emphasized Rayleigh waves in previous sections, here we concentrate on the Love wave case. This is because both types must eventually be considered and the Love wave case is simpler and embodies most of the ideas which will eventually be required to treat the Rayleigh wave case. This section presents the theory of ray tracing in a prism and the results of Love wave propagation through prototype models of sections of the travel path. These include a range of sediment thicknesses and updip and downdip angles. The two sediment thicknesses considered, 5 km and 2 km, correspond to the western and eastern flanks of the Rocky Mountains, respectively. The interface updips and downdips of 3°, 5° and 10° are observed along the travel path.

We find that updips tend to promote energy leakage into the underlying halfspace while downdips tend to trap energy. We are able to trace the leaked energy into the crust and to determine where it re-emerges at the surface. This information is relevant to the hypothesis that the patterns of seismic

alarms at Wing V are due to leaked surface wave energy which is refracted under the Rocky Mountains. It is also relevant to the general problem of reflection and refraction of surface wave energy at basin edges. These results help to screen candidate sites for facilities which may be sensitive to periods of ground shaking that are conditioned by geology peculiar to basin edges.

#### 4.1 Two-Point Ray Tracing in Sedimentary Prisms

With the surface wave decomposed into rays, the problem of calculating response in a dipping region of the waveguide due to first-order rays can be reduced to ray tracing. This also involves phase and amplitude determination, followed by a ray sum at the output point. Ray tracing is simplified considerably by constructing an equivalent model based on the beam inputs described above. The procedure, illustrated in Fig. 4-2 for Love waves into a downdip, is to replace the upstream waveguide (Fig. 4-2a) by the equivalent beam input at the dipping layer junction (Fig. 4-2b). By extending the dipping interface back through the beam, the problem is analogous to a single beam of SH-rays projected into a wedge or prism. A similar picture holds for Love waves into an updip.

In this context, the two-point ray tracing problem in the dipping layer can be stated as: Given a receiver point,  $R$ , in the prism, find the interface entry points of those rays in the equivalent beam which are incident on  $R$ . The advantage of the equivalent model is that the prism is a semi-infinite sector and lacks a characteristic length. The only lengths involved are the beam width and entry point, which are boundary conditions and do not affect the intrinsic geometry. The virtue of this situation is that lacking a length scale the ray system must exhibit self-similarity, simplifying the ray picture considerably. The two-point solution follows by analyzing the rays.



4.1.1 The self-similar system of rays--Given a prism with included angle,  $\gamma$ , suppose that an SH-ray is shot in the downdip direction from a source near the vertex at radius  $r_1$  and takeoff angle,  $\delta_1$ , on the lower face, Fig. 4-3. The system of multiply-reflected rays is immediately drawn on the basis of straight ray paths and Snell's law for internal reflection (reflection angle equal to incidence angle). Reflections occur at  $r_n$  with reflection angle,  $\delta_n$ ,  $n = 2, 3, \dots$  measured from the normal directed into the prism. Because the geometry lacks a length scale, the ray system must exhibit this symmetry. Dimensionally, no characteristic length requires that the variables and parameters of the ray system reduce to  $r/r_1$ ,  $\theta$ ,  $\delta_1$ , where  $r$  and  $\theta$  are polar coordinates. Consequently, a solution for  $r/r_1$  the ray must take the form

$$r/r_1 = f(\theta; \delta_1, \gamma) ,$$

i.e. homogeneous of degree one. The graphical result is shown in Fig. 4-4 by extending all of the internal rays back towards the vertex, where they are clearly tangent to a single circle centered at the vertex. Radius of the tangent circle,  $r_0$  depends on the source location and takeoff angle as

$$r_0 = r_1 \cos \delta_1 . \quad (4-1)$$

A little geometry shows the extended rays are tangent to the circle at the angles shown, hence

$$r_0 = r_n \cos \delta_n \quad ; \quad n = 1, 2, \dots , \quad (4-2)$$

a very powerful result for the two-point problem. The formula for takeoff angle in (4-2) is found from the geometrical requirement of Snell's law, that incidence angle increases by the prism angle from one reflection to the next, i.e. the recursion  $\delta_{n+1} = \delta_n + \gamma$ , whence

$$\delta_n = \delta_1 + (n-1)\gamma . \quad (4-3)$$

Clearly,  $\delta_n$  must be less than  $\pi/2$ , which places an upper bound on the number of reflections. Solving  $\delta_n < \pi/2$  for  $n$  yields

$$n < 1 + \frac{\pi/2 - \delta_1}{\gamma},$$

from which the upper bound is

$$n \leq N = 1 + \text{INT} \left( \frac{\pi/2 - \delta_1}{\gamma} \right). \quad (4-4)$$

where  $\text{INT}()$  gives the integer part of its argument. The  $N$ th reflection is unique in that the reflected ray never reaches the opposite face, but goes to infinity into the prism interior.

4.1.2 Rays to an interior point--The above relations characterize the semi-infinite ray path from the entry point to reflection points to the point at infinity along the  $N$ th ray. Next, consider the finite ray path from the entry point to some interior point on one of the ray segments illustrated in Fig. 4-5. Assume that the point is on the  $n$ th crossing ray ( $n$  even or odd) at  $R_n$  and  $\theta$ , where the angle is measured from the upper face as shown. In the figure, applying the law of sines to the triangles connecting the vertex  $O$ ,  $r_n$  on a face and  $R_n$  in the interior, radius to the interior point is

$$R_n = r_n \frac{\cos \delta_n}{\cos(\theta_n + \delta_n)}, \quad (4-5)$$

and the distance,  $l_n$  along the ray from the last reflection at  $r_n$  is

$$l_n = r_n \frac{\sin \theta_n}{\cos(\theta_n + \delta_n)} = \frac{\sin \theta_n}{\cos \delta_n} R_n, \quad (4-6)$$

where

$$\theta_n = \begin{cases} \theta & n \text{ even} \\ \gamma - \theta & n \text{ odd} \end{cases}. \quad (4-7)$$

Length of the ray path from the entry point to the reflection at  $r_n$  is

$$L_n = r_n \sin \delta_n - r_1 \sin \delta_1, \quad (4-8)$$

which follows by unfolding the ray outside the prism about each reflecting face. Referring back to Fig. 4-4, these unfolded rays are coincident with the extended ray tangent to the circle. Images of the corresponding reflection points are marked  $\hat{r}_n$  in the figure. Therefore, the total path length from the entry point to a point on the  $n$ th crossing ray at  $R_n, \theta$  is

$$S_n = L_n + \ell_n = r_n \left[ \sin \delta_n + \frac{\sin \theta_n}{\cos(\theta_n + \delta_n)} \right] - r_1 \sin \delta_1, \quad (4-9)$$

where  $r_n, \delta_n$  and  $\theta_n$  are given above. Note that  $r_1 \sin \delta_1$  is just the distance of the entry point to the circle tangency point. This is a convenient point of constant phase for the equivalent beam input described earlier.

**4.1.3 The two-point solution**--The two-point ray tracing problem can now be solved. The solution is illustrated in Fig. 4-6. Assume that the receiver is located at  $R, \theta$  and that, for the time being, single ray sources are distributed over the entire lower face. Referring to the figure, there are exactly  $N$  entry points,  $r_{1n}$  on the lower face which illuminate the receiver. These correspond to the direct ray,  $n = 1$  and all higher multiples,  $n = 2, \dots, N$ , and follow by rewriting (4-5) using (4-2) as

$$\frac{R_n}{r_1} = f(\theta; n) \equiv \frac{\cos \delta_1}{\cos(\theta_n + \delta_n)}. \quad (4-10)$$

Setting  $R_n = R$  and solving for the corresponding  $r_1$  (renamed  $r_{1n}$ ) yields

$$r_{1n} = \frac{R}{f(\theta; n)}; \quad n = 1, 2, \dots, N. \quad (4-11)$$

If the entry point is within the equivalent beam input window, then it

corresponds to a Love ray from the waveguide, but if  $r_{in}$  is outside the window it has no significance, at least in the present context. Therefore, given an input window corresponding to some Love wave, all rays incident on the receiver can be determined from (4-11).

4.1.4 Amplitude and phase at the receiver--Receiver response is the sum of the incident harmonic waves traveling along the rays, each with its own phase and amplitude. Consider  $M$  rays illuminating the receiver, each with amplitude  $A_i$  and phase  $P_i$ , then response is

$$\begin{aligned} v(R, \theta, t) &= \sum_{i=1}^M A_i \sin(\omega t - P_i) \\ &= A \sin(\omega t - P) \end{aligned} \quad (4-12)$$

where  $A$  and  $P$  are the total ray amplitude and phase given by

$$A \equiv \sqrt{\xi_1^2 + \xi_2^2}, \quad P \equiv \tan^{-1} \frac{\xi_2}{\xi_1} \quad (4-13)$$

and

$$\xi_1 \equiv \sum_{i=1}^M A_i \cos P_i, \quad \xi_2 \equiv \sum_{i=1}^M A_i \sin P_i. \quad (4-14)$$

The individual ray amplitudes and phases,  $A_i$  and  $P_i$  are calculated on the basis of total ray length and reflection history. The amplitude changes at each subcritical reflection ( $\delta_1 < \sin^{-1} \beta_1 / \beta_2$ ) so that  $A_i$  is just the product of the entry amplitude,  $A_1^0$ , and all subcritical reflection coefficients,  $R_1^j$ ,  $j = 1, J_1$ , on the interface,

$$A_i = A_1^0 \prod_{j=1}^{J_1} R_1^j. \quad (4-15)$$

The phase on each ray is determined from the ray length and phase changes at supercritical interface reflections,

$$P_1 = P_1^0 + \sum_{k=1}^{K_1} P_1^k + 2\pi \frac{\hat{S}_1}{\lambda} \quad (4-16)$$

where  $P_1^0$  is the phase at the entry point,  $P_1^k$ ,  $k=1, \dots, K_1$  are the phase changes at supercritical reflections,  $\hat{S}_1$  is the total ray length to the receiver, and  $\lambda = 2\pi/\beta_1\omega$  is the wavelength in the prism. The  $\hat{S}_1$  are measured from some convenient point of constant phase in the equivalent beam. Reflection coefficients may be found in Aki and Richards [1980], for example.

**4.1.5 Updip versus downdip ray tracing**--Although the preceding geometric ray analysis was done for the downdip case, it is equally valid for updip. This can be seen by continuing the entry angle,  $\delta_1$ , in Fig. 4-3 from positive values (downdip) through zero to negative values (updip). To consider the updip case, it is only necessary to let  $\delta_1$  be negative in the formulas, by analytic continuation. This yields a significantly different ray picture because as the ray shoots updip, from (4-3) its incidence angle increases by the dip angle through negative values at each reflection until it passes through zero. At this point incidence angle is positive and the ray shoots downdip, i.e. the ray has turned. Such a case is drawn in Fig. 4-7.

In application to Love waves, this implies phenomenological differences between updipping and downdipping transitions. Rays into a downdip tend to increase both their incidence angle and spacing between reflection points, Fig. 4-3. In contrast, rays into an updip decrease their incidence angle and reflection spacing up to the turning ray, and increase them thereafter in the downdip direction, Fig. 4-7. As a consequence, Love rays into a downdip remain trapped in the layer by total reflection because the angles become more grazing;

but into an updip the steepening rays will generally reflect partially at the interface as the turning point is approached, thereby leaking much of their energy into the lower halfspace.

In terms of the equivalent beam input, beam segments crossing the layer in a downdip will spread apart while in an updip they will overlap, caused by the respective increase and decrease in reflection spacing on the faces. The spread due to downdip causes shadows to appear, i.e. regions not illuminated by first-order rays from the beam. The beam is trapped and after the Nth reflection goes to infinity into the interior. These effects are shown in Fig. 4-8 for a 7° downdip with five rays across the incident beam, as in Fig. 4-2. In contrast, for updip, constructive interference in the overlapping regions gives rise to amplification, and when the beams reflect partially off the interface they transmit into the halfspace. Ray beams into a 3° updip with  $\beta_2/\beta_1 = 2$  are drawn in Fig. 4-9. All leaked beams are included although only the first few have significant amplitude.

Finally, note that beams can propagate no further into the transition than the turning point of their rightmost ray for updip; while for downdip the beam cannot reach the free surface past the N or N-1 reflection. Phase velocities on the free surface decrease down the transition, approaching  $\beta_1$  for downdip, but increase for updip, becoming high near the turning point.

#### 4.2 Results of Love Wave Propagation in Sedimentary Prisms

Response at a receiver in the prism can now be determined for Love waves incident from the uniform waveguide. First the dispersion relation for a particular model and mode is solved for a discrete set of phase velocity-period (V-T) pairs, which are converted to ray angle-period ( $\theta_L$ -T) pairs. Then from the equivalent ray beam input (Fig. 4-2), response to first-order rays is found for each  $\theta_L$ -T pair using the recursions and sums derived above for two-point ray tracing in the prism.

Two Love wave models will be investigated representing sedimentary waveguides 2 km and 5 km thick on the eastern and western flanks of the Rocky Mountains, respectively. Approximate attenuation is included to indicate the effect of material damping on response. Three modes will be examined for each model. The transitions include updipping and downdipping layers at 3°, 5° and 10°. Response in the transition is evaluated at an array of discrete points, either over the free surface,  $X$  or through the depth,  $Z$ . For each Love wave mode in a model, displacement amplitude will be calculated both as a function of Love wave period and distance or depth. Results are presented in the form of three-dimensional surface plots typically involving  $10^4$  discrete amplitudes per plot (100 receivers x 100 periods) to achieve adequate resolution.

4.2.1 Ideal free surface response--A typical example of surface response is shown in Fig. 4-10 for the 2 km waveguide into 5° updipping and downdipping transitions. Amplitude is a function of Love wave period and distance from the end of the uniform waveguide into the transition, and is normalized by amplitude in the waveguide. In addition to the response surface, peak amplitude over the transition as a function of period is plotted in the vertical amplitude-period plane. The plots graphically illustrate the fundamental difference between updip and downdip propagation in a transition. Namely, updip is characterized by patterns of amplification and downdip by patterns of deamplification. The explanation follows from the geometric comparison of updip and downdip in Sec. 4.1.5.

Consider updip response for a particular period in Fig. 4-10. Moving along the transition, near the origin, response is identical to that in the waveguide until the point of first beam overlap is reached, where the amplitude doubles. Past the overlap the amplitude is unity until the next sequence of beam overlaps amplifies it by constructive interference. Continuing past the point of maximum

amplification, the amplitude decreases roughly stepwise and then very quickly to zero as the beam is turned in the downdip direction. Interface reflections near the turning point are partial, transmitting most of the incident energy into the halfspace. Consequently, backscattered rays have negligible amplitude and effect.

For downdip response, again consider a particular period. Near the origin, response is identical to that in the waveguide up to the first shadow where the amplitude drops to zero. This is followed by a zone of unit response, shadow, etc. These alternations are caused by gaps between the ray beam on the free surface as it reverberates in the downdip direction.

The patterns of abrupt variation in amplitude for both updip and downdip are caused by either a change in the number of rays (beams) incident on the receiver point; or a change in one or more interface reflections on a ray, from partial to total or vice versa. In both dip cases, the sequence of jumps is seen to smoothly migrate down the transition as the period decreases due to the corresponding increase in Love ray angle.

To track the amplitude discontinuities in the  $X$ - $T$  plane, it is convenient to examine the downdip case. By simple geometry the first shadow demarcation appears at distance,  $X_1 = h \tan \theta_L(T)$  from the waveguide. Note that this is half the equivalent input beam width. The next demarcation can likewise be found at  $X_2 = h \tan (\theta_L(T) + 2\gamma)$ , etc. As  $\theta_L$  becomes larger (grazing rays) for shorter periods,  $X_1$  and  $X_2$  increase quickly as the argument of the tan function approaches  $\pi/2$ . This explains the smooth sweep in Fig. 4-10 nearly paralleling the  $T$  axis for longer periods and then paralleling the  $X$  axis for shorter periods.

4.2.2 A comparison of response for both models--Plots of surface response over both sedimentary models are shown in Figs. 1-8a,b for four cases of updip



and downdip. In most part they exhibit the same behavior as described above for Fig. 4-10. The resemblance arises from the essential similarity of the fundamental mode dispersion curves. Peak updip amplifications are comparable for the two models because of similar impedance contrasts between halfspace and layer measured by their ratio,  $\rho_2\beta_2/\rho_1\beta_1 = 1.88$  and  $2.2$  for the 5 km and 2 km layers. There is virtually no backscattering of energy from the updips because of these low impedance contrasts. However, greater contrasts will produce significant reflections back into the waveguide. Comparing the  $3^\circ$ ,  $5^\circ$  and  $10^\circ$  cases shows that the discontinuous surface response becomes sparser as dip angle increases, as well as decreasing peak amplitudes. The reason is fewer beam reverberations at the greater dip angles.

4.2.3 Higher modes and response through depth--The fundamental mode and its first two overtones were calculated for both models. Their features are illustrated in Fig. 4-11 for the 5 km layer with  $5^\circ$  updip and downdip. The fundamental mode exists over all periods while the overtones exhibit cutoffs which are evident in the picture. Correlation of overtone response with that of the fundamental can be made using the dispersion curves. These show that shape of the response surface is a function principally of the Love wave ray angle (i.e. phase velocity). In fact, a stretching transformation on overtone period, to align the overtone dispersion curves with the fundamental mode curve, provides the mapping between response curves. This is evident in a comparison of mode 2 and mode 3 response, e.g. stretch the T scale to double its present length on the third mode and compare to the second.

Mode shapes for the fundamental and two overtones are shown in Fig. 4-12 for the 5 km layer. These are merely plots of amplitude versus depth and period at the waveguide junction into an arbitrary downdip. They were compared to the analytic expression,  $|\cos\omega q_1 z|$  to verify the analysis. Amplitude at the

interface depth in the figure demonstrates the relative strength of the evanescent wave in the halfspace. Clearly, the evanescent waves are stronger as the interface amplitude increases at the longer periods.

Amplitude versus depth in the transition is plotted in Fig. 4-13 for 2 km, 5° updip and downdip. The corresponding surface response was described in Sec. 4.2.1. Downdip cross sections are at 10 and 20 km from the waveguide, and updip sections are at 5 and 10 km. These plots show that for downdip the reverberating but non-overlapping beam creates a diamond pattern of steps in the Z-T plane. The amplitude is zero in the shadows, .5 where one ray is incident and 1. where two rays intersect. Spacing along the period axis decreases with distance from the waveguide. For updip, the diamond patterns are still evident but amplification due to overlapping complicates the picture. It appears that amplification on the surface implies the same through depth, although the amplitude is not a smooth function of depth as for the incident mode, Fig. 4-12. Higher modes exhibit similar patterns.

4.2.4 Effects of material damping on surface response--The analysis described in Section 4.1 was for waves in ideal, non-dissipative geologic media. In reality such materials exhibit material damping. To indicate what effects this damping might have on transition response, a frequency independent  $Q$  was introduced in the ray analysis by merely attenuating amplitude on the basis of  $2\pi/Q = -2\Delta A/A = -2\delta$ , where  $\Delta A$  is the change in amplitude for one cycle on the ray and  $\delta$  is the logarithmic decrement. This is, of course, a crude approximation but for low damping values it is not unreasonable, see Aki and Richards [1980].

Both models were examined for a number of damping values. The results already shown were for  $Q = 1000$ , essentially undamped. Effects are shown in Fig. 4-14 for the 2 km shale/sandstone waveguide, with  $Q = 1000, 100, 40$ .

Clearly, high frequencies are most highly attenuated but response is still significant at moderate distances (10-20 waveguide depths).

#### 4.3 Extension of Ray Tracing to P-SV-Waves in a Sedimentary Prism

The analysis of Rayleigh (P-SV) waves in a sedimentary prism is based on an extension of the theory presented in Section 4.1. The Rayleigh case involves two wave types, P- and SV-body waves, whereas the Love case involves only SH-waves. This section discusses two aspects of the Rayleigh wave case requiring special attention. First, an algorithm is needed to deal with the large number of internal reflections generated in a sedimentary prism. Second, a method is needed to track the energy which leaks into the underlying halfspace due to subcritical interface reflections; this has practical application to tracking surface wave energy leaked from basin edges.

4.3.1 Binary tree representation of rays--Analysis of the Rayleigh case requires more elaborate bookkeeping because at each reflection both P- and SV-waves are usually generated; in fact, the number of rays multiply exponentially and quickly overwhelm the storage capacity even of large computers. This problem is solved by screening out low amplitude rays.

A general scheme for calculating all P-SV-rays is required. The scheme described here involves recursive application of the canonical solution for ray tracing in a prism. Figure 4-15 illustrates a typical P-SV-ray system in a layer. The system consists of a main trunk (the incident ray) from which a cascade of branches (the reflected rays) are produced. Each branch in turn may be regarded as a trunk. This situation is conveniently represented by a binary tree. The term "binary" refers to the fact that a single incident ray usually produces two rays upon reflection. The binary tree data structure is especially convenient for keeping account of ray data (amplitude, phase) in a

format that makes screening easy and computationally economical. In this case, we screen out rays whose amplitudes are below a threshold value.

To illustrate how the binary ray tree is used to screen rays, Fig. 4-16a depicts a fan of rays emanating from a point on a dipping interface. Some of the rays (positive angle) are in the downdip direction while others (negative angle) are in the updip direction. The binary tree for each ray is computed as follows. All reflection points and reflection coefficients are calculated for the trunk ray. When a branch occurs (e.g. when a P-wave is reflected as S- and P-waves), its amplitude is calculated and compared to the threshold value. If the branch amplitude is significant (i.e. greater than the threshold) the branch data is retained in a memory stack; if the branch amplitude is below the threshold, the branch is pruned and no further calculations using it are made. This sequence is followed down the main trunk until all branches are accumulated or discarded. The first retained branch off the trunk then is treated as if it were a trunk and procedure is repeated. The second and subsequent branches are treated similarly.

A graphical illustration of binary tree data in which P- and S-rays are shot at various updip and downdip angles is given in Figs. 4-17 and 4-18. No pruning is applied to these trees. As defined in Fig. 4-16b, S-rays are drawn to the left and P-rays to the right. P-branches generally undergo more reflections than S-branches. In Fig. 4-17, for example, each reflection is denoted by a unit of vertical growth of the branch. Clearly, branches tend to grow more to the right than to the left. Ray trees for S-rays are shown in Fig. 4-18. In cases of shallow updip, the initial reflections of the S-trunk are so shallow that no P-branches are initially generated. For steeper incidence cases, both P- and S-branches are generated at the first reflection.

4.3.2 Leakage of surface wave energy at basin edges--Subcritical reflections at the interface between the sedimentary prism and underlying bedrock result in leakage of surface wave energy out of the prism. This is illustrated in Fig. 1-9 for Love waves of three different periods propagating into a  $3^\circ$  up-dipping transition. In terms of our equivalent ray beam analysis, the energy is leaked as ray beams at angles depending on the dip angle, impedance contrast and period. This treatment neglects diffraction effects which would cause beam spreading and would modify amplitudes. To include diffraction effects requires numerical analysis, which is the subject of current research.

A similar mechanism occurs in the case of Rayleigh wave overtones propagating into an updip; however, in this case, both P- and SV-beams are leaked. An example for a single ray incident on a  $10^\circ$  updip is shown in Fig. 4-19. The leaked rays are shown in Fig. 4-19a for an incident P-ray at three different angles. Two numbers describe each ray--the upper is the amplitude and the lower is the angle of refraction measured from the vertical. An important finding of the analysis is that ray beams of significant amplitude leave the prism at a variety of angles. As a result, these beams will re-emerge at the surface over a wide range of distances from the prism. This is illustrated in Fig. 4-20 where a fan of rays, each of which may correspond to a beam leaked at an angle between  $34^\circ$  and  $55^\circ$  into the Sinclair, WY crust, re-emerges at widely varying distances from the point of incidence. Rays leaked at angles less than  $34^\circ$  or more than  $55^\circ$  would re-emerge at distances greater than 260 km or less than 10 km, respectively. The leaked rays for an incident SV-ray are shown in Fig. 4-19b, where the findings with respect to the variety of exit angles are similar. Comparing Fig. 4-19a and b shows that, in general, S-rays will propagate further up the transition than P-rays. Further study of this problem, including diffraction effects, is warranted.

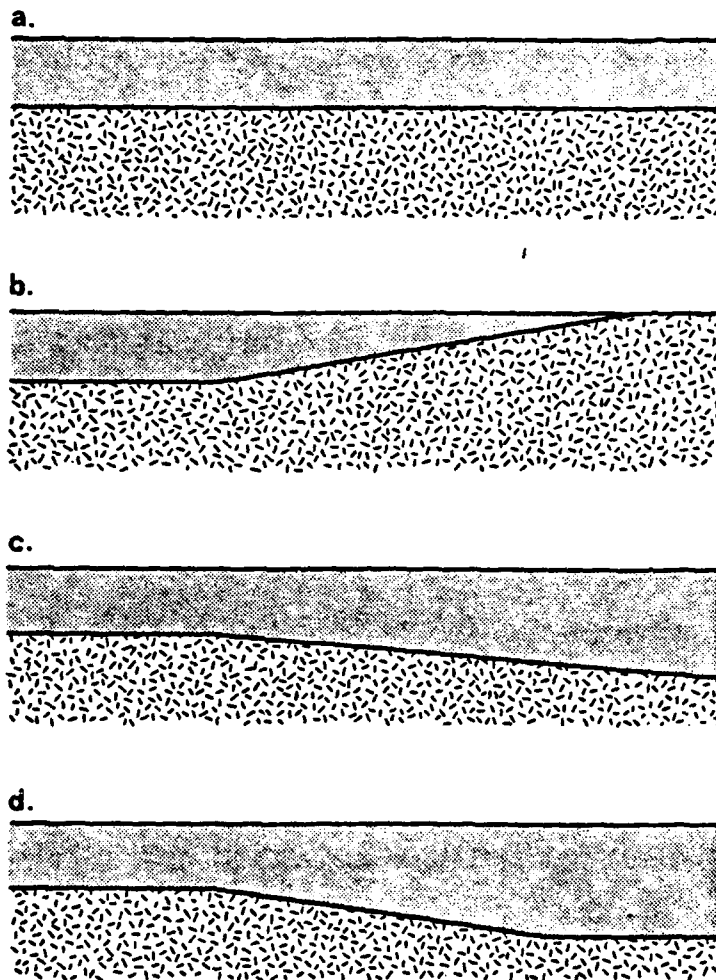


Figure 4-1. Prototype waveguide (a) and waveguide transition (b-d) models.

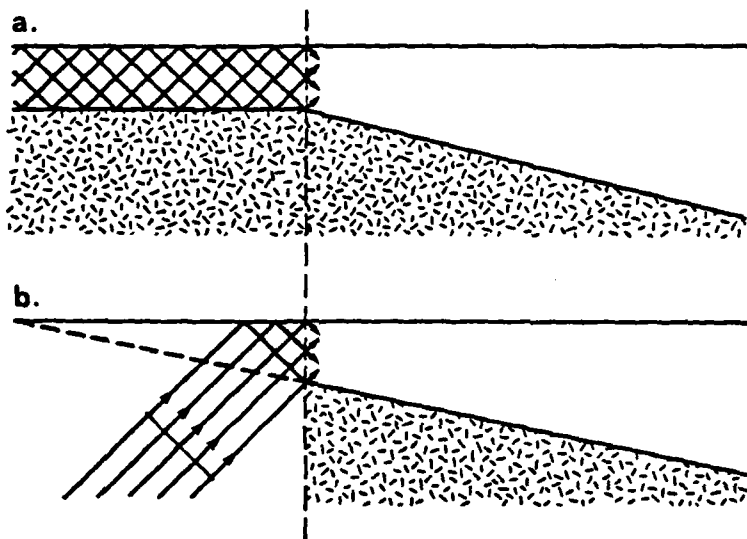


Figure 4-2. The equivalent Love wave transition model based on a ray beam projected into a prism.

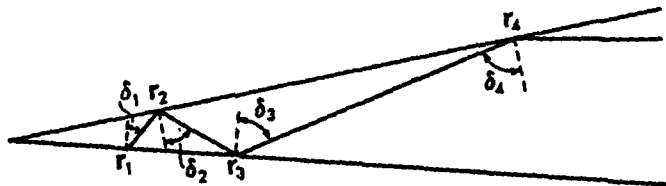


Figure 4-3. The system of multiply-reflected rays in the prism (case of downdip).

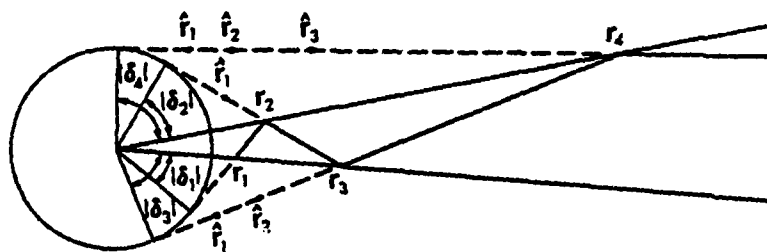


Figure 4-4. The graphical result of self-similarity, all rays tangent to a single circle.



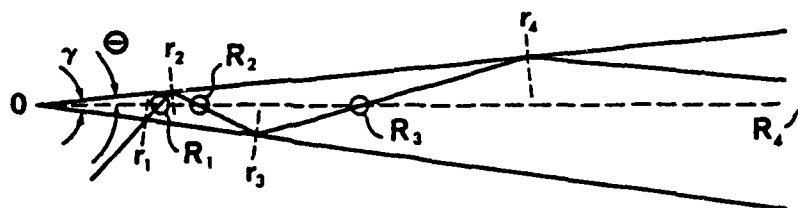


Figure 4-5. The geometry of rays incident on an interior point at  $R_n, \Theta$ .

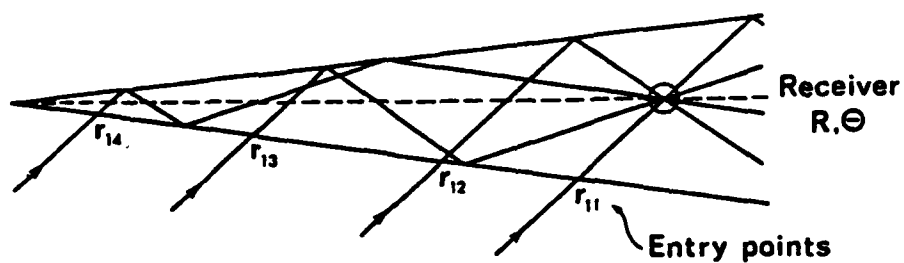


Figure 4-6. The totality of entering rays illuminating the receiver.

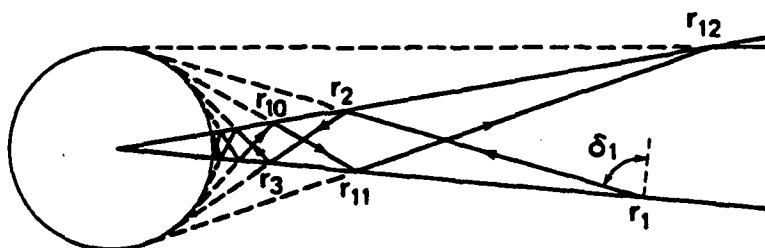
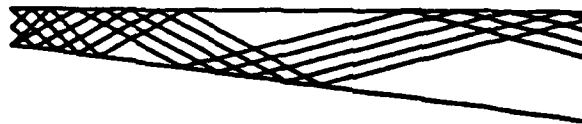


Figure 4-7. The complete ray system for a ray shot in the updip direction.

$\theta_L = 45^\circ$



$\theta_L = 55^\circ$



$\theta_L = 70^\circ$



Figure 4-8. The equivalent Love ray beam in a  $7^\circ$  downdip.

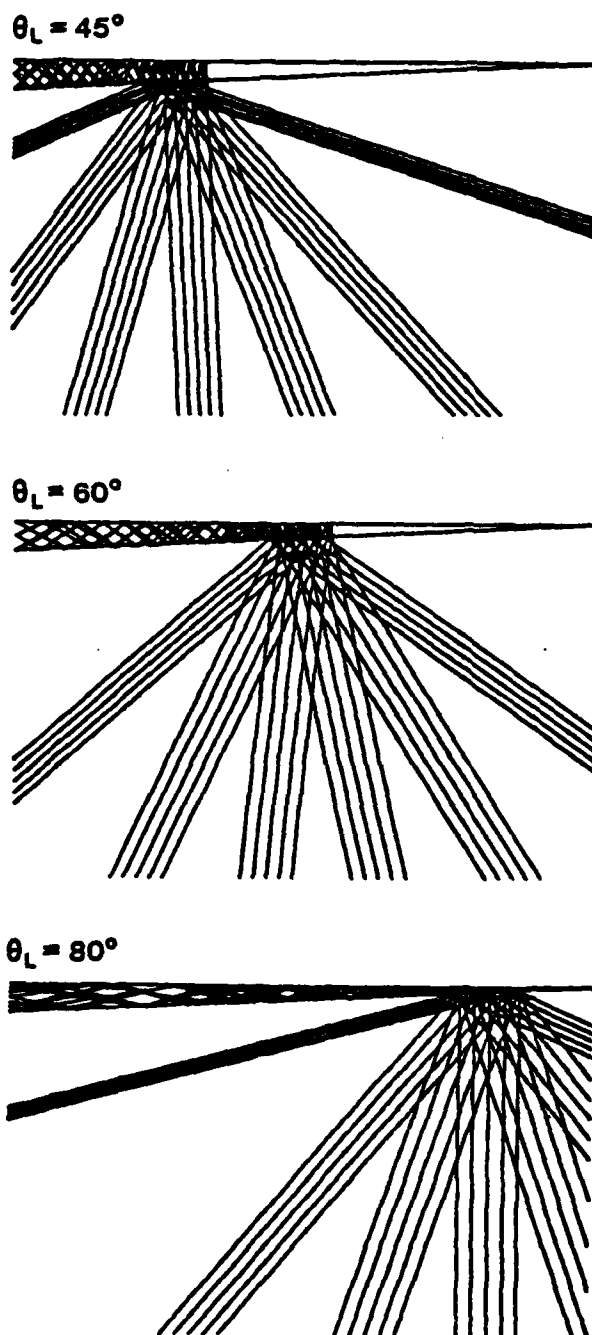


Figure 4-9. The equivalent Love ray beam in a 3° updip showing leaked beams.

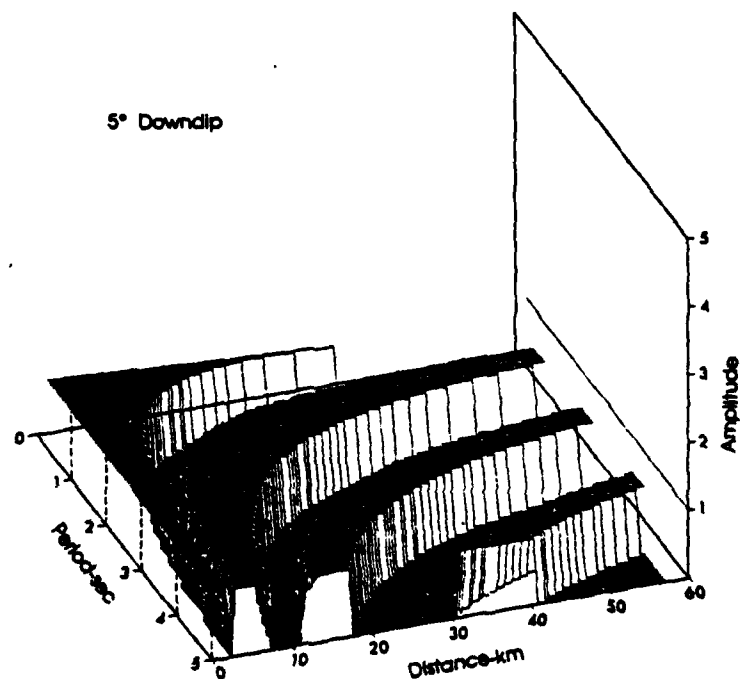
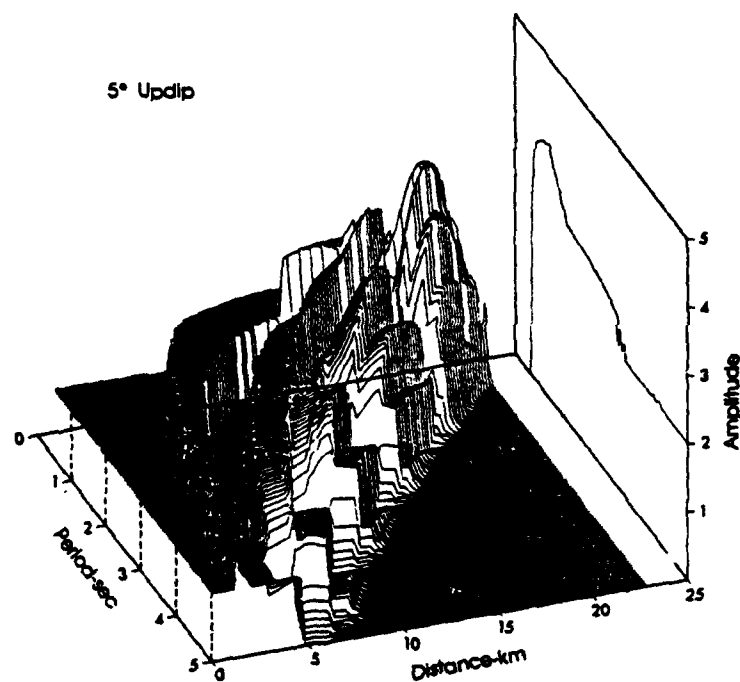


Figure 4-10. An example of the 2 km waveguide fundamental Love mode surface response as a function of wave period and distance over the transition.

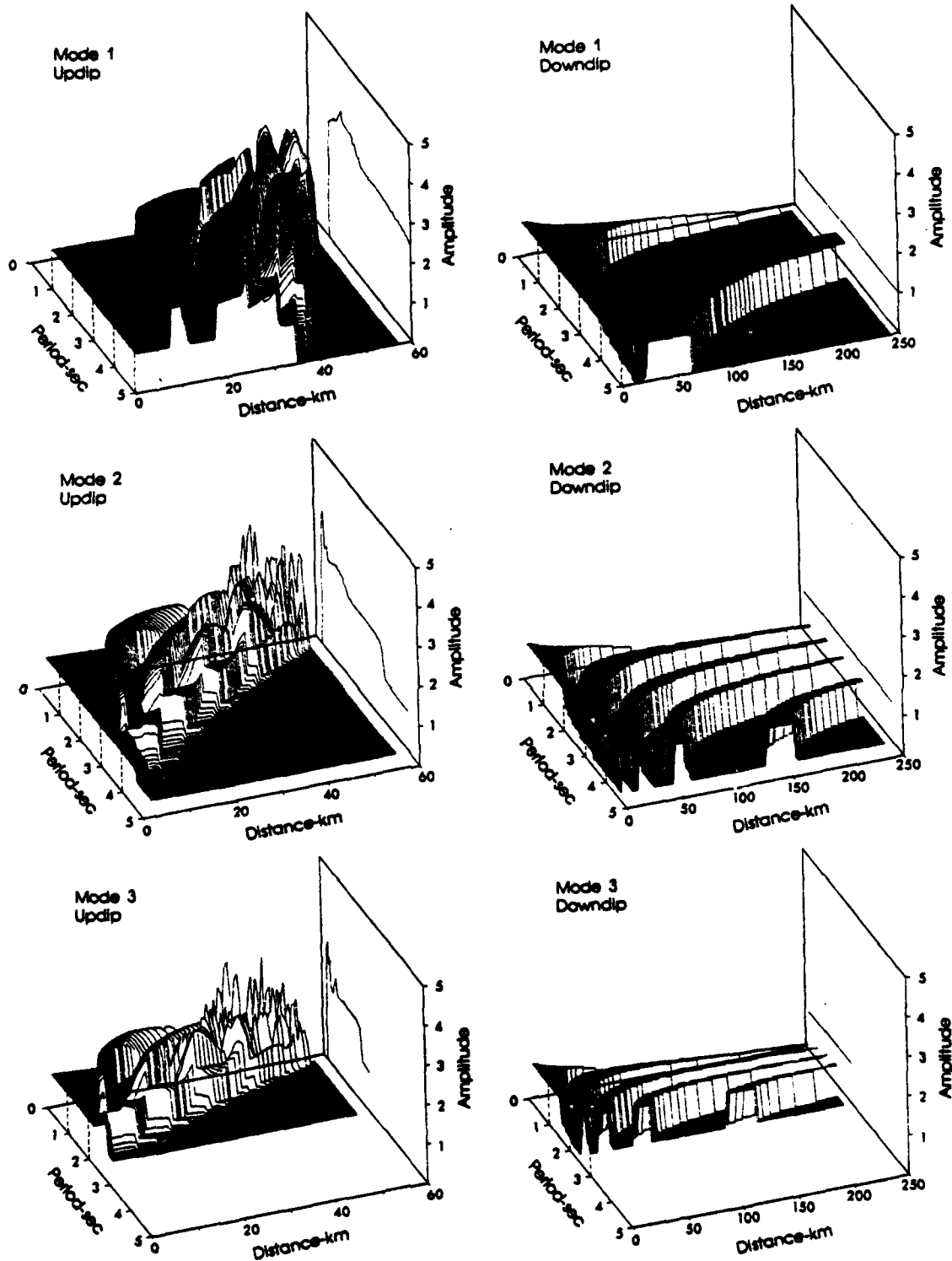


Figure 4-11. 5 km waveguide fundamental and higher mode surface response over 5° updipping and downdipping transitions.

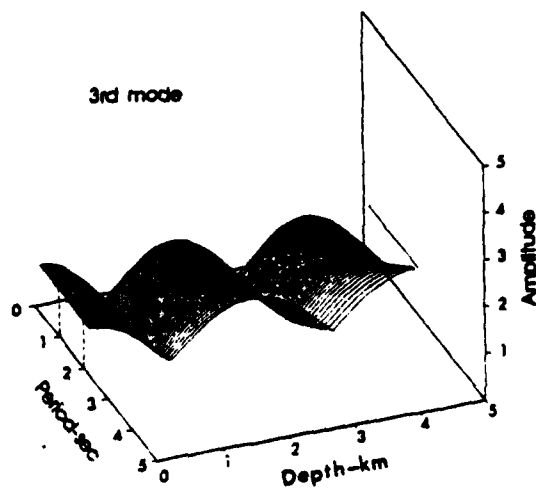
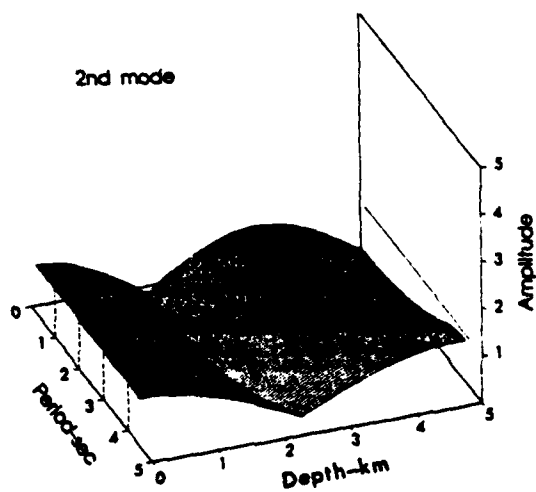
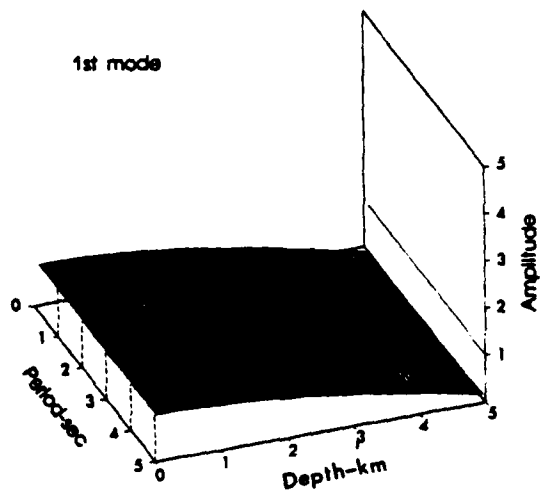


Figure 4-12. 5 km layer mode shapes for the fundamental and first two overtones; given analytically by  $|\cos \omega_1 z|$ .

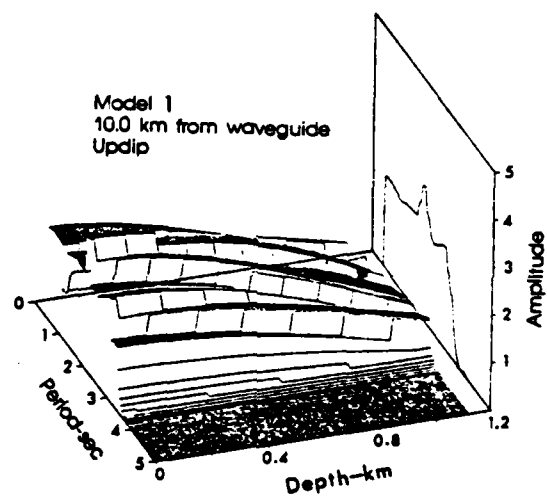
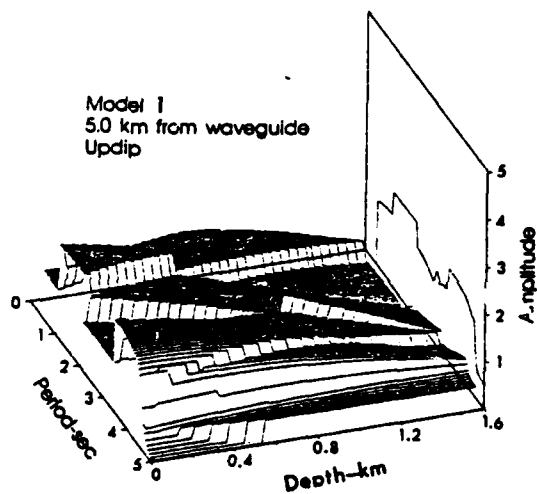
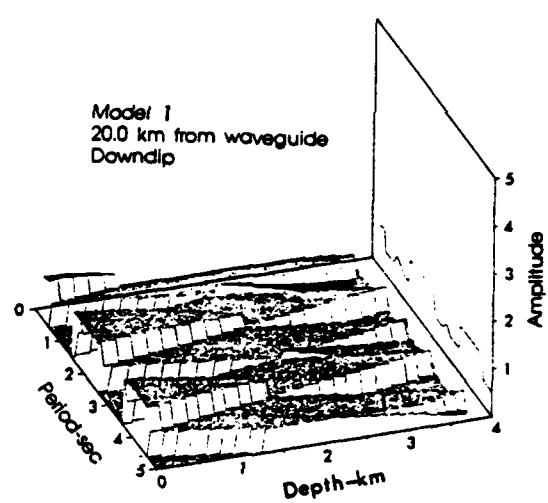
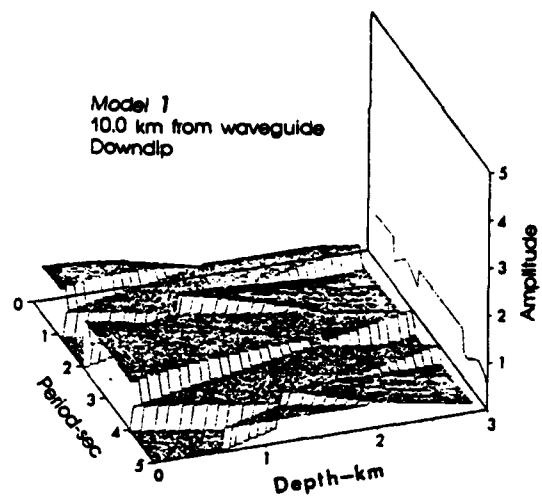


Figure 4-13. Examples of 2 km amplitude through depth in  $5^\circ$  updipping and downdipping transitions (see Fig. 4-10).



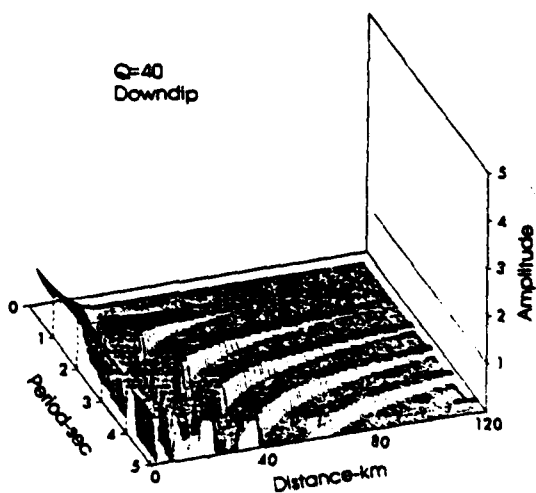
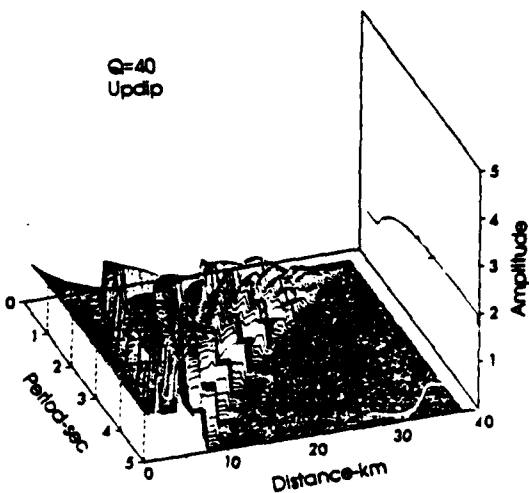
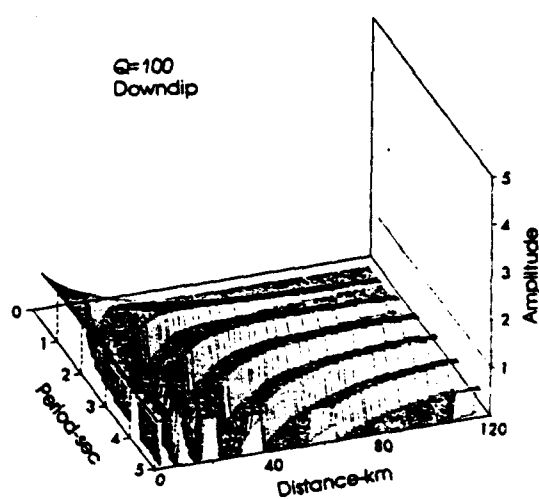
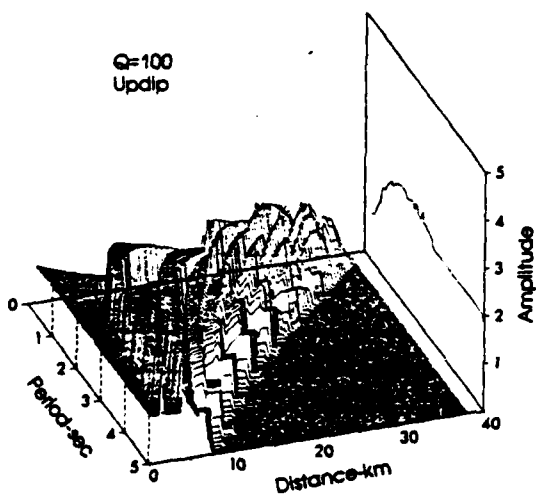
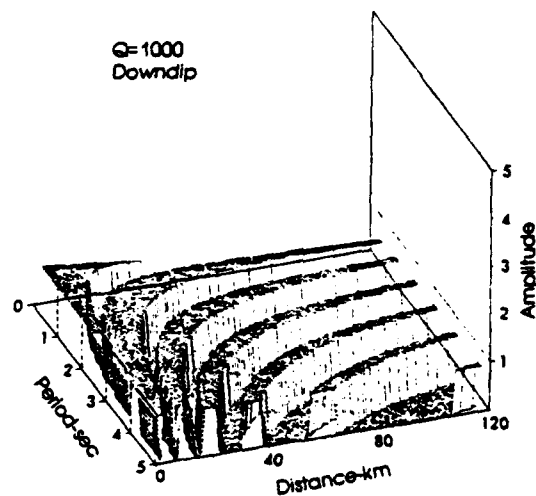
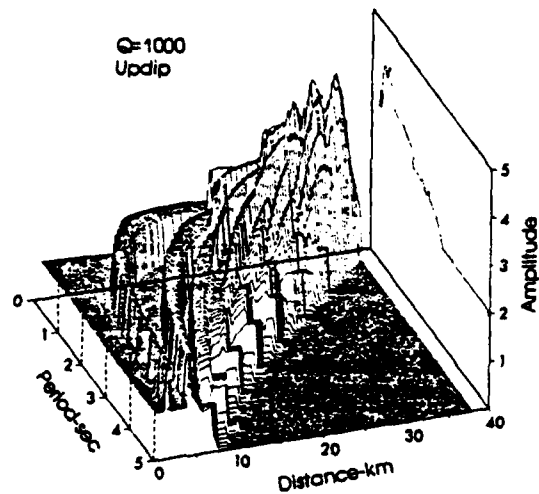


Figure 4-14. Effects of material damping on 2 km, 3° updip and downdip surface response.

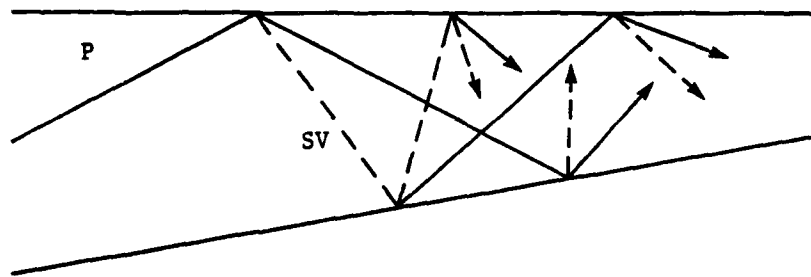


Figure 4-15. A typical P-SV-ray cascade in a layer.

AD-A111 903

WEIDLINGER ASSOCIATES MENLO PARK CA

F/G 8/11

RESEARCH INTO SURFACE WAVE PHENOMENA IN SEDIMENTARY BASINS.(U)

DEC 81 G L WOJCIK, J ISENBERG, F MA F49620-80-C-0009

R-8144

AFOSR-TR-82-0065

NL

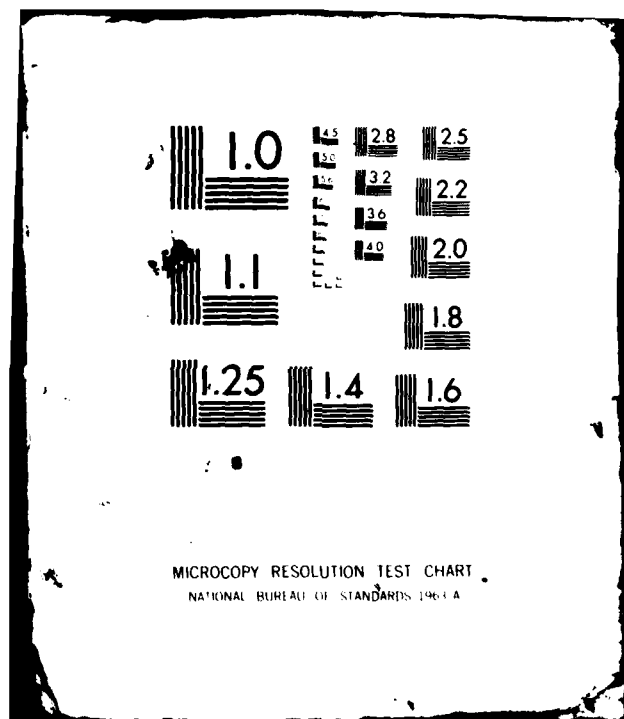
UNCLASSIFIED

2 - 2

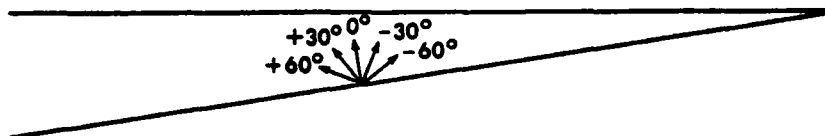
1 - 1



END  
DATE  
FILMED  
4 82  
DTIC



a. A ray fan in the prism



b. The P- and S-ray convention in the binary tree

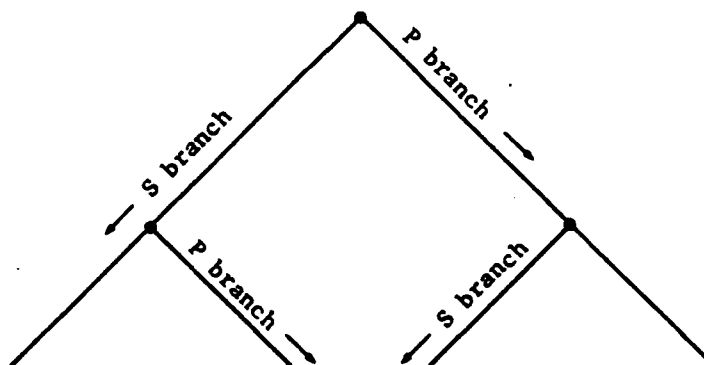


Figure 4-16. The ray fan in a prism, and the convention for drawing the binary tree for each ray of the fan.

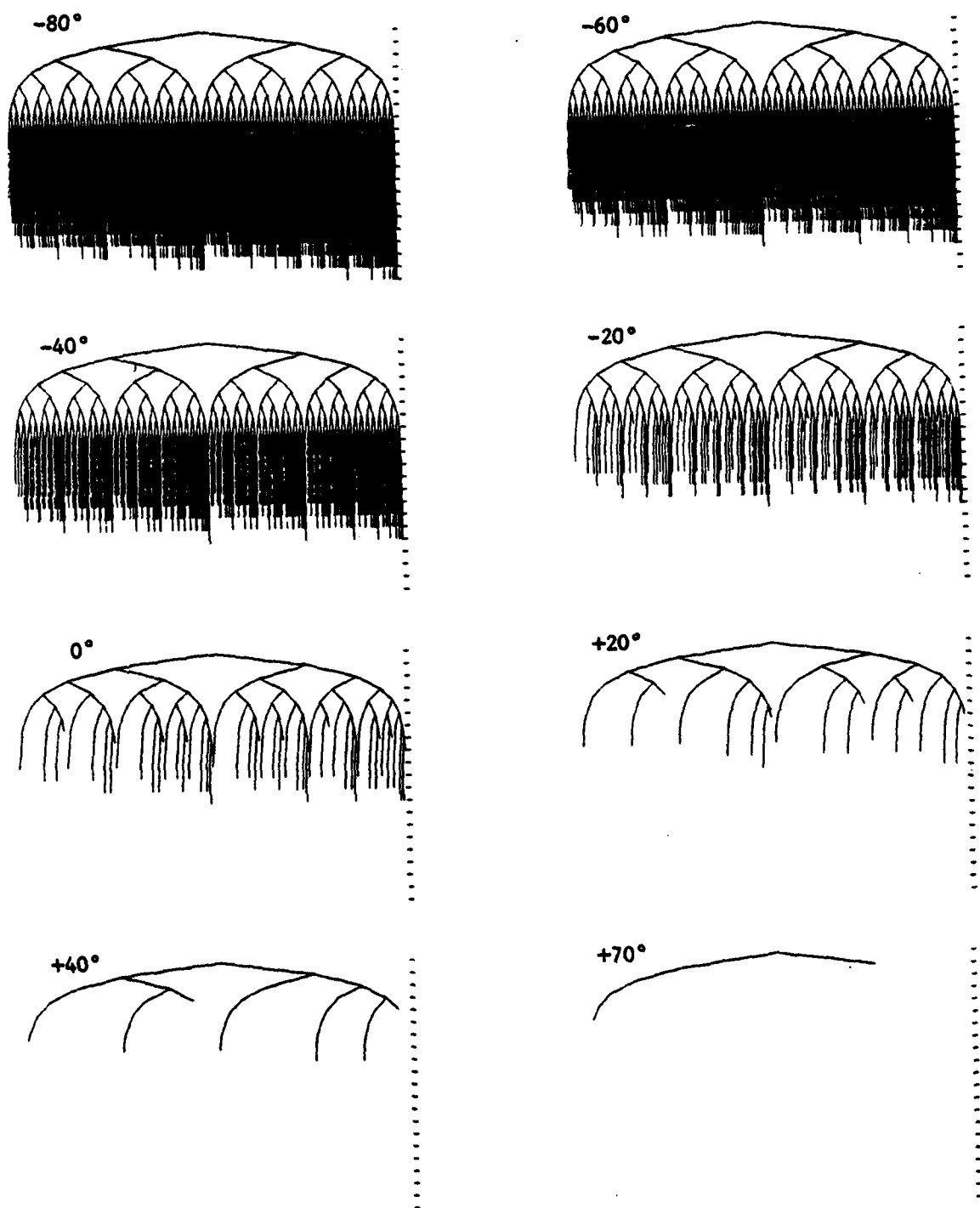


Figure 4-17. P-ray binary trees for the  $10^\circ$  prism in Fig. 4-16a.  
Ratio of P to SV velocity is 1.5 in the prism.

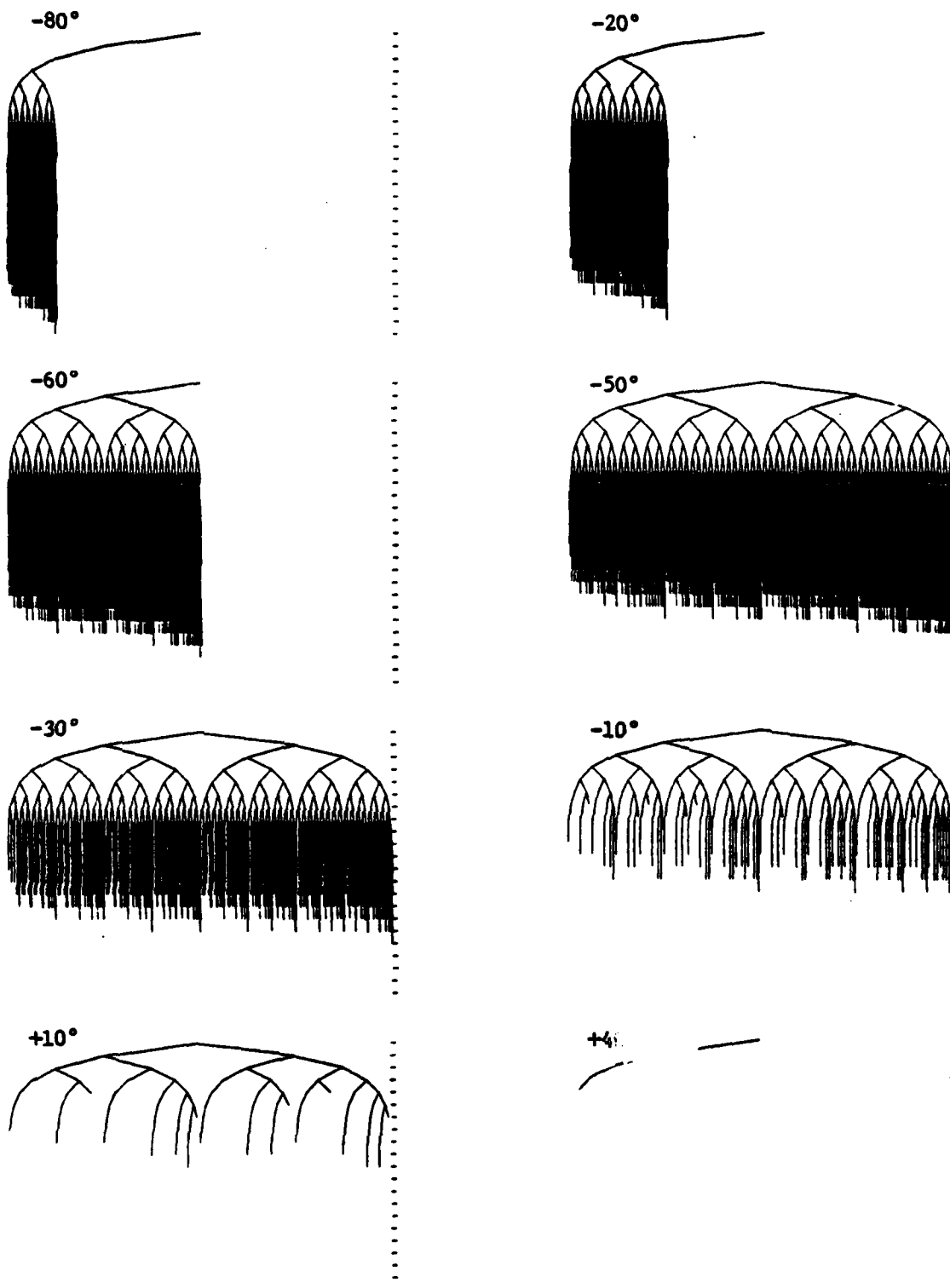


Figure 4-18. S-ray binary trees for the 10° prism.

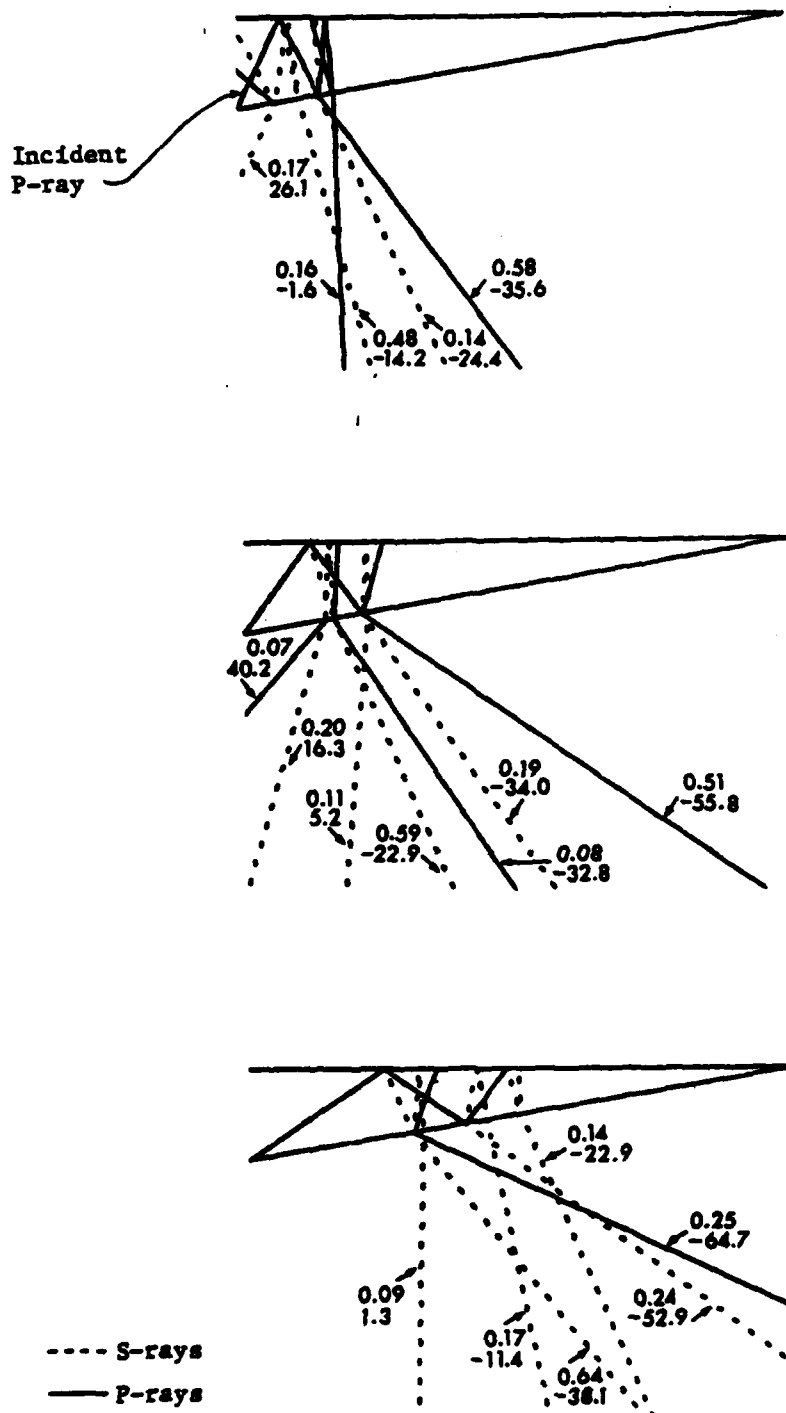


Figure 4-19a. Leaked rays from a  $10^\circ$  prism for an incident P-ray. Upper number is amplitude and lower is angle from vertical in degrees (negative sign for updip). Rays in prism are pruned to an amplitude of 10% of incident ray.



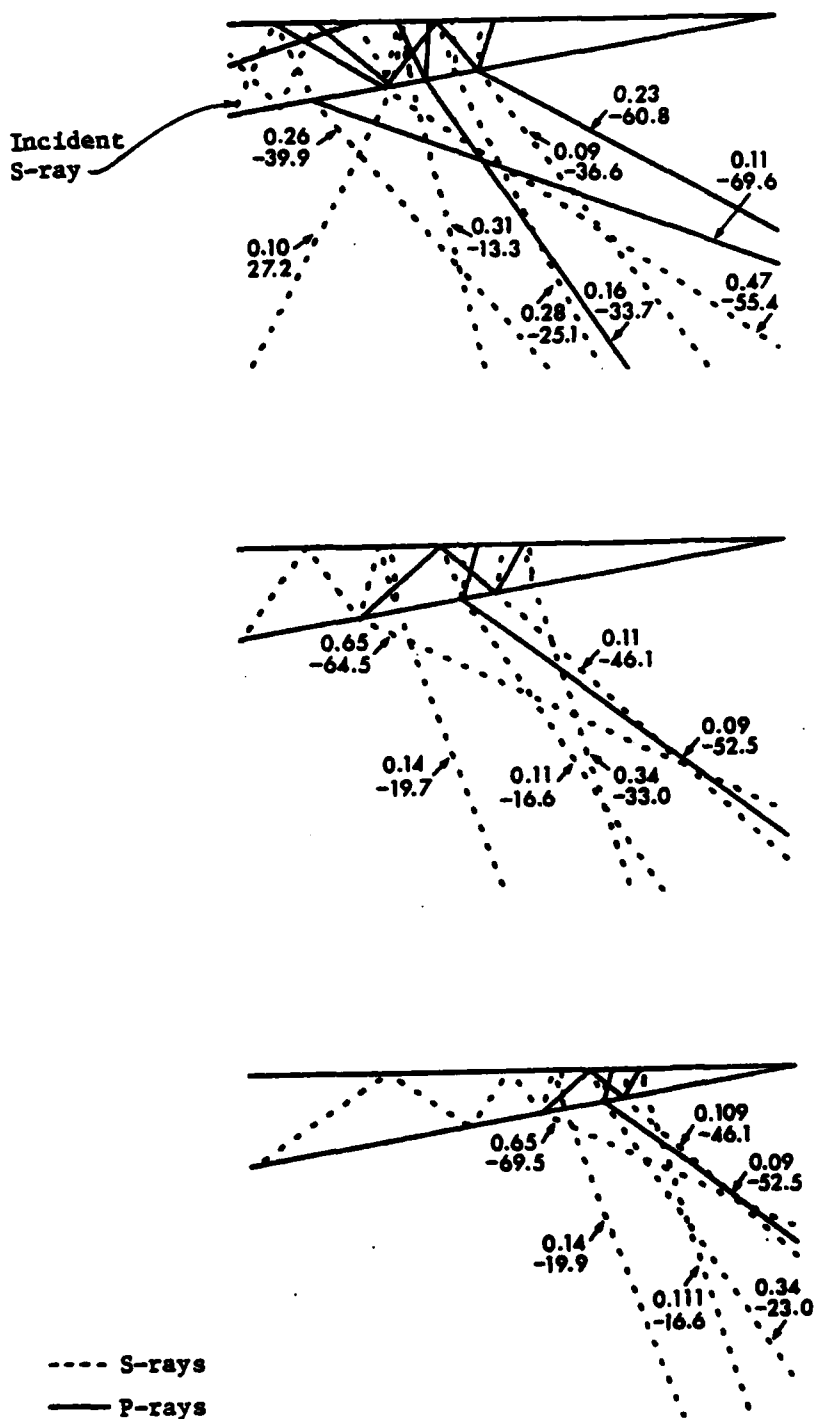


Figure 4-19b. Leaked rays for an incident S-ray.

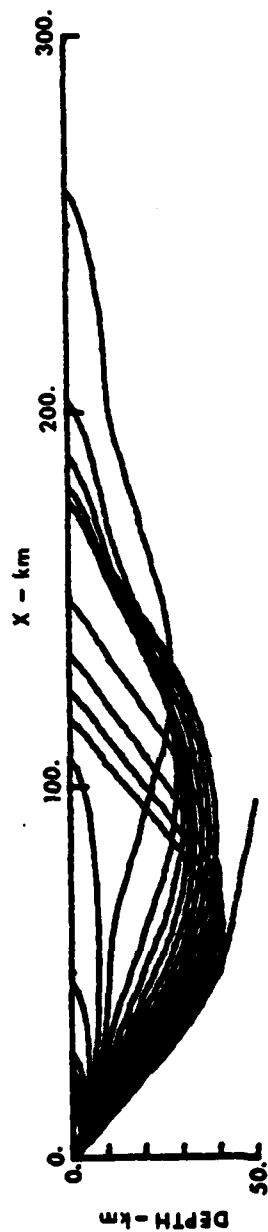


Figure 4-20. A ray fan in the Sinclair crustal model with no sediment. The fan is from  $34^{\circ}$  to  $45^{\circ}$  in increments of  $1^{\circ}$  and illustrates the paths of leaked rays into bedrock.

## SECTION 5

### SUMMARY AND CONCLUSIONS

This section briefly summarizes the work performed under the present contract and presents the main conclusions prompted by three questions stated in Section 1.5. The methods used in this study consider idealization of the geology and a portion of the complete wave field. To consider more complete solutions requires full wave field numerical analysis.

#### 5.1 Summary

This report examines the propagation of surface waves from the Pocatello Valley, Idaho earthquake sequence across Wyoming and the central Rocky Mountains to Wing V. A model of the travel path between Pocatello Valley and Wing V is prepared on the basis of geological reconnaissance including geology and tectonics of the Rocky Mountain region. Cross sections along the travel path show basin sediments overlying basement rock thinning toward the east with interface dips of  $2^{\circ}$ - $10^{\circ}$ . A range of crustal velocity models were found, including Flaming Gorge, Sinclair and Wolcott, and were augmented with data from oil well sonic logs for near-surface sediments. The arrangement of principal uplifts and basins in the region is three-dimensional and cannot be idealized by simple one- or two-dimensional travel path models.

Short- and long-period seismograms recorded at Golden, Colorado during the 1975 Pocatello Valley earthquake were examined to infer bedrock motion near Wing V. The main event was not well recorded but a magnitude 4.7 aftershock provided data on body and fundamental mode Rayleigh wave phases. From the long-period surface wave data, a group velocity dispersion curve and particle motion orbits (ellipticity) were obtained. Theoretical dispersion curves in crustal models along the travel path were compared with the one derived from the Golden

records. The comparison shows that the measured dispersion curve for the range of periods 5-12 sec lies within the bounds obtained theoretically using the various models along the travel path. Favorable agreement between measured and calculated ellipticity of surface displacements for fundamental mode Rayleigh wave was also obtained. This gives us confidence in extrapolating the theoretical model into the period range of 1-5 sec, which is significant for Wing V seismic alarms. In all theoretical cases examined, group velocity minima were found in this shorter period range suggesting that Airy phases capable of producing long duration ringing of the crust may be significant.

There are two classes of surface waves which are incident at Wing V. One is the fundamental Rayleigh or free surface wave consisting of interfering evanescent waves. The other is the channeled surface wave including Rayleigh overtones and Love wave modes, all of which are composed fully or in part of trapped plane waves. This channeled type may be readily analyzed using conventional ray theory in contrast to free surface waves. In preparation for the study of channeled wave interaction with basin and mountain structure, we examine channeled surface waves using seismic ray theory in smooth crustal models. The results show ray path penetration depths and travel times for P-rays. The finding is that the first Rayleigh overtone (second mode) and the first two Love wave modes are propagated near the free surface, hence interact with lateral variations in the sedimentary cover. However, higher modes travel deeper in the crust and interact much less with surface sediments. This ray viewpoint also provides a basis for representing higher mode surface waves by ray beams in the next part of the study.

To examine the behavior of channeled surface waves along the travel path, the gently dipping sedimentary layer on the western flank of the Rockies is idealized as a homogeneous prism and analyzed by a two-point ray tracing

scheme. Input to the prism consists of various Love modes decomposed into SH-ray beams mentioned above and the solution is constructed by tracking all rays incident on an array of receivers at varying distances along the prism. Examples considered are sedimentary prisms of 5 km and 2 km depth at the input point for various updips and downdips; these are inspired by geology on the eastern and western flanks of the Rocky Mountains, respectively. The model was extended to consider the effects of typical damping values for basin sediments. Overall, these results show that little surface wave energy is reflected at the flank but instead is transmitted into the crust at a variety of angles. To include Rayleigh overtones requires ray tracing for both P- and SV-rays which is much more complicated than the SH-wave case considered above. As a step toward accomplishing this, a binary tree representation of P-SV-ray tracing was developed but the complete ray tracing scheme has not yet been implemented. Some examples showing the leakage of P-SV-rays from the prism are analyzed.

## 5.2 Conclusions

Here we describe conclusions reached regarding the three questions raised in Section 1.5. The first question concerns wave types causing seismic alarms at Wing V. For any surface structure subject to seismic ground shaking, three important factors governing response are amplitude, frequency and duration of shaking. Because the Wing V missile suspension system has three lightly damped (less than 1% critical damping) resonances in the period range 1-5 sec, input of long duration ground shaking at appropriate periods will cause seismic alarms even though input amplitudes are low. Thus, the important factors are proper frequency and sufficiently long duration; for example, periods of about 3.5 sec and durations on the order of 2 minutes.

Short period Golden seismograms from the 1975 Pocatello Valley earthquake sequence indicate the  $P$ ,  $P^*$  and  $P_g$  are of too short duration to be the principal cause of alarms. However, later arrivals, including  $S_g$  body waves, and  $L_g$  Love and  $R_g$  Rayleigh surface waves, possess periods and sufficient durations to cause alarms. This is in contrast to the 1979 St. Elias, Alaska earthquake which also caused seismic alarms due to first arriving P-waves with periods on the order of 3 sec, duration on the order of five minutes and peak amplitude near 0.1 mm.

The travel path between Pocatello Valley and the Denver Basin includes 350 km of the Green River Basin with 5-7 km of sedimentary cover (half the travel path). For the period range 1-5 sec, first and second mode Rayleigh waves and first mode Love waves are confined to this sedimentary layer. In contrast, higher mode surface waves propagate much deeper into the crust. Whereas the sedimentary surface waves continually interact with near-surface inhomogeneities, the higher mode crustal surface waves are affected much less because most of their component ray path is at depth. Our ray analysis shows how fundamental mode Love waves and first overtone Rayleigh waves interact with the sedimentary prism on the western flank of the Rocky Mountains. The result of this interaction is leakage of energy in the form of deeper penetrating waves which may or may not re-emerge as body or higher mode surface waves near Wing V. The higher mode crustal surface wave phases which are relatively unaffected by the travel path are steeply incident at Wing V and in terms of their ray components virtually are indistinguishable from body waves except for time of arrival. Therefore, the higher mode crustal phases in the vicinity of Wing V can be viewed as steeply incident body waves which, as shown in our previous report, Wojcik et al. [1980], are responsible for anomalous patterns of seismic alarms due to resonance of the underlying sedimentary column.

The second question deals with the response anomalies due to propagation of surface waves through sedimentary prisms. We find response of the type illustrated in Fig. 4-10. These figures show amplifications and distinct cutoff distances for propagation into an updip, and nominal surface wave response interrupted by shadow zones for propagation into a downdip. These zones propagate with an unsteady speed depending on the dispersive character of the incident surface wave; by dispersive character we mean chiefly the rate at which surface wave period changes at the receiver due to dispersion of the source pulse. These results are relevant to siting of facilities at basin edges. Due to the distinct distance cutoff for updip propagation, facilities can be shielded from longer period components of surface waves. Although shorter period components are incident throughout the prism, they tend to be highly damped in sedimentary and basin fills.

The third question is concerned with leakage of surface wave energy. In basins where depth changes are continuous with interface slopes less than  $15^\circ$  or so, we find that propagation over a downdip tends to promote shallowing of the component rays and energy trapping. In contrast, propagation over an updip tends to promote steepening of the rays, some or all of the energy leaked depending on the geometry, period and interface impedance contrast. The leaked energy can be expressed as spreading ray beams projected into the crust, which will re-emerge at some distance depending on the refraction angle and details of the velocity variation and depth. This leaked energy may have the same depth of penetration (ray parameter) as higher mode surface waves which did not interact with the prism and thereby reinforce them; or the energy may re-emerge near the receiver as a spreading beam of body waves. The former interpretation is appropriate to longer distances (multiple skips) between source and receiver; the latter is more appropriate at shorter distances (single skip).

## SECTION 6

### REFERENCES

- Aki, K. and P. G. Richards [1980]. Quantitative Seismology, W. H. Freeman and Co.
- Allmendinger, R. [1980]. Personal communication, Dept. of Geological Sciences, Cornell University.
- Faust, L. Y. [1951]. Seismic Velocity as a Function of Depth and Geologic Time, Geophysics 16, 192-206.
- Gardner, E.H.F., L. W. Gardner and A. R. Gregory [1974]. Formation Velocity and Density—The Diagnostic Basics for Stratigraphic Traps, Geophysics 39, 770-780.
- Glover, D. P. [1980]. Pocatello Valley Seismograms, National Geophysical and Solar-Terrestrial Data Center (D62), Boulder, Colorado.
- Haskell, N. A. [1941]. The Relation Between Depth, Lithology and Seismic Wave Velocity in Tertiary Sandstones and Shales, Geophysics 6, 318-326.
- Herrmann, R. B. [1978]. Computer Programs in Earthquake Seismology, 1,2, NSF Sponsored, Dept. of Earth and Planetary Sciences, Saint Louis University.
- Jackson, W. H., S. W. Stewart and L. C. Pakiser [1963]. Crustal Structure in Eastern Colorado from Seismic Refraction Measurements, J. Geophys. Res. 68, 5767-5776.
- Jeffreys, H. [1924]. The Earth, Ed. 1, Cambridge University Press, New York.
- Julian, B. R. [1970]. Regional Variations in Upper Mantle Structure Beneath North America, Ph.D. Thesis, California Institute of Technology.
- Keller, G. R., R. B. Smith, L. W. Braile, R. Heaney and D. H. Shurbet [1976]. Upper Crustal Structure of the Eastern Basin and Range, Northern Colorado Plateau, and Middle Rocky Mountains from Rayleigh-Wave Dispersion, Bull. Seism. Soc. Am. 66, 869-876.
- Keller, J. B. [1958]. A Geometrical Theory of Diffraction, in Proc. of Symp. in Appl. Math. 8: Calculus of Variations and its Application, edited by L. M. Graves, McGraw-Hill Book Co.
- Keller, J. B. and F. C. Karal [1964]. Geometrical Theory of Elastic Surface-Wave Excitation and Propagation, J. Acoust. Soc. Am. 36, 32-40.
- King, P. B. [1969]. Tectonic Map of North America, U.S. Geological Survey.
- King, P. B. [1977]. The Evolution of North America, Princeton University Press, Princeton, New Jersey.



#### REFERENCES (CONCLUDED)

- Love, A.E.H. [1911]. Some Problems of Geodynamics, 1967 republication, Dover Publications.
- Majors, M. [1980]. Personal communication, Colorado School of Mines, Golden, Colorado.
- Officer, C. B. [1974]. Introduction to Theoretical Geophysics, Springer-Verlag, New York.
- Oliver, J. [1962]. A Summary of Observed Seismic Surface Wave Dispersion, Bull. Seism. Soc. Am. 52, 81-86.
- Press, F. [1966]. Seismic Velocities, Handbook of Physical Constants, Geol. So. Am., Memoir 97.
- Prodehl, C. [1979]. Crustal Structure of the Western United States, Geological Survey Professional Paper 1034.
- Prodehl, C. and L. C. Pakiser [1980]. Crustal Structure of the Southern Rocky Mountains from Seismic Measurements, Bull. Geol. Soc. Am. 91, 147-155.
- Smith, R. B. and M. L. Sbar [1974]. Contemporary Tectonics and Seismicity of the Western United States with Emphasis on the Intermountain Seismic Belt, Bull. Geol. Soc. Am. 85, 1205-1218.
- Smithson, S. B., J. A. Brewer, S. Kaufman, J. E. Oliver and C. A. Hurick [1979]. J. Geophys. Res. 84, 5955-5972.
- Sommerfeld, A. [1964]. Partial Differential Equations in Physics, Academic Press, New York.
- Thompson, G. A. and J. Hill [1981]. Velocity Data from Wyoming Sonic Logs, for COCORP interpretation, Stanford Geophysics Department.
- Tosaya, C. [1981]. Ultrasonic Velocities and Attenuation in Shales: Identification of Shale Lithologies and Delineation of Abnormal Pore Pressures, Stanford Rock Physics Project 10, Amos Nur, Principal Investigator, 61-101.
- Wojcik, G. L., J. Isenberg and W. S. Dunbar [1980]. Site Dependent Ground Motions from Distant Earthquakes, Prepared for Air Force Geophysics Laboratory and Air Force Office of Scientific Research by Weidlinger Associates, Menlo Park, CA.

DA  
FILM

4-